Title
Pion Correlations as a Function of Atomic Mass in Heavy-Ion Collisions

Author
Chacon, A.D.

Publication Date
1989-12-04

UC-413
LBL-28149

Lawrence Berkeley Laboratory
UNIVERSITY OF CALIFORNIA

Pion Correlations as a Function of Atomic Mass in Heavy Ion Collisions

A.D. Chacon
(Ph.D. Thesis)

November 1989

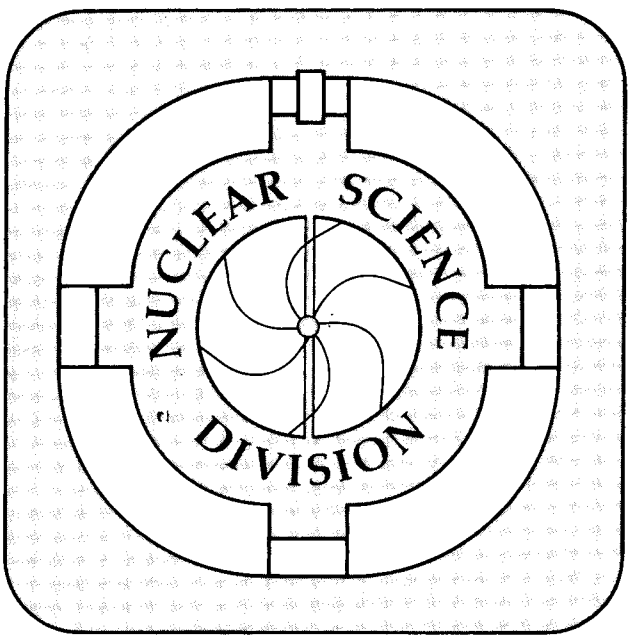

Prepared for the U.S. Department of Energy under Contract Number DE-AC03-76SF00098.

DISCLAIMER

LBL-28149

Pion Correlations as a Function of Atomic Mass in Heavy Ion Collisions

Aaron Dean Chacon
Ph. D. Thesis

Department of Physics
University of California

and

Nuclear Science Division
Lawrence Berkeley Laboratory
1 Cyclotron Road
Berkeley, California 94720

November 26, 1989

This work was supported by the Director, Office of Energy Research, Division of Nuclear Physics of the Office of High Energy and Nuclear Physics of the U.S. Department of Energy under Contracts DE-FG03-87ER40323 and DE-AC03-76SF00098.

Abstract

The method of two pion interferometry was used to obtain source–size and lifetime parameters for the pions produced in heavy ion collisions. The systems used were 1.70 · A GeV ^{56}Fe + Fe, 1.82 · A GeV ^{40}Ar + KCl and 1.54 · A GeV ^{93}Nb + Nb, allowing for a search for dependences on the atomic number. Two acceptances (centered, in the lab., at $\sim 0°$ and 45°) were used for each system, allowing a search for dependences on the viewing angle.

The correlation functions were calculated by comparing the data samples to background (or reference) samples made using the method of event mixing, where pions from different events are combined to produce a data sample in which the Bose–Einstein correlation effect is absent. The effect of the correlation function on the background samples is calculated, and a method for weighting the events to remove the residual correlation effect is presented. The effect of the spectrometer design on the measured correlation functions is discussed, as are methods for correcting for these effects during the data analysis.

The form of the correlation function fit allowed the source to have different radius parameters in the direction perpendicular to the beam and parallel to the beam (although the source was assumed to be cylindrically symmetric about the beam axis). The source parameters show an oblate source (e.g., $R_\perp > R_{||}$) for the lighter systems and an approximately spherical source for the heaviest system. When the two acceptances are compared system by system, $R_\perp$ for the 0° acceptance agrees with $R_\perp$ for the 45° acceptance, whereas $R_{||}$ is smaller in the 45° acceptance than in the 0° acceptance. The dependence on atomic number shows that $R_\perp$ is essentially constant and $R_{||}$ shows a large dependence on atomic number. Fits where $R_\perp$ was forced to equal $R_{||}$ were made for all systems in the 45° acceptance and the Ar + KCl data are compared to earlier measurements made on the same system with a similar acceptance. Cuts imposed on the pions' momenta show no evidence for source size dependence on pion momentum.

Contents

1 Introduction 1

1.1 Organization 2

1.2 Notation 4

2 Historical Review 5

2.1 Photon–Photon Correlations 5

2.2 Particle–Particle Correlations 6

2.3 Particle Correlations in Nuclear Collisions 8

3 Motivation and Theory 11

3.1 Motivation 11

3.2 Derivation of Bose–Einstein Correlations 12

3.3 Correlation Function Used in the Fit 14

3.4 Experimental Correlation Function 16

3.5 Coherence and the λ Parameter 17

4 Apparatus 20

4.1 The Bevalac Accelerator 20

4.2 The Janus Spectrometer 20

4.3 Fast Electronics and Computer Readout 28

5 Track finding and Particle Identification 32

5.1 Outline of the Problem 32

5.2 Hit Finding 33

5.3 Effective Edge Track Finding 38

5.4 Two Track Efficiency 48
5.5 Particle Identification 49
5.6 Momentum and Other Track Parameter Fitting 50

6 Background Generation and Function fitting **53**
6.1 Background Event Generation 53
6.2 Derivation of Event Mixing 54
6.3 Residual Correlations 59
6.4 Iteration Scheme for the Event Weights 60
6.5 Momentum Difference (**Q**) Histograms 64
6.6 Background Fluctuations 65
6.7 Other Corrections 66
6.8 Fitting the Correlation Function 68
6.9 Summary of the Fitting Procedure 70

7 Results from the Correlation Function Fits **71**
7.1 Presentation of the Data 71
7.2 Fits to Monte Carlo Data 72
7.3 Projections for the Data 80
7.4 Confidence Contours for the Data 87
7.5 Study of the Coulomb Corrections 87
7.6 Systematic Uncertainty 95
7.7 The Parameters 96
7.8 Discussion 102

8 Conclusions and Future Work **107**
8.1 Conclusions 107
8.2 Future Work 113

A The Monte Carlo Program **115**

Bibliography **117**

List of Figures

4.1 The Janus spectrometer in the plan view (1982). 21
4.2 The Janus spectrometer in the plan view (1986). 22
4.3 Contour plot of the acceptance for the Fe setups. 27
4.4 Trigger logic part 1. 29
4.5 Trigger logic part 2. 30
4.6 Slow Logic. 31

5.1 A triangle in a wire chamber. 34
5.2 Three hits in a wire chamber showing possible shared wires. 37
5.3 The Janus magnet with the set up for the Δr calculation. 39
5.4 Δr with two tracks per event. 44
5.5 ΔZ_3 with two tracks per event. 45
5.6 ΔZ_4 with two tracks per event. 46
5.7 Track finding as a function of the hit separation. 47

6.1 Estimated fractional uncertainty in the background. 67

7.1 $\langle C(q_0) \rangle$ for the Monte Carlo data. 74
7.2 $\langle C(q_\perp) \rangle$ for the Monte Carlo data. 75
7.3 $\langle C(q_{||}) \rangle$ for the Monte Carlo data. 76
7.4 The 1σ confidence contour for the Monte Carlo data — $R_{||}$ vs. $R_\perp$ plane. 77
7.5 The 1σ confidence contour for the Monte Carlo data — $R_\perp$ vs. τ plane. . 78
7.6 The 1σ confidence contour for the Monte Carlo data — $R_{||}$ vs. τ plane. . 79
7.7 $\langle C(q_0) \rangle$ for the 0° Nb least cut data. 81
7.8 $\langle C(q_\perp) \rangle$ for the 0° Nb least cut data. 82

7.9 $\langle C(q_{\|})\rangle$ for the 0° Nb least cut data. 83
7.10 $\langle C(q_0)\rangle$ for the 45° Nb uncut data. 84
7.11 $\langle C(q_{\perp})\rangle$ for the 45° Nb uncut data. 85
7.12 $\langle C(q_{\|})\rangle$ for the 45° Nb uncut data. 86
7.13 The 1σ confidence contour for the 0° Nb cut data — $R_{\|}$ vs. $R_{\perp}$ plane. . . 88
7.14 The 1σ confidence contour for the 0° Nb cut data — $R_{\perp}$ vs. τ plane. . . . 89
7.15 The 1σ confidence contour for the 0° Nb cut data — $R_{\|}$ vs. τ plane. . . . 90
7.16 The 1σ confidence contour for the 45° Nb cut data — $R_{\|}$ vs. $R_{\perp}$ plane. . 91
7.17 The 1σ confidence contour for the 45° Nb cut data — $R_{\perp}$ vs. τ plane. . . 92
7.18 The 1σ confidence contour for the 45° Nb cut data — $R_{\|}$ vs. τ plane. . . 93
7.19 The 1σ confidence contour for the 0° Ar least cut data — $R_{\|}$ vs. τ plane. 94
7.20 Parameters as a function of A for the 45° data with $R_{\perp} \equiv R_{\|}$. 97
7.21 Parameters as a function of A for the 45° uncut data. 100
7.22 Parameters as a function of A for the 45° cut data. 101
7.23 Parameters as a function of A for the 0° least cut data. 103
7.24 Parameters as a function of A for the 0° cut data. 104

8.1 Pion source parameters as a function of $A_p^{1/3}$. 108

List of Tables

4.1 Beam parameters for the runs. 20
4.2 Spectrometer parameters for the set-ups used. 23
4.3 Stainless steel target composition. 24
4.4 Spectrometer characteristics for the Fe setups. 26
4.5 Locations of the principle components of the Janus spectrometer as used in 1986. 28

5.1 Effective edge parameters for one Monte Carlo track per event. 43
5.2 Resolution for Monte Carlo simulated events. 51

7.1 Parameters extracted from Monte Carlo simulated events. 73
7.2 Parameters as a function of the corrections applied, for a subset of the 0° Fe data. 95
7.3 Statistical uncertainties followed by estimated systematic uncertainties for the Ar and Fe 0° data sets. 96
7.4 Parameters as a function of the projectile, for the 45° data. 98
7.5 Parameters as a function of the projectile, for the 45° uncut data. 99
7.6 Parameters as a function of the projectile, for the 45° cut data. 99
7.7 Parameters as a function of the projectile, for the 0° least cut data. 102
7.8 Parameters as a function of the projectile, for the 0° cut data. 105

8.1 Pion source parameters for different projectile target combinations. 109
8.2 Comparison between experimental and CASCADE pion source parameters for the 45° data. 110

8.3 Comparison between experimental and CASCADE pion source parameters for the Fe data. 112

Dedicated to the memory of Louise Grace Chacon (née Sevier, 1933–1980),

and

to all the other members of my family — each has helped in his (or her) own way.

Acknowledgments

Because of the large number of people involved, it is difficult to recall all the people who have helped with the experiments which are the main part of this thesis. Of course, all the members of the Crowe/Rasmussen group at LBL have helped at one time or another, and I would like to thank all of the members.

I thank the following people for contributions above and beyond the call of duty:

Bill Zajc for, during the brief period when we were both members of the group, giving me many insights into the nature of problem solving in the real world.

Jim Bistirlich for keeping the wire chambers and their electronics going in spite of the fog blowing into the cave and the electronics shack.

Roy Bossingham for helping to keep the wire chambers going, helping to increase the event read–out speed, and keeping me honest during the analysis.

Joe Love for debugging the MBD–11 program with an oscilloscope, the only time in my life that I have seen software debugged using hardware.

Tom Kozlowski for debugging the MBD–11 code over the telephone.

Ivanna Juričić for relevant conversations on many topics related to the analysis of particle–particle correlations.

Ken Crowe for taking me off the street, allowing me to find my own style of data analysis, and allowing me to learn from my mistakes. Of course, any errors that remain in this thesis are the responsibility of the author.

Finally, I would like to thank the taxpayers of the United States who have chosen, through the Director, Office of Energy Research, Division of Nuclear Physics of the Office of High Energy and Nuclear Physics of the U. S. Department of Energy, under contracts DE–AC03–76F00098 and DE–FG0387ER40323, to finance this work.

Chapter 1

Introduction

This thesis is a measurement of the size of the pion emitting region in a heavy ion collision. The measurement was made using intensity interferometry, which is based on the interference of identical particles due to the Bose–Einstein symmetrization of the wave function. The large data sample sizes in this experiment allowed dropping the assumption that the size of the source measured parallel to the beam is equal to the size of the source measured perpendicular to the beam. The systems used were 1.82 · A GeV ^{40}Ar + KCl, 1.70 · A GeV ^{56}Fe + Fe and 1.54 · A GeV ^{93}Nb + Nb,[1] allowing comparison of the data with existing Ar + KCl data[1], and a search for effects depending on the size of the nuclear system. The identical particles used were negative pions.[2] Two different acceptances were used for each system, centered at 0° (in the laboratory and the nucleus–nucleus center of mass) and at 45° in the laboratory, which is approximately 90° in the center of mass, allowing a search for effects depending on the viewing angle. The data samples for Fe + Fe, Nb + Nb (for both acceptances) and for the 0° Ar + Ar, allowed cuts to be made as a function of pion momentum, allowing a search for effects depending on pion momentum. Equal mass target and projectile were used for all systems so that the rest frame of the pion source is the same as the nucleus–nucleus center of mass.

The high statistics available for this experiment made necessary a careful analysis of the spectrometer's effect on the measured correlation function, and a description of the

[1] The notation "1.54 · A GeV" is used to denote "1.54 GeV per nucleon", the total energy of the nucleus is then 1.54 × A in units of GeV, where A is the atomic number.

[2] Although pions were used, any identical bosons could be used. An analogous effect exists for Fermi-Dirac particles.

hardware and software is given, along with the methods used to correct for the effect during the data analysis. For the same reason, a detailed analysis is made of the method used to generate the background, or reference sample and an existing method was modified to give higher accuracy.

Included here is a discussion of the terminology of two pion correlations as used in relativistic heavy ion physics. The word "background" is usually understood to mean everything but the signal desired. In high energy physics this would mean everything but the pions, since particle identification is a concern. In this experiment, the particle identification is much easier because pions are the only negative particles that are abundantly produced in a nuclear collision at this energy, and it is common to assume that anything that is negatively charged is a negative pion. For positive particles, the only contaminants that are likely are protons and, for the energy ranges of interest and the flight path of this spectrometer, it is possible to distinguish between the pions and protons on the basis of time of flight. Therefore, the "background" sample has come to mean the data sample with only the effect that we are trying to measure (the Bose–Einstein correlations) removed. In high energy physics experiments this sample has been called the "reference sample".

The "real" sample is used here to mean the data sample that includes the Bose–Einstein correlations and other effects. It is the data sample that is measured in the experiment. The correlation function is then the ratio of the "real" sample to the "background" sample, since the real sample includes all effects, and the background sample includes all effects except for the Bose–Einstein correlations.

1.1 Organization

The organization of this thesis is as follows:

Chapter 2 is a review of the experimental and theoretical developments that predate this thesis, both in heavy ion collisions and other collisions.

Chapter 3 is a discussion of the theories of nuclear collisions, explaining the motivations for particle–particle correlation experiments, and a derivation of the Bose–Einstein correlation effect.

Chapter 4 describes the apparatus. The locations of the major components of the

spectrometer are given so that the acceptance can be reproduced in detail.

Chapter 5 describes the track–finding and particle identification algorithms and their effects on the observed correlation function. Also described are a series of cuts made on both the real and the background data so these effects are present in both data samples and hence cancel out when the correlation function is calculated. The chapter concludes by describing how the momenta of the tracks are calculated from the wire chamber data.

Chapter 6 describes how the background is calculated from the real data using the method of event mixing. A detailed calculation is made to show that, even though the Bose–Einstein correlations are removed through event mixing, the observed but discarded pions affect the momentum spectra of the remaining pions (this is known as residual correlation). A method is developed where the events are weighted to approximately remove the residual correlation effect. An iterative procedure is developed where the approximate weights are used to calculate more accurate weights, which can be repeated until the desired accuracy is reached. The chapter concludes with a discussion of the techniques used to fit the correlation function to the data and the methods used to estimate the quality of the fit.

Chapter 7 begins by presenting the results of fits to a Monte Carlo simulation of the experiment. The pion pairs were generated so that their momenta were correlated using the same functional form as was used for the fit correlation function, with source–size parameters typical of those measured in this experiment. The pion paths in the spectrometer were then simulated, which allowed for the simulation of the spectrometer's acceptance, and for using the usual data analysis stream on the simulated pion tracks. Comparison of this simulated data with the measured data allows determination of which features are due to the spectrometer's acceptance (which the Monte Carlo simulates, and hence these features are present in the Monte Carlo fits) and which features are due to novel physics (which the Monte Carlo lacks, and hence the Monte Carlo fits will lack). Typical fits for the data are shown in detail and the parameters are given for all fits, including fits for which $R_\perp = R_{||}$ was forced, which can be compared to earlier results (where this was assumed). The results of the earlier experiments and the results of this experiment are discussed.

Chapter 8 discusses future experimental and theoretical needs.

1.2 Notation

In this thesis the convention has been adopted of using math italic lower case letters (e.g., x) for scalars, math italic lower case letters with arrows (e.g., $\vec{x}$) for three–vectors, and bold face capital letters (e.g., $\mathbf{X}$) for four–vectors. In this convention the notation for the four–vector momentum and location are

$$\mathbf{P} = (\vec{p}, E)$$
$$\mathbf{X} = (\vec{x}, t)$$

There are some important scalars that have been given capital letters to distinguish them from the run–of–the–mill scalars. These scalars include $R_\perp$, $R_{||}$ (which are correlation function parameters), C_2, also denoted C_{ij}, (which is used for the correlation function), A (which is used for normalizations), and N (which is used as the number of events in the experiment).

In this thesis, except for Section 5.3 on effective edge track finding, $\mathbf{Q} = (\vec{q}, q_0)$, will be used for the momentum–energy difference of the two pions in the event. In Section 5.3, q will be used for the particle's charge. The notation Δx, where x is a measured quantity, is used for the uncertainty in x. Throughout this thesis the notation $\perp$ (and $||$) will mean the components of a vector perpendicular (and parallel) to the axis through the collision defined by the beam axis. Note that some authors use the same symbols for other reference axes.

Chapter 2

Historical Review

2.1 Photon–Photon Correlations

The earliest mention of identical particle correlations is that of Hanbury–Brown, Jennison and Das Gupta in 1952[2]. They discuss the results of using intensity interferometry to measure the angular sizes of radio sources. A later paper[3] presents the theoretical motivation behind the first paper, based on electromagnetic theory. The description of the apparatus in the second paper is:

> "Two aerials A and B feed two independent receivers tuned to the same frequency with identical band–pass characteristics. The output of each receiver is rectified in a *square–law* detector and is fed to a low–frequency band–pass filter. The outputs $S_1(t)$, $S_2(t)$ of these filters are combined in a correlator ...[emphasis in the original]"

All of the components necessary for a particle correlation experiment are present — two detectors at different locations counting the number of particles (radio–frequency photons) arriving from an extended source. Here the energy of the photons is fixed; the receiver separation must be varied to find the source size.

Intensity interferometry is based on the comparison of the intensity of the electromagnetic waves, not the interference of the waves, so the same theory can be applied to light to produce an interferometry experiment that does not require that the beams of light be brought together to interfere. This is not too surprising since one can reason that

if intensity interferometry works for radio–frequency photons it should also work for light photons, the only difference being the technical one of particle detection. So Hanbury–Brown and Twiss adapted their theory for light[4] and used the intensity interferometry of light to measure stellar diameters. They also improved their resolution by the ratio of the wavelengths (although they could no longer detect the same stars as before). It is interesting to note that the mirrors used in the detectors did not have to be of good optical quality since one does not have to resolve the star very well in order to be able to count the photons coming from it.

Although Hanbury–Brown and Twiss could have used photons in their reasoning, they instead used the fact that photomultiplier tubes are square–law devices, like their radio detectors were. In 1963, Glauber[5] developed the quantum theory of optical coherence and showed that the Hanbury–Brown—Twiss effect was due to photon–photon correlations in incoherent sources. He also showed that for coherent sources[1] the effect was absent. This was experimentally verified in 1965 by Armstrong and Smith[6], when they demonstrated that for a solid–state laser, driven above the lasing threshold,[2] the Hanbury–Brown—Twiss effect was absent. They also found that for the laser driven below the threshold, where it will behave similarly to ordinary thermal sources, the effect is present. For very low driving currents, the effect begins to disappear, because the probability of two photons being in the system at the same time is small.

2.2 Particle–Particle Correlations

A few years after the first photon–photon correlation experiments, Goldhaber, Goldhaber, Lee and Pais[7] rediscovered intensity interferometry while measuring the opening angles of pions produced in $p\bar{p}$ collisions in a bubble chamber.[3] Their analysis interpreted the probability of emission at varying opening angles as the effect of the Bose–Einstein symmetrization of the pionic wave functions, and the size of the thermal source involved in the pion emission. They calculated the number of pions as a function of the opening angle

[1] Here the definition of coherent is (probability for a photon in state i and a photon in state j)^2 = (probability for a photon in state i) × (probability for a photon in state j). A more general definition and definitions for higher levels of coherence (involving more photons) are given in [5].

[2] The parameter used to control the laser in this experiment was the current through the diode junction.

[3] For more details concerning particle–particle correlations see [8].

for various source sizes to compare to their data; the concept of a correlation function was not in use at that time.

In the 1970's Kopylov and Podgoretskii[9], Shuryak[10] and Cocconi[11] proposed to analyze the data in terms of a correlation function, where the ratio of the number of particles with Bose–Einstein correlations (or Fermi–Dirac anticorrelations) to the number of particles with out such correlations is plotted as a function of the momentum difference of the particles. This started two discussions; the first concerns the proper background (or reference) sample (e.g., the sample without the correlations or anticorrelations), and the second concerns the proper functional form to use for the correlation function that is to be fit to the data. A list of the popular functional forms and conversion factors was given in a recent article[12].

There are several plausible schemes for calculating the background data sample, some of them are:

1. Use the relative momentum spectrum from the unlike–sign particles (this is done mainly for experiments using pions).

2. Use the relative momentum spectrum of two like–sign particles coming from different events.

3. Use the relative momentum spectrum of two unlike–sign pions coming from different events.

4. Use the relative momentum spectrum from theoretical calculations that include all of the collision dynamics except for the Bose–Einstein correlations.

The first method has problems with resonances contributing to the unlike–sign particle spectrum differently than to the like–sign particle spectrum. This method is commonly used in high energy experiments where particles of both charge are detected, the effect of resonances can be cut out, and conservation of energy and momentum is a concern. The second method has problems with momentum and energy conservation violations, and residual correlations[4] appearing in the pseudo–events. This method has been used in heavy ion collisions where the momentum–energy violations generated are small since the

[4] See [1] or Chapter 6, this thesis.

pions carry only a small part of the total momentum and energy of the nuclear collision. The third method combines the first and second methods. The role of resonances will be different in this method than in the first method, a possible advantage. The last method has the difficulty of requiring that almost everything must be known about the collision dynamics before the experiment is done. This was the method used in [7], in a form involving integration over many variables.

Work on $p\bar{p}$ two pion correlations led to additional papers[13, 14] that provided increasingly detailed analysis of the data and uncertainties. These papers serve to point out how difficult it is to generate a good background (or reference) data set. A later paper[15] showed, by Monte Carlo simulations, that one of the methods used to generate the background data sets (that of shuffling the components of the momenta transverse to the beam) can induce correlations in the background data, which will obscure the correlations in the measured data.

The Mark II collaboration[16, 17, 18, 19] has studied Bose–Einstein correlations at SPEAR and PEP finding only small variations in the parameter β, where the functional form for the correlation function was $C_2(Q) = 1 + \alpha e^{-\beta Q^2}$, from 4–7 GeV (SPEAR) to 29 GeV (PEP). In this parameterization, Q in the invariant momentum difference ($Q = \sqrt{\mathbf{Q}\mathbf{Q}}$), β is the size of the correlation and α is the strength of the correlation (analogous to λ in Chapter 3 of this thesis). A recent paper[20] has proposed that because of the correlation between the momentum of the particle and its emission point in this type of collision, the source size as measured will reflect the momentum–position correlation effects and will not show the size of the pion emitting source. However, the apparent source size provides information on particle production in the collision process[20].[5]

2.3 Particle Correlations in Nuclear Collisions

In nuclear collisions, there is a length scale present other than that induced by the position–momentum correlation, that of the nuclear diameter.[6] It is thought that the source size will reflect the motion of the hot nuclear matter formed in the early stages of the collision. It was hoped that the pion source size would reveal what the nuclear matter

[5] For more details concerning high energy interactions see [18].
[6] For more details concerning heavy ion collisions see [21].

density was at "freeze out" — the moment that nucleons were far enough apart and cool enough that the interaction phase of the collision could be considered to be over. Another area of interest was the hoped–for ability to determine if coherent emission of pions was taking place in the collision (pion condensation), producing the pion equivalent of a laser.

A series of experiments was conducted at the streamer chamber at the LBL Bevalac accelerator[22, 23, 24, 25] using 1.8 · A GeV ^{40}Ar + BaI_2, 1.8 · A GeV ^{40}Ar + Pb_3O_4, 1.5 · A GeV ^{40}Ar + KCl, 1.2 · A GeV ^{40}Ar + KCl, and 1.8 · A GeV ^{40}Ar + Pb. While the 4π detector allowed detection of many pions in each event, improving the statistics in the experiments, most of the pions were at large relative momentum differences, where the correlation effect is minimal.

In the 1980's Zajc *et al.*[1] conducted several experiments at the LBL Bevalac using a magnetic spectrometer and two beam–target combinations (1.8 · A GeV ^{40}Ar + KCl and 1.8 · A GeV Ne + NaF). These experiments allowed good statistics at low values of the momentum difference, while introducing the complication that the background was not as well determined as in the 4π streamer chamber experiment and also contained larger residual correlations. This work uses a modified form of the spectrometer used in those experiments.

In 1986, Beavis *et al.*[25] (see also [26] and [22]) measured the pion source size as a function of the negative pion multiplicity (denoted here $N_{\pi-}$) of the nuclear collision. The reaction studied was 1.8 · A GeV Ar + Pb. The results were, for $2 \leq N_{\pi-} \leq 7$, R = 3.59 ± 0.71 fm and, for $11 \leq N_{\pi-} \leq 20$, R = 5.97 ± 0.52 fm, where the function fit is the single radius parameter fit as discussed in Section 7.7 and Chapter 3. This showed that for this asymmetric system, the measured source size depends on the pion multiplicity and, therefore, the centrality of the collision.

In that same year, Humanic made[27] a comparison of the source size of pions generated by the nuclear collision simulation code CASCADE and the data of Zajc *et al.*[1] and Beavis *et al.*[23, 24]. While the agreement was generally acceptable, the small values of the parameter λ observed were not predicted by CASCADE.[7]

Other experiments at the Bevalac include the Plastic Ball[28], where a fast/slow scintillation combination was used to provide dE/dX and E_{total} information for a $\sim 4\pi$

[7]The data from [1] are included in Table 7.4 and the predictions from [27] are included in Table 8.2.

solid angle. Unfortunately the granularity of the detector (and possibly other effects) did not allow a very good measurement of the correlation function. The systems used were 650 · A MeV Nb + Nb and 650 · A MeV Au + Au. In the HISS (Heavy Ion Spectrometer System) facility, the correlation function was measured using a magnetic spectrometer and drift chambers for Ar + KCl (making this projectile–target combination one of the most popular for measuring the correlation function). These data are still under analysis as of the writing of this thesis[29].

Chapter 3

Motivation and Theory

3.1 Motivation

Virtually all the computer codes[30] that are being used to predict the properties of nuclear collisions at the present time are transport codes of one form or another. Since it is desirable to be able to predict the properties of the collision as a function of the impact parameter, almost all of the codes have the ability to locate the nucleons in space. Since pion production is part of the nuclear collision, these codes are capable of predicting the density of the pion sources in space. The codes that allow scattering of the pions generally allow one to modify "sources" to mean the location of the last scattering of the pion before it leaves the collision. So, if nuclear transport codes are to be able to correctly predict quantities that reflect the nucleon distributions during the course of the nuclear collision then they must be able to correctly predict the pion source size.

The difficulty is in generating the theoretical source size to compare to the measured sizes.[1] This has been done in the case of $1.70 \cdot$ A GeV ^{56}Fe + Fe, using the Cascade model[27, 32], which is part of the data reported here. In principle, predicted source sizes (in the parameterization of the correlation function used in this thesis) for all of the computer codes in use, could be generated for all of the reactions studied here. Because of the large number of codes and unmanageably large amounts of CPU time that would be required, generating source sizes for all the computer transport codes was not attempted

[1] Zajc[31] gives procedures for symmetrizing large numbers of Monte Carlo pions from the same collision, but one still has to generate the pions.

in this thesis but was left for those who have developed (or will develop) the codes.

3.2 Derivation of Bose–Einstein Correlations

Suppose[2] that a pion is emitted at the (four–vector) position $\mathbf{R}_1$, a second pion is emitted at $\mathbf{R}_2$ and the momenta of the pions are measured by two detectors, giving momentum $\mathbf{P}_1$ at position $\mathbf{X}_1$ and $\mathbf{P}_2$ at $\mathbf{X}_2$. Assuming that the pions are indistinguishable (including knowing where the pions came from) then, since the pions are bosons, the wave function describing the pions must be symmetric under interchange of the particle labels, that is under interchange of $\mathbf{R}_1$ and $\mathbf{R}_2$ in the wave function. This is equivalent to allowing either of the particles to have come from $\mathbf{R}_1$ or $\mathbf{R}_2$.

Assuming further that the particles may be described by plane waves, then the pion wave function is (in units such that $\hbar = c = 1$)

$$\Psi(\mathbf{P}_1, \mathbf{P}_2) \propto \frac{1}{\sqrt{2}}(e^{i\mathbf{P}_1(\mathbf{X}_1-\mathbf{R}_1)}e^{i\mathbf{P}_2(\mathbf{X}_2-\mathbf{R}_2)} + e^{i\mathbf{P}_1(\mathbf{X}_1-\mathbf{R}_2)}e^{i\mathbf{P}_2(\mathbf{X}_2-\mathbf{R}_1)}) \qquad (3.1)$$

where the usual definition for the dot product of four–vectors is used

$$\mathbf{P}_i\mathbf{X}_i = \vec{p}_i \cdot \vec{x}_i - E_i t_i \ .$$

The probability of a given state (relative to the same state without the Bose–Einstein symmetrization) is $\Psi \cdot \Psi^*$, which is

$$|\Psi(\mathbf{P}_1, \mathbf{P}_2)|^2 \propto 1 + \frac{1}{2}(e^{i(\mathbf{R}_1-\mathbf{R}_2)(\mathbf{P}_1-\mathbf{P}_2)} + e^{-i(\mathbf{R}_1-\mathbf{R}_2)(\mathbf{P}_1-\mathbf{P}_2)}) \ . \qquad (3.2)$$

Assuming that in a heavy ion collision all the pion sources act incoherently,[3] and are distributed according to the distribution function $\rho(\vec{x}, t)$, then the two pion counting rate is

$$\mathcal{P}(\mathbf{P}_1, \mathbf{P}_2) \propto \iint \rho(\vec{r}_1, t_1)\rho(\vec{r}_2, t_2)|\Psi(\mathbf{P}_1, \mathbf{P}_2)|^2 \, d^4\mathbf{R}_1 \, d^4\mathbf{R}_2 \ . \qquad (3.3)$$

The integrals over position are to be taken over all space. In the time integrals, the time between the nuclear collision and detection of the particles is assumed to be sufficiently long that the limits may be extended to all times with negligible error.

[2] This derivation follows that of [33].

[3] Here incoherently is defined as (probability of a pion in state i and a pion in state j) = (probability of a pion in state i) × (probability of a pion in state j), where the Bose–Einstein symmetrization is to be considered shut off. See Section 3.5 for more detail.

The corresponding two pion counting rate without the Bose–Einstein symmetrization is

$$\mathcal{P}'(\mathbf{P}_1,\mathbf{P}_2) \propto \iint \rho(\vec{r}_1,t_1)\rho(\vec{r}_2,t_2)\, d^4\mathbf{R}_1\, d^4\mathbf{R}_2 \ . \tag{3.4}$$

Assuming the normalization

$$\int \rho(\vec{r}_1,t_1)\, d^4\mathbf{R}_1 = 1 \ , \tag{3.5}$$

then Eq. 3.4, becomes

$$\begin{aligned} \mathcal{P}'(\mathbf{P}_1,\mathbf{P}_2) &\propto \int \rho(\vec{r}_1,t_1)\, d^4\mathbf{R}_1 \int \rho(\vec{r}_2,t_2)\, d^4\mathbf{R}_2 \\ &\propto 1 \ . \end{aligned} \tag{3.6}$$

With a little algebra, the equation for the rate with the Bose–Einstein symmetrization included, Eq. 3.3, becomes

$$\mathcal{P}(\mathbf{P}_1,\mathbf{P}_2) \propto 1 + |\tilde{\rho}(\vec{q},q_0)|^2 \ , \tag{3.7}$$

so that the ratio of the two pion counting rate with Bose–Einstein symmetrization to the rate without is

$$\begin{aligned} C_2(\mathbf{P}_1,\mathbf{P}_2) &= \frac{\mathcal{P}(\mathbf{P}_1,\mathbf{P}_2)}{\mathcal{P}'(\mathbf{P}_1,\mathbf{P}_2)} \\ &= 1 + |\tilde{\rho}(\vec{q},q_0)|^2 \ , \end{aligned} \tag{3.8}$$

where

$$\vec{q} = \vec{p}_2 - \vec{p}_1 \tag{3.9}$$

$$q_0 = |E_2 - E_1| \tag{3.10}$$

$$\begin{aligned} \tilde{\rho}(\vec{q},q_0) &= \iint e^{i(\vec{q}\cdot\vec{x}+q_0 t)}\rho(\vec{x},t)\, d^3\vec{x}\, dt \\ &= \text{the Fourier transform of } \rho(\vec{x},t). \end{aligned} \tag{3.11}$$

Some of the properties of the probability are: First, the symmetry under interchange of $\mathbf{P}_1$ and $\mathbf{P}_2$ in Eq. 3.3 implies that $\tilde{\rho}(\vec{q},q_0)$ is an even function in both $\vec{q}$ and q_0, so that the absolute value in Eq. 3.10 is not strictly necessary, and the order of $\vec{p}_1$ and $\vec{p}_2$ in Eq. 3.9 is not important. Second, the probability of emission is increased relative to the probability of emission of identifiable particles for small values of $\vec{q}$ and q_0. Third, for Fermions the plus sign in Eq. 3.8 becomes a minus sign and the emission at small $\mathbf{Q}$

is suppressed. Last, it is possible to justify Eq. 3.8 by saying that for $\Delta x \cdot \Delta p \leq \hbar = 1$ and $\Delta E \cdot \Delta t \leq \hbar$ (where $\Delta x = |r_1 - r_2|$, $\Delta p = |p_1 - p_2|$ and so on) then the uncertainty principle allows the wave functions to overlap, and hence to interfere.

3.3 Correlation Function Used in the Fit

Generally it is not possible to invert the Fourier transform (particularly since what is measured is the square of the absolute value of the Fourier transform), so a source density function with several free parameters is assumed. Its Fourier transform is then calculated, and the free parameters are adjusted for best agreement with the data. The choice of the parameterization used is made according to the physics to be explored.

Fourier transforms have the general property that large scale features transform to small scale features. For example, the overall normalization of the number of pion emitters, a property of the integral of $\rho(\vec{x}, t)$ over all space, transforms to the property that the intercept of the correlation function at $\mathbf{Q} = 0$ is $C_2(\mathbf{Q} \rightarrow 0) = 2$ (this is best seen by setting $\mathbf{P_1} = \mathbf{P_2}$ in Eq. 3.2 and then substituting the result into Eq. 3.3). Because the finite amount of data that can be taken in a realistic experiment restricts the resolution of the correlation function, which is roughly the Fourier transform of the pion source density, only the larger features of the pion source density are well determined. These are the lifetime and the radius parameters in the two directions that the spectrometer can determine, the radius parameter parallel to the beam and the radius perpendicular to the beam (the spectrometer cannot determine the impact plane).

In this experiment the source density $\rho(\vec{x}, t)$ is assumed to be the Gaussian

$$\rho(\vec{x}, t) \propto e^{-\left(\frac{r_\perp}{R_\perp}\right)^2 - \left(\frac{r_\parallel}{R_\parallel}\right)^2 - \left(\frac{t}{\tau}\right)^2} \tag{3.12}$$

Where the notations $\perp$ (and $\parallel$) mean perpendicular (and parallel) to the axis through the collision defined by the beam axis. The parameters $R_\perp$, $R_\parallel$ and τ are the two radius parameters and the lifetime parameter. The Gaussian source density is chosen because the the transform is particularly simple to calculate. Note that other parameterizations will yield similar forms for the correlation function, but the parameters may differ by a multiplicative factor. When comparing data it is essential to check the parameterizations used.

Assuming this source density the probability can be calculated as

$$\mathcal{P}(\mathbf{P}_1, \mathbf{P}_2) \propto 1 + e^{-\left(\frac{q_\perp^2 R_\perp^2}{2}\right) - \left(\frac{q_\parallel^2 R_\parallel^2}{2}\right) - \left(\frac{q_0^2 r^2}{2}\right)} . \tag{3.13}$$

A number of assumptions have been made in deriving these equations and what follows is a discussion some of the important ones. It has been shown that replacing plane waves with Coulomb waves (but retaining the Gaussian source) changes the result by $< 0.1\%$ in the region of $\vec{q}$ important for this effect[34]. Changing from a Gaussian source to a uniform density spherical source (while assuming plane waves) changes the value of the correlation function by less than 2% if $R_{\text{Gaussian}} = 1.52 \cdot R_{\text{uniform}}$[7]. So it is expected that a large variety of sources can be fit with the Gaussian parameterization.

The *a priori* assumption of incoherent sources should be relaxed to allow it to be verified by experiment. If coherent sources were to exist, then the effects of the Bose–Einstein correlations could be increased or reduced or eliminated. This will be discussed further in Section 3.5. Further, if particle misidentification occurs, then the supposed identical particle sample will include a number of pairs of particles of different types which will not interfere. This would lessen the measured effect. To allow for these (and other possibilities) a parameter λ was introduced[35, 14] giving us the correlation function that was fit in this experiment

$$C_2(\mathbf{P}_1, \mathbf{P}_2) = 1 + \lambda e^{-\left(\frac{q_\perp^2 R_\perp^2}{2}\right) - \left(\frac{q_\parallel^2 R_\parallel^2}{2}\right) - \left(\frac{q_0^2 r^2}{2}\right)} . \tag{3.14}$$

The correlation function is usually written with a subscript 2 to indicate that this is a second order (two particle) correlation effect. Further, the normalization assumed is such that for large values of $\vec{q}$, q_0 the correlation function is 1.

There has been an implicit assumption in the choice of the functional form for the source density $\rho(\vec{x}, t)$ since it assumes that ρ has no momentum dependence. The choice for the definition of the experimentally determined correlation function (Eq. 3.15) will allow for a momentum dependence as long as it is the same at all locations, because it will cancel out. However, the momentum dependence cannot be a function of the emission point. Such a momentum dependence could be envisioned as arising from isotropic emission in the local rest frame of an extended, expanding source. Pratt[36] has shown that such a

source would give an apparent source size that would decrease as a function of the pion energy.

3.4 Experimental Correlation Function

In the experiment the correlation function is defined to be the ratio of the two particle cross section to the product of two single particle cross sections with a normalization factor

$$C_2(\mathbf{P}_1, \mathbf{P}_2) = D \frac{\frac{d^6\sigma}{dp_1^3\, dp_2^3}}{\frac{d^3\sigma}{dp_1^3}\frac{d^3\sigma}{dp_2^3}} \tag{3.15}$$

where D is a normalization constant, $d^6\sigma/dp_1^3\, dp_2^3$, the two–pion inclusive cross section, and $d^3\sigma/dp^3$, the single–pion inclusive cross section. While it is in principle possible to measure the various cross sections separately, that is not usually done. Usually, in nuclear collision experiments, the single pion cross sections (the background) are estimated from relative momentum spectrum of like–sign pions from different events (event mixing).

The reasons for using event mixing are outlined below:

Using mixing of unlike–sign pions has the difficulty that the spectrometer can only detect one sign of particle at a time. Assuming that triggering difficulties and the proton contamination could be dealt with, twice the beam time would be needed to do the experiment. There is also the theoretical uncertainty due to the different production rates of π^+ and π^- and the different distributions of the protons and the neutrons in the nucleus.

Using theoretical methods to generate the background has the difficulty that nuclear collisions are not understood well enough to predict what the two–particle momentum spectra would be in the absence of the Bose–Einstein effects. There is also the objection of using the model that is to be tested to generate the data that are supposed to be testing the model.

Simply measuring the single pion momentum spectrum has the difficulty that the number of pions produced in the nuclear collision depends on the impact parameter. Therefore, the requirement of two pions in the spectrometer biases the two–pion trigger towards more central collisions than the one–pion trigger[1]. The one–pion triggered data

would then come from a different class of nuclear collision than the two–pion data and would not be a valid background sample. The only way to properly reproduce the bias is to require that the track–finding routines find two tracks and ignore one — which is the event–mixing technique.

Use of the event–mixing technique requires calculation of the effects of the observed but discarded pions in each of the events that are mixed to form the pseudo–event. This will be discussed in detail in Chapter 6.

3.5 Coherence and the λ Parameter

The parameter λ in Eq. 3.14 has been given the interpretation that if $\lambda = 1$ then the source is fully incoherent, and if $\lambda = 0$ then the source is fully coherent. Before commenting on this interpretation, it is necessary to define both λ and "coherent".

The parameter λ is defined in Eq. 3.14 but there are two possible interpretations. The first interpretation is the value of λ that would be obtained in the limit of infinite information about a single nuclear collision, which will be denoted λ_{true}. The second is the value of λ that would be obtained from applying the event–mixing technique to a data sample of arbitrarily large size, which will be denoted λ_{obs}.

In elementary optics "coherent" is defined as knowledge of the electric field at one location allows one to predict the electric field at another location (in the radiation field). This definition makes no mention of the number of photons present, and applies even if one photon at a time passes through the apparatus. Glauber[5] termed this "first order" coherence and pointed out that this level of information was insufficient to determine the outcome of a correlation experiment, which requires two photons.

Definitions of second order coherence are based on properties of two photons. A simplified form of Glauber's definition of second order coherence[5] is

> (probability of a photon in state i and a photon in state j)^2 = (probability of a photon in state i) $\times$ (probability of a photon in state j)

The definition of incoherence then is

> (probability of a photon in state i and a photon in state j) = (probability of a photon in state i) $\times$ (probability of a photon in state j)

Although photons are used here, any particle could be used. In particular, for a two pion correlation experiment one would replace "photon" with "pion".

An example of a second order coherent source is a laser. The important feature of the laser for second order coherence is the amplification technique, not the monochromatic nature of the light. Amplification by stimulated emission results in many photons leaving the laser in the same state.[4] Therefore, if there is a photon in a given state it is extremely likely that there is a second photon in the same state, and this state is the only state populated by photons. Taking extremely likely to be 100%, the probabilities (as a function of the photon momentum) are

$$\begin{aligned} \mathcal{P}(\mathbf{P}_1, \mathbf{P}_2) &= \mathcal{P}(\mathbf{P}_1) \\ &= \mathcal{P}(\mathbf{P}_2) \end{aligned}$$

and the laser is second order coherent. Further, $C_2(\mathbf{P}_1, \mathbf{P}_2) \equiv 1$ and $\lambda_{\text{true}} = 0$.

So if "pion lasers" are the sole source of pions in the nuclear collision then $\lambda_{\text{true}} = 0$. If there are coherent and incoherent sources in the collision then $\lambda_{\text{true}} \leq 1$. Simple arguments show that if the single–particle momentum spectra are the same for the coherent and incoherent sources then

$$\lambda_{\text{true}} = \frac{1}{1+f} \tag{3.16}$$

where f is the ratio of the number of coherent pion pairs to the number of incoherent pion pairs.

The effect of pion lasers on λ_{obs} depends strongly on the event–mixing technique, and underlines the assumption (often not stated) that all events must have the same momentum distribution for the technique to apply. Imagine the simple case where a pion laser is the sole source of pions in all of the nuclear collisions in the experiment. If the pion laser always has the same orientation, then event mixing produces the true background and $\lambda_{\text{obs}} = 0$. If the pion laser changes orientation randomly from one event to the next (for example, the first $\Delta(1236)$ to decay triggers the laser and determines the direction) then the real spectrum will be a δ–function. The background calculation will mix pions of random orientation, and hence the spectrum will be flat. The ratio of the two will be a δ–function and λ_{obs} will be arbitrarily large.

[4] Note that all photons leaving the laser in the same state is symmetric under interchange of particle labels and the symmetrization imposed in Section 3.2 does not apply.

Pion lasers are not the only mechanism that can induce second order correlations. Decay of resonances (where conservation of momentum is a factor), and dynamical correlations (where ρ depends on $\vec{p}$ through the dynamics of the collision) can influence the value of λ[37].

Chapter 4

Apparatus

4.1 The Bevalac Accelerator

The heavy ion beams for this experiment were provided by the Bevalac accelerator at Lawrence Berkeley Laboratory. They were transported to the experiment using beam line 30–2, which consists of magnetic dipole and quadrapole magnets. The parameters for the beams used are given in Table 4.1.

Ion	Energy	Typical Intensity	Beam Spot Size	Year
^{40}Ar	1.82 · A GeV	$1 \cdot 10^8$ Ions/spill	1 cm × 1.6 cm	1986
^{56}Fe	1.70 · A GeV	$1 \cdot 10^7$ Ions/spill	1 cm × 6 cm	1982
^{93}Nb	1.54 · A GeV	$2 \cdot 10^7$ Ions/spill	1 cm × 1 cm	1986

Table 4.1: Beam parameters for the runs.

4.2 The Janus Spectrometer

The Janus spectrometer, as shown in Figs. 4.1 and 4.2, consists of two dipole magnets, a "C" magnet near the target, and a window-frame magnet that is called the "Janus" magnet (after the Roman god). Between the C magnet and the Janus magnet are two wire chambers, and after the Janus magnet are two more wire chambers. The first pair of chambers define the in-going (to Janus) vector, and the second pair of chambers define the out-going (from Janus) vector. The deflection in Janus gives the particles' momentum.

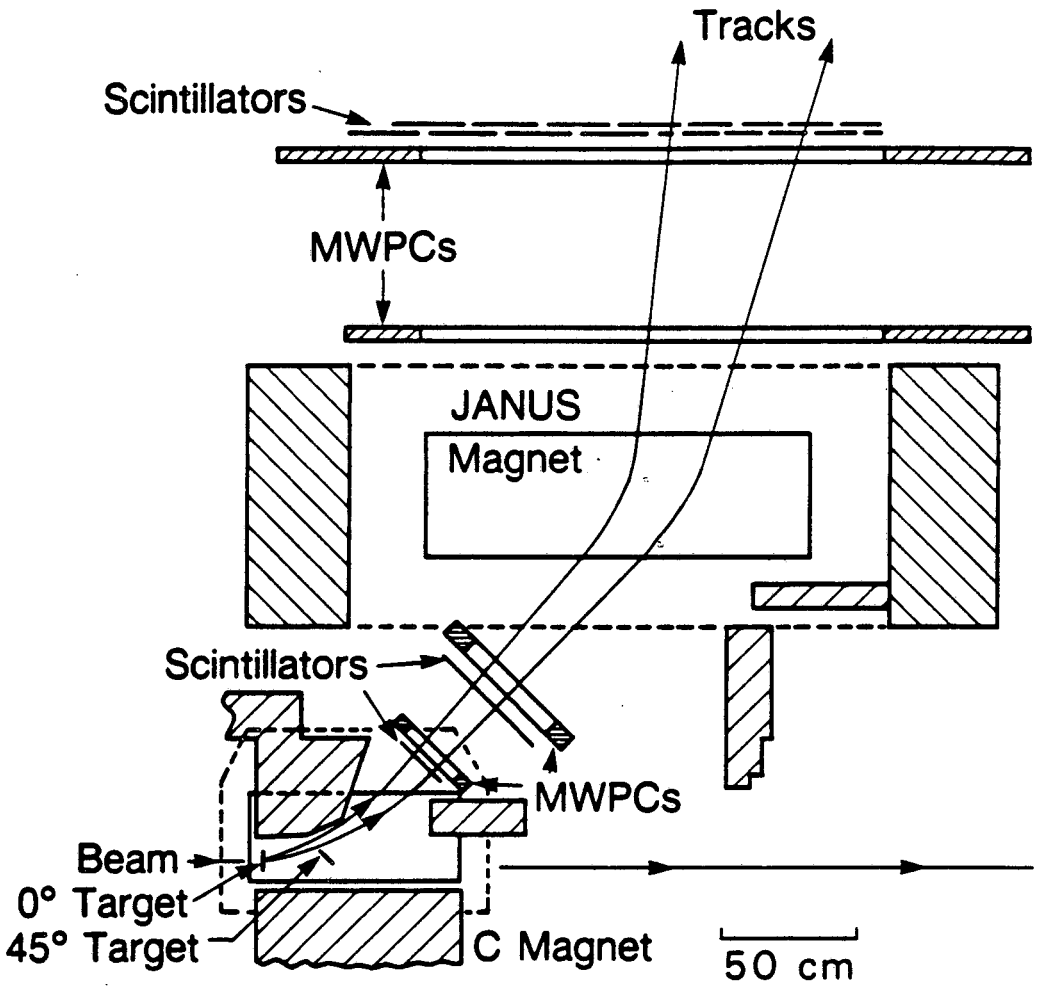

Figure 4.1: The Janus spectrometer in the plan view (1982).

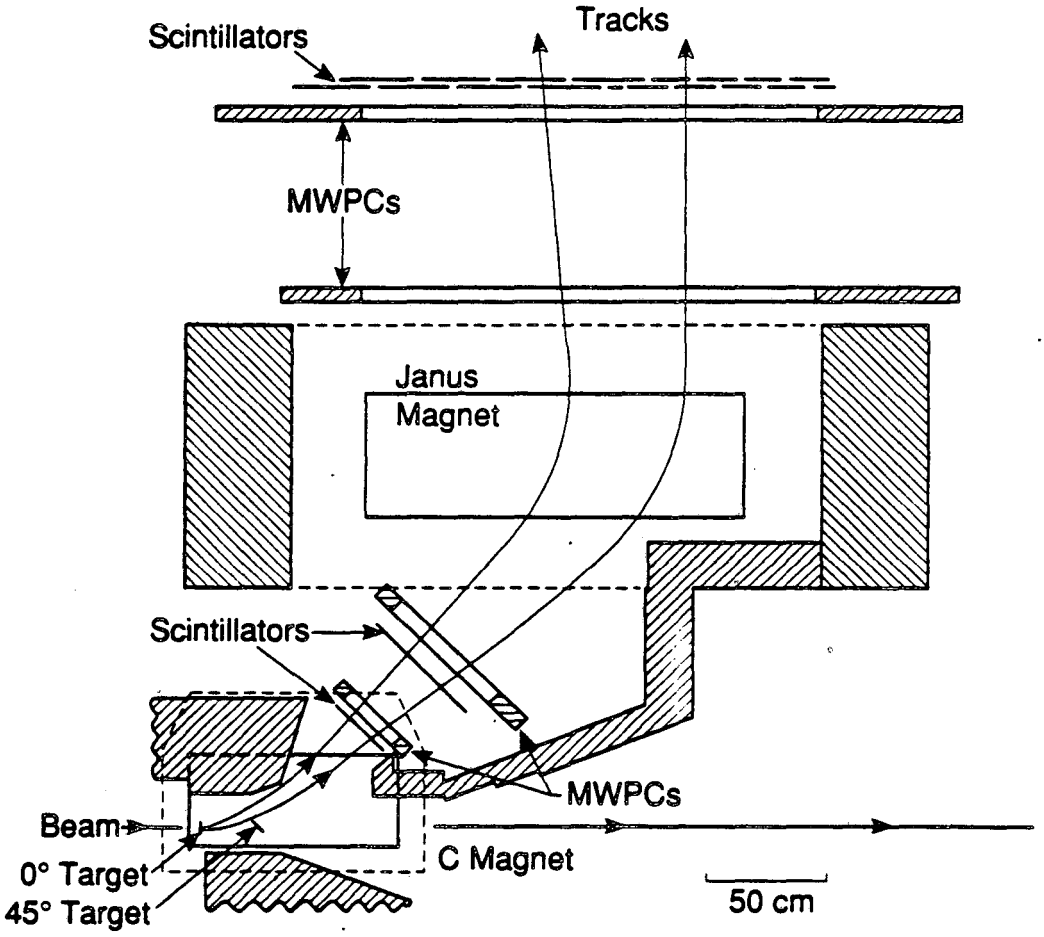

Figure 4.2: The Janus spectrometer in the plan view (1986). The spectrometer was modified between the runs by adding lead walls to protect the second wire chamber from δ–rays produced by the beam interacting with the air downstream of the target, and replacing the second wire chamber.

There are also a number of scintillation counters for triggering, time of flight determination and energy–loss measurement. Figure 4.1 shows the spectrometer as run in 1982 and Figure 4.2 shows the spectrometer as run in 1986. The spectrometer was modified between the runs by adding lead walls to protect the second wire chamber from δ–rays produced by the beam interacting with the air downstream of the target, and replacing the second wire chamber.

The detailed description of the components will be given in approximate order of distance from the exit window of the beam line. The C magnet has a pole tip size of 91.4 cm by 40.6 cm and a pole gap of 20.0 cm. In this configuration the magnet can give fields in the range of about 1 KG to about 14 KG. The magnet was mapped after the Fe data were taken using a field mapper from the Magnetic Measurements group. The field mapper measured the voltages across three orthogonal search coils as they were moved through the field volume. The data from the mapper were processed on the BEVAX VAX–11/780. The field mapper and processing techniques used are similar to those used for the Janus magnet in an earlier experiment[1].

	Target			Magnet fields	
Set-up	Material	Position	angle	C magnet	Janus magnet
Ar 0°	KCl	26.0 cm	90°	14.6 KG	12.0 KG
Ar 45°	KCl	2.8 cm	45°	1.7 KG	9.0 KG
Fe 0°	Stainless Steel	26.0 cm	90°	14.2 KG	11.4 KG
Fe 45°	Fe	0.0 cm	45°	0.0 KG	8.6 KG
Nb 0°	Nb	26.0 cm	90°	13.0 KG	10.8 KG
Nb 45°	Nb	0.0 cm	45°	1.5 KG	8.5 KG

Table 4.2: Spectrometer parameters for the set-ups used.

The target materials used in this experiment are given in Table 4.2. The targets were placed in a target holder that rested on the lower pole tip of the C magnet. This places a restriction on the choice of target in that it cannot be magnetic if the C magnet is used. For this reason the target used in the 0° Fe runs was #304 stainless steel. The composition of the stainless steel target (as given by the supplier, Castle Metals — A. M. Castle & Co.) is given in Table 4.3. For the Ar run a KCl target was used to avoid the

necessity of using a cryogenic target. Since the properties measured depend on the mass number of the colliding species the slight difference in mass was not important. Targets 0.5 to 1.0 gm/cm^2 thick were used in all cases as a compromise between the data–taking rate and the multiple scattering in the target. At this thickness, and for the materials used, the multiple scattering in the target is approximately equal to that in the first two wire chambers and counters.

Element	Amount
Fe	70.9 %
Cr	18.5 %
Ni	8.5 %
Mn	1.6 %
Si	0.5 %

Table 4.3: Stainless steel target composition. Percentages are by weight.

The target location and orientation used depends on the desired acceptance, as do the magnetic fields. This information is contained in Table 4.2. The origin for the coordinate system is taken as the 45° target position and positive is upstream. The angle is the angle between the target plane and the beam direction, 45° being such that the target is facing the Janus magnet.

The first scintillation counter (S1) is 30.5 cm by 15.2 cm and 0.18 cm thick. The photomultiplier tube used is an XP2020 with an active base suitable for high count–rate environments.

The first wire chamber follows S1. The active area is 30.5 cm by 15.25 cm and contains about 400 wires. The wire spacing is 0.2 cm and the distance between sense planes is 1.4 cm. The first plane of wires (closest to the target) is angled at 45°, the second plane is strung at 90° (vertically), and the last plane is strung at 0° (horizontally). It is read out by a wire chamber readout system designed and built at LBL[38].

The second scintillation counter is actually two counters side–by–side (called S2A and S2B — S2A is upstream). The active area is 55.9 cm by 19.1 cm and is equally split by the two counters, which overlap slightly. The counters are 0.18 cm thick. These counters are each viewed by an RCA 8575 phototube on a standard LBL base. These counters are

used to determine the start of the time of flight since it was felt that the lower counting rates in S2 than in S1 would allow a better determination of the start of the event.

The second wire chamber follows the S2 counters. During the Fe runs, the wire chamber used was 52 cm by 19.4 cm in active area. The full height was 40 cm, but some of the horizontal wires were not used. The order of the planes in this wire chamber was, the first plane was 0°, the second was 90° and the last plane was −45°. The negative angle means that the upstream end of the wire is lower than the downstream end. The wire spacing was 0.2 cm for 0° and the 90° planes and 0.3 cm for the −45° plane. Between the first and second sense planes the spacing was 1.2 cm, and between the second and the third sense planes the spacing was 2.2 cm. The wire chamber contained about 600 wires, and was read out by the LBL wire–chamber read–out system.

For the Ar/Nb runs a different second wire chamber was used.[1] The new wire chamber had an active area of 57.6 cm by 19.2 cm. The full height of the wire chamber is 32.0 cm but, again, not all of the horizontal wires were used. The order of the planes in this chamber is 0°, 90° and then −45°. The wire spacing is 0.2 cm in all sense planes and the spacing between the sense planes is 1.4 cm, This chamber contains about 700 active wires, and it is read out by a LeCroy PCOS3 wire chamber readout system.

The Janus magnet follows wire chamber two. This magnet has a pole tip size of 167.6 cm by 55.9 cm, and a pole gap of 21.4 cm. The magnetic field of the Janus magnet was mapped for an earlier experiment[1].

Following the Janus magnet are wire chambers three and four. These wire chambers are electrically identical, and the active areas are 200 cm by 25 cm. The sense planes for these wire chambers are strung with the wires at −30°, 90° and then 30°. The wire spacing is 0.2 cm in all sense planes, and the spacing between sense planes is 1.4 cm. These chambers are composed of about 2,000 active wires (each) and are read out by the LBL wire chamber readout system.

The last counters that the particles go though are the AB counters. These are two rows of counters (the B's are closer to the target), with eight A counters and ten B counters. The counters are 0.7 cm thick and have an active height of 30.5 cm. Three different widths are used (33.1 cm, 19.1 cm and 9.5 cm), which are staggered (as shown

[1]The original wire chamber had been returned to its owners at the end of the Fe run and it was unavailable for these runs.

in Figs. 4.1 and 4.2) to give 17 possible overlaps. The staggering gives the finest possible granularity for the number of counters, which becomes finer towards the high momentum end (the downstream end) of the array. Some of these counters were first used in 1979, and the pulse height resolution has degraded noticeably in the older counters. This was considered acceptable for this experiment since the time of flight information alone can give particle identification for most of the accepted momenta.

Downstream of the target, and not on the flight path of the pions, is an ion chamber used to monitor the beam intensity[1]. The output is passed to an Ortec 439 current integrator and then to the CAMAC where it is the recorded by the computer.

The signals from the various parts of the experiment were lead out of the experimental area to the electronics shack, were the trigger logic is made. The remainder of the description of the electronics is given in the next section.

The acceptance of the spectrometer for the Fe setup is given on a rapidity vs. $P_\perp$ plot in Fig. 4.3. The data shown are Monte Carlo data, with one track per event, weighted to reflect the particle emission probability[39, 40]. The figure contains both the 45° and the 0° acceptances. The lines marked "A" are the lower of the two momentum cuts employed for each of the two acceptances. The lines marked "B" are the higher of the two momentum cuts employed. These cuts are explained in detail in Chapter 6, and the values will be repeated here. For the 45° data, the cuts were $|\vec{p}_{\rm cm}| > 100$ MeV/c and $|\vec{p}_{\rm cm}| > 150$ MeV/c. For the 0° data the cuts were $|\vec{p}_{\rm proj}| > 50$ MeV/c and $|\vec{p}_{\rm proj}| > 100$ MeV/c. Table 4.4 gives the corresponding spectrometer characteristics.

θ_{lab}	θ_{cm}	$\|\vec{p}_{cm}\|$, accepted	Solid Angle
$\sim 0°$	$(0°, 32°)$	(100, 400) MeV/c	12 msr
$\sim 45°$	$(91°, 106°)$	(100, 600) MeV/c	29 msr

Table 4.4: Spectrometer characteristics for the Fe setups.

Table 4.5 gives the locations of the effective edges of the magnets, and the centers of the wire chambers. Using these positions, the field values from Table 4.2 and the effective edge approximation, one can reproduce the acceptance of the spectrometer. The coordinate system used is: the beam direction is $-\hat{y}$, $\hat{z}$ is vertical and $\hat{x}$ is perpendicular to the beam direction. The values are for the Ar/Nb setup, the values for the Fe set up

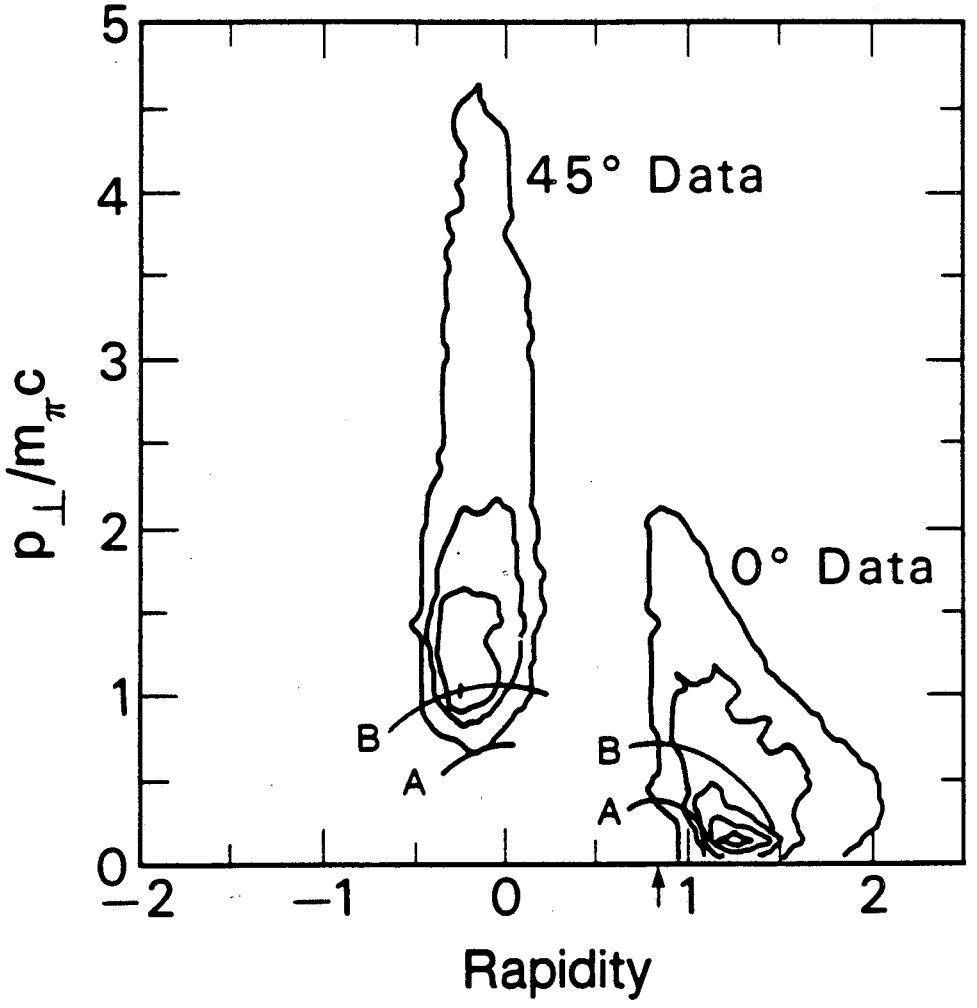

Figure 4.3: Contour plot of the acceptance for the Fe setups, both 45° and the 0°. The arrow marks the beam rapidity, The lines marked "A" are the lower of the two momentum cuts employed each acceptance, the lines marked "B" are the higher of the two cuts.

	location (cm)		
item	x	y	z
Beam direction	–	$-\hat{y}$	–
Target position	–	26.0 to 0.0	–
C magnet effective edge	41.0	–	–
Wire Chamber 1	48.7	−48.2	0.1
Wire Chamber 2	78.5	−80.2	−0.1
Janus magnet effective edge	126.6	–	–
Janus magnet effective edge	204.8	–	–
Wire Chamber 3	237.8	−142.6	−0.6
Wire Chamber 4	316.9	−142.4	−0.2

Table 4.5: Locations of the principle components of the Janus spectrometer as used in 1986.

are similar. The effective edge approximation is discussed in detail in Chapter 5.

4.3 Fast Electronics and Computer Readout

The trigger logic used in this experiment is given in Figs. 4.4 and 4.5. A few comments about the trigger logic diagram will be made here. The "Run Gate" was the output from a Jorway output register, and was used to allow the computer to enable and disable the triggers to start and stop the runs. The "Computer Free" was the inverse of the "Computer Busy" output from the trigger module that was set when the module was triggered, and remains set until the trigger was cleared by the computer. The "Fast Hold Off" (from "Event" to the "Master Gate") was used to disable the "Master Gate" until the "Computer Busy" can be asserted.

Once the event was triggered the data were acquired using standard CAMAC modules, read out by a program running on a Bi Ra MBD–11 connected to a computer. For the Fe data the computer was a PDP–11/45, and for the Ar/Nb data the computer was a VAX–11/750. The PDP–11/45 based system could acquire about 200 events per spill (limited by the tape writing during the spill), whereas the VAX–11/750 based system could acquire

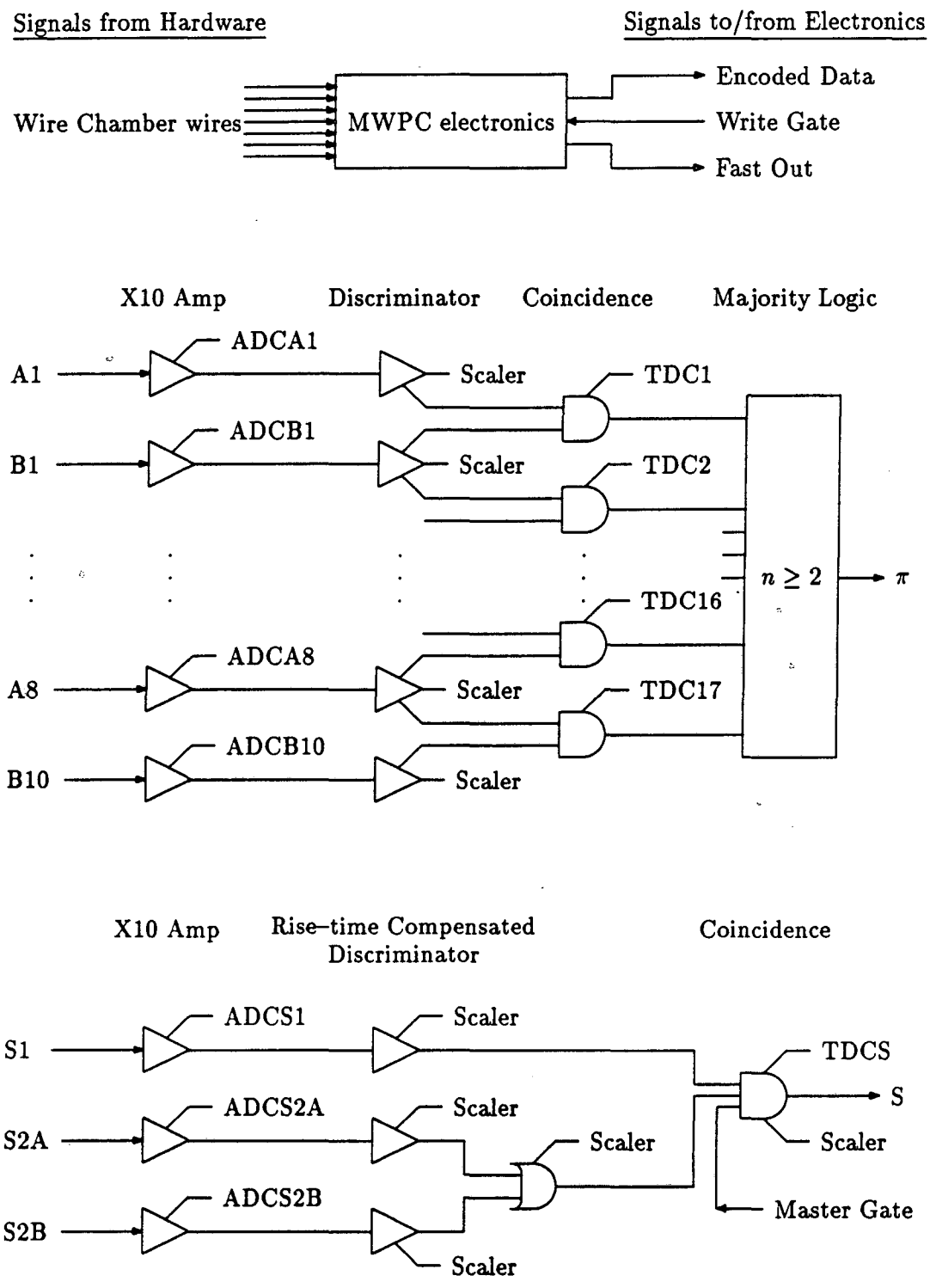

Figure 4.4: Trigger logic part 1.

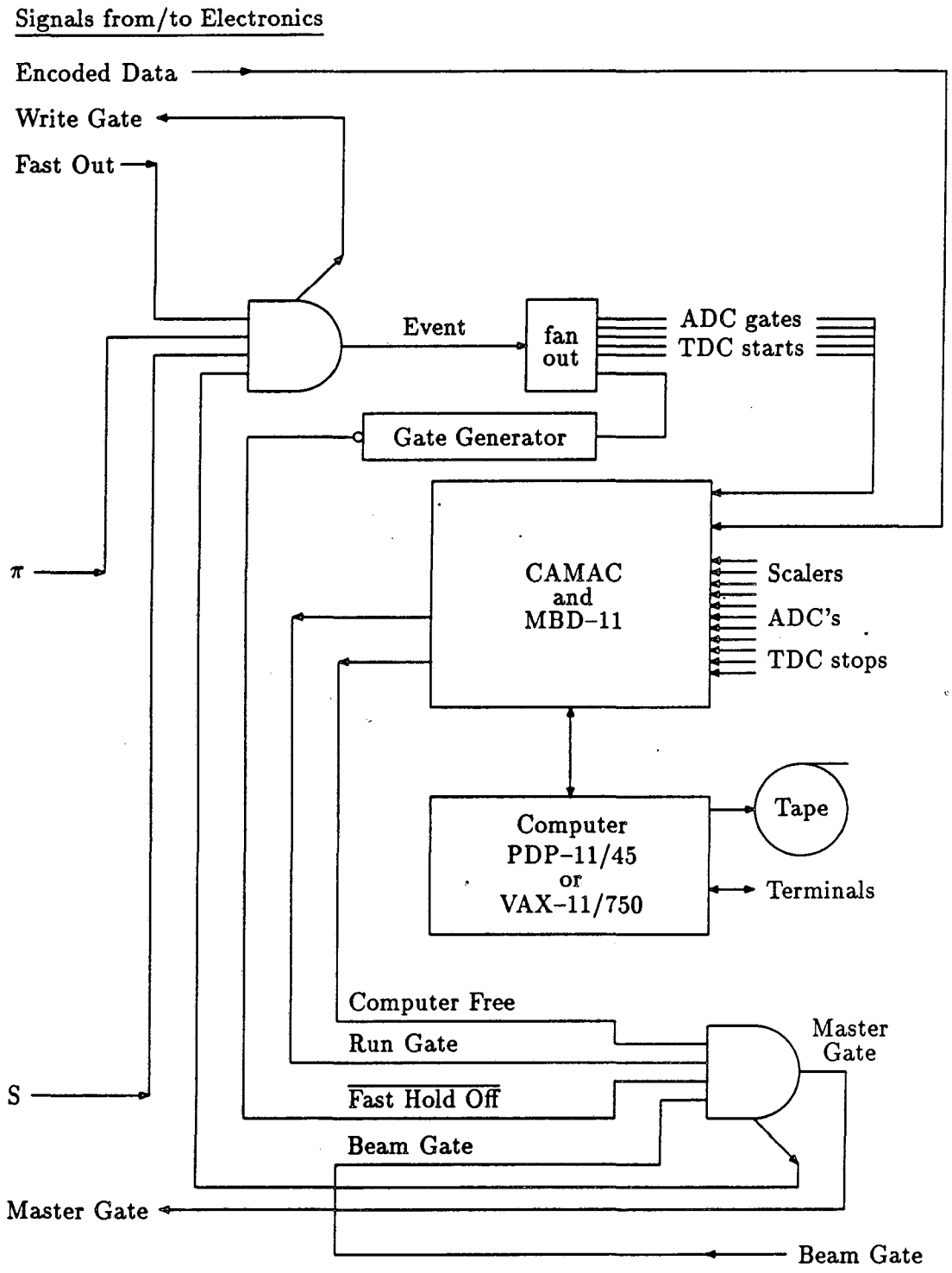

Figure 4.5: Trigger logic part 2.

about 300 events per spill (limited by the event read–out speed). In addition, the VAX–11/750 based system could do significantly more on–line analysis.

The slow logic, used to synchronize the experiment and the computer to the accelerator beam spills, is shown in Fig. 4.6. When the VAX–11/750 based system was in use, the "Start of spill" and "End of spill" events were used to disable the 11/750's analysis of event data during the spill so the 11/750 could transfer data into its memory at the largest rate possible.

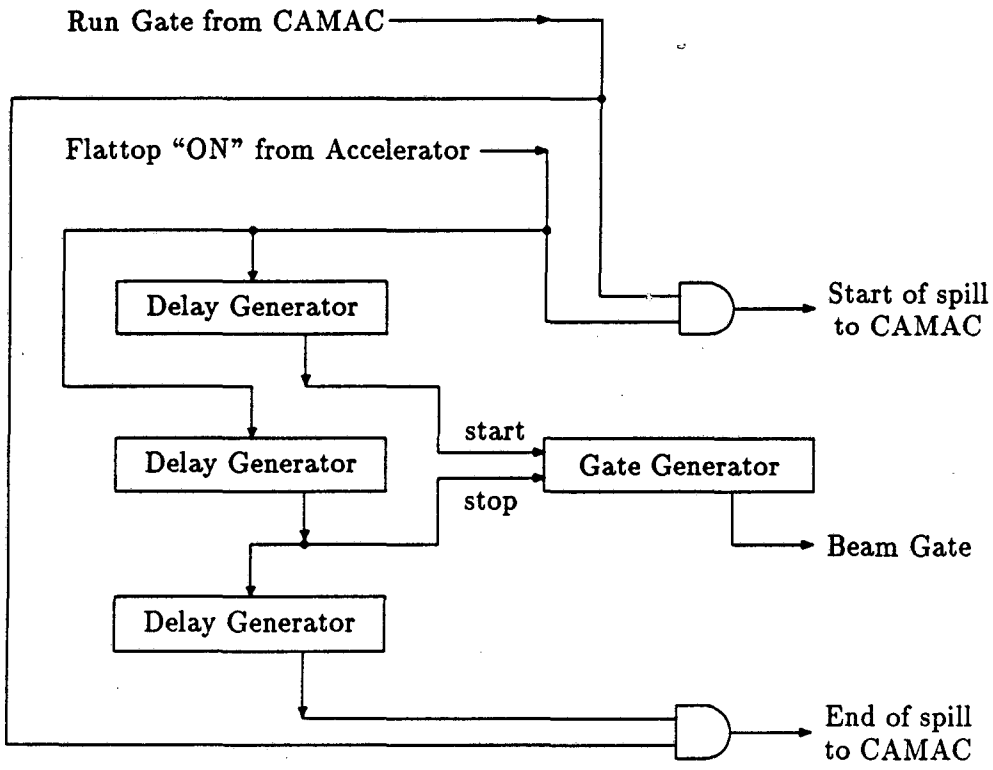

Figure 4.6: Slow Logic.

The data acquisition programs running in the MBD–11 and the PDP–11/45 (or VAX–11/750) were the Q system[41]. These programs were written (and maintained) by the MP–1 group at Los Alamos[2] and the Real Time Systems group at Lawrence Berkeley Laboratory. The author wishes to thank the group for the use of their programs and their efforts in correcting the few bugs that showed up during the experimental runs.

[2]In 1988, the MP–1 group became Group MP–6, LAMPF, Los Alamos National Laboratory.

Chapter 5

Track finding and Particle Identification

5.1 Outline of the Problem

Track finding and particle identification in the two pion experiment are broadly divided into three tasks. First, there is finding the hits in the wire chambers given the raw data (the wire numbers of the struck wires). Second, there is finding the tracks given the hits in the wire chambers. Third, there is particle identification, and momentum determination for each track found. The programs (or subroutines) to accomplish the earlier tasks are faced with the simultaneous requirements of being fast enough to look at almost every event in the experiment, but also complete enough not to introduce statistical biases that will complicate the later analysis. This must be done in an experiment that requires two tracks in the spectrometer for a good event. In addition, the region of most interest, that of low momentum differences, is where the two tracks are physically close together and, therefore, easier to confuse. A further complication for the Fe data set was that the track finding was originally done on a PDP–11/45 and the program had to fit into the address space allowed by the 16 bit addressing.

The size of the calculation task is illustrated with the track finder. In the ideal case of just two real tracks, there are four possible out–going (from the Janus magnet) tracks defined by the two hits in each of the two rear wire chambers. Similarly, there are four

possible in-going (to the Janus magnet) tracks defined by the two hits in each of the two front wire chambers. Therefore, the eight hits in the four wire chambers define sixteen possible candidates for the first track (once the first track is found, there is only one choice for the second track in this case). Although some of the candidates for the track can be eliminated early in the calculations, since the candidate is obviously bad, the presence of stray particles striking the wire chambers increases the number of candidates to consider and, to an order of magnitude, the number of candidates that have to be considered for the first track is an order of magnitude larger than the number of events.

5.2 Hit Finding

The hit finding routines work as follows: The wire chambers were positioned so that the tracks were approximately perpendicular to the wire chambers. It is then possible to ignore the dimension perpendicular to the wire chamber, which is approximately parallel to the particle's path, approximating the three separated sense planes of the wire chamber by three sense planes which are superimposed. If a particle goes though the wire chamber and fires all three planes, the hit will be located by the three fired wires that pass through a single point. In general, due to the finite resolution of the wires and non-normal tracks, the three wires will not define a single point, but will define a small triangle. The program must calculate the size of this triangle and use the size to decide if a triplet of wires forms a hit or not. The method chosen must be simple enough to calculate for every possible triplet of wires in every wire chamber for every event.

To derive the method used here, it is first necessary to define the symbols used:

Let N_i be the number of the wire of interest for plane i.

C_i be the number of the wire passing through the center of the wire chamber for plane i.

w_i be the separation of the wires for plane i.

$\vec{n}_i$ be the unit normal to the wire, in the direction of increasing N, for plane i.

In Figure 5.1 these definitions are illustrated in a wire chamber for a single hit within the wire chamber. In this experiment N_i is chosen, for all wire chambers, to increase going

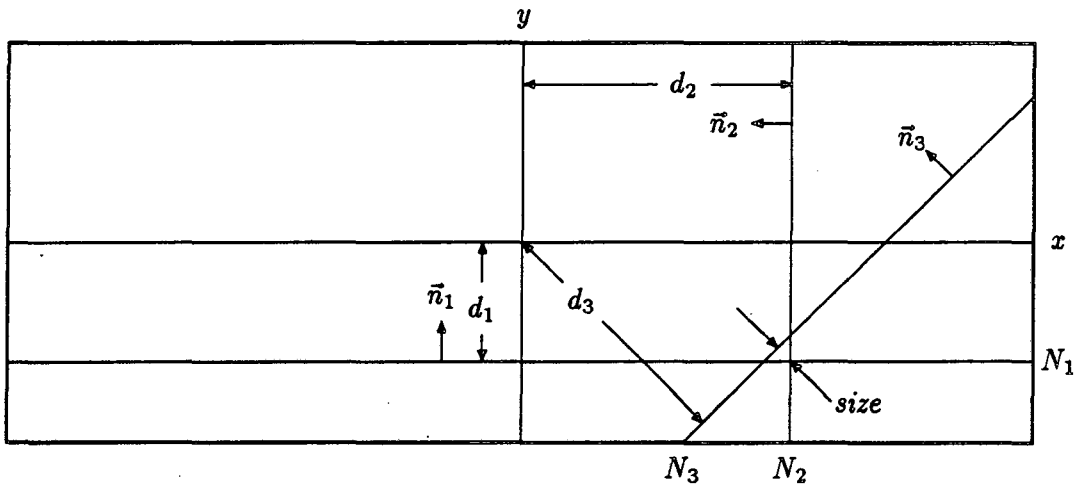

Figure 5.1: A triangle in a wire chamber.

to the left for non-horizontal wires, or up for horizontal wires, as drawn. The (signed) distance from the center of the wire chamber (which is taken as the origin) to the wire is

$$d_i = w_i(N_i - C_i) \tag{5.1}$$

so the wire is given by $\vec{x}$ such that

$$\vec{x} \cdot \vec{n}_i = w_i(N_i - C_i) \tag{5.2}$$

A "cross" is defined as the intersection of two wires. The location of a cross is a simultaneous solution to two of Eq. 5.2 for the two different planes of wires. In component notation this is (x, y) such that

$$x n_{x1} + y n_{y1} = w_1(N_1 - C_1) \tag{5.3}$$

$$x n_{x2} + y n_{y2} = w_2(N_2 - C_2) \tag{5.4}$$

Assuming that

$$\begin{vmatrix} n_{x1} & n_{y1} \\ n_{x2} & n_{y2} \end{vmatrix} \neq 0 \tag{5.5}$$

otherwise the wires are parallel, and none of the wire chambers in this experiment have different planes with parallel wires, the matrix can then be inverted and x and y are given

by

$$\begin{pmatrix} x \\ y \end{pmatrix} = \frac{1}{\begin{vmatrix} n_{x1} & n_{y1} \\ n_{x2} & n_{y2} \end{vmatrix}} \begin{pmatrix} n_{y2} & -n_{y1} \\ -n_{x2} & n_{x1} \end{pmatrix} \begin{pmatrix} w_1(N_1 - C_1) \\ w_2(N_2 - C_2) \end{pmatrix} . \tag{5.6}$$

Putting this into Eq. 5.2 for the third plane, the wire number for the third plane is given by

$$N_3 - C_3 = \frac{w_1}{w_3} \frac{\begin{vmatrix} n_{x3} & n_{y3} \\ n_{x2} & n_{y2} \end{vmatrix}}{\begin{vmatrix} n_{x1} & n_{y1} \\ n_{x2} & n_{y2} \end{vmatrix}} (N_1 - C_1) + \frac{w_2}{w_3} \frac{\begin{vmatrix} n_{x1} & n_{y1} \\ n_{x3} & n_{y3} \end{vmatrix}}{\begin{vmatrix} n_{x1} & n_{y1} \\ n_{x2} & n_{y2} \end{vmatrix}} (N_2 - C_2) . \tag{5.7}$$

Hence, for a triangle of zero size

$$w_1 \begin{vmatrix} n_{x3} & n_{y3} \\ n_{x2} & n_{y2} \end{vmatrix} (N_1 - C_1) + w_2 \begin{vmatrix} n_{x1} & n_{y1} \\ n_{x3} & n_{y3} \end{vmatrix} (N_2 - C_2) + w_3 \begin{vmatrix} n_{x2} & n_{y2} \\ n_{x1} & n_{y1} \end{vmatrix} (N_3 - C_3) = 0 . \tag{5.8}$$

The above equation is included on account of its symmetry and because from it the third wire through a hit can be found if the other two wires are known. The equation used is that which gives the difference between the real N_3 wire and that predicted by the cross of N_1 and N_2

$$\Delta N_3 = \frac{w_1}{w_3} \frac{\begin{vmatrix} n_{x3} & n_{y3} \\ n_{x2} & n_{y2} \end{vmatrix}}{\begin{vmatrix} n_{x1} & n_{y1} \\ n_{x2} & n_{y2} \end{vmatrix}} (N_1 - C_1) + \frac{w_2}{w_3} \frac{\begin{vmatrix} n_{x1} & n_{y1} \\ n_{x3} & n_{y3} \end{vmatrix}}{\begin{vmatrix} n_{x1} & n_{y1} \\ n_{x2} & n_{y2} \end{vmatrix}} (N_2 - C_2) - (N_3 - C_3) . \tag{5.9}$$

There is a small computational complication. The resolution of the wire chambers is half integral (in terms of wire spacings). Since the computers store integers more efficiently than fractional numbers, it is desirable to use twice the wire number instead of the wire number, since twice the wire number is integral. For this reason the equation actually

used is

$$\Delta N_3 = \frac{1}{2}\frac{w_1}{w_3}\frac{\begin{vmatrix} n_{x3} & n_{y3} \\ n_{x2} & n_{y2} \end{vmatrix}}{\begin{vmatrix} n_{x1} & n_{y1} \\ n_{x2} & n_{y2} \end{vmatrix}}(2N_1 - 2C_1) + \frac{1}{2}\frac{w_2}{w_3}\frac{\begin{vmatrix} n_{x1} & n_{y1} \\ n_{x3} & n_{y3} \end{vmatrix}}{\begin{vmatrix} n_{x1} & n_{y1} \\ n_{x2} & n_{y2} \end{vmatrix}}(2N_2 - 2C_2) - \frac{1}{2}(2N_3 - 2C_3)\ . \tag{5.10}$$

The coefficients of $(2N_i - 2C_i)$ are calculated once for the experiment and entered into the codes. The $2C_i$ are entered into the codes, so that the calculation of a triangle size requires 1 addition, 4 subtractions and 3 multiplications, and can be done for each triplet of wires. A further savings could have been realized by clearing the parenthesis and adding all the constants together. However, it was felt that the increased chance for error when varying the center wire numbers offset the possible gain and this was not done.

The hit finding process starts with each triplet of wires being checked against Eq. 5.10 and if the size is less than the maximum size (5 wires) the triplet is considered a triangle and a possible hit.

Experience has shown that hits cannot be allowed to share wires. That is, a single wire cannot be allowed to be part of two different hits. If this is allowed, the distribution of the second hit relative to the first shows clear indications that the number of hits sharing wires is greater than one would expect for a random distribution. So the hit finding proceeds as follows: All triangles smaller than the maximum size are stored as hit candidates. If too many candidates are found the event is rejected to avoid biases. The triangles are ordered by size (smaller first) and each triangle is checked for shared wires with previously found hits. If there are none, the triangle is considered good and is added to the list of found hits and its wires associated with the hit. If there are shared wires then the triangle is rejected. The smallest triangle is, of course, always considered a good hit.

This is best illustrated as in Fig. 5.2, where a typical three hit event is shown. The wire angles are those of the first and second wire chambers, however a similar picture could be drawn for the third and fourth wire chambers. There are potentially five triangles, labelled 1–5, and 3 shared wires, labelled N_1, N_2, and N_3. The four reasonably small hits are labelled 1–4. The requirement of small triangle size eliminates the triangle near 5 as a hit, but the assignment of the hits based on triangle size alone is ambiguous for

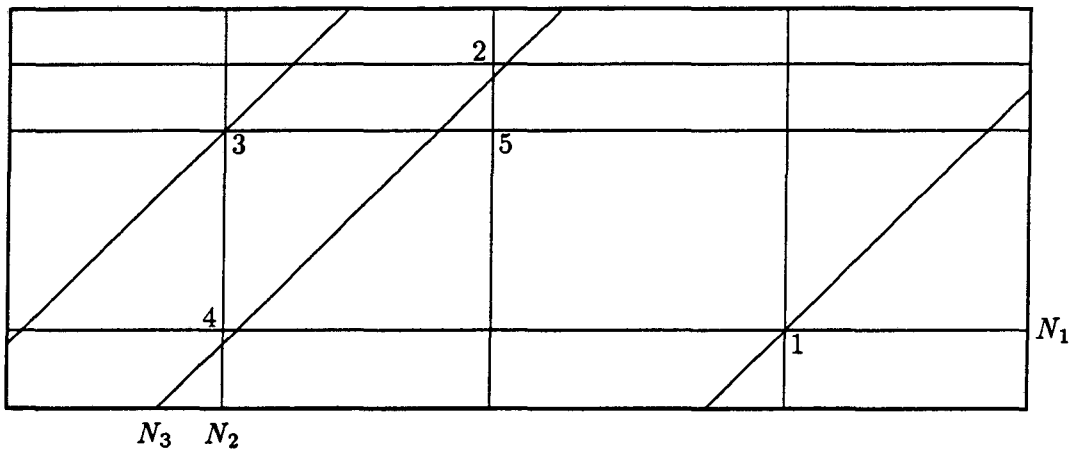

Figure 5.2: Three hits in a wire chamber showing possible shared wires, N_1, N_2, and N_3.

the triangles near 2 and 4. However, following the preference for small triangles, then the wires for the hits near 1 and 3 should be removed, so that it is not possible for these wires to be shared with other hits. It is then clear that 2 is the remaining hit.

It has been assumed that the wire chambers are 100% efficient. In reality, the wire chambers were measured to be about 95% – 99% efficient. Taking 95% as an example, a two–track event with 24 struck wires and efficiency of 95% per wire will give an event efficiency of 0.95^{24}, or 54%. Clearly, it cannot be required that all hits be perfect triangles, but missing wires must be allowed.[1] So the wires that are not associated with good triangles are checked to see if they cross within the chamber boundaries, if so they are called a hit, and the position is recorded. At this stage, hits formed from crosses are allowed to share wires with other crosses.

A side effect of the procedure is that the hits are stored in the arrays as smallest triangles first, then larger triangles, and then crosses. When track finding is done the hit arrays are searched in this order, and the track finding is biased towards smaller triangles.

At this point the number of hits in each chamber is counted. If there are not at least as many hits in each chamber as tracks sought, no further processing of the event is done.

[1]The track–finder's efficiency for using the wires is measured to be about 85%. So from the track–finder's point of view it is essential to allow missing wires. The difference between the track–finder's efficiency and the wire–chamber's efficiency is due to the shared–wire removal in the hit finder and the track finder.

5.3 Effective Edge Track Finding

Before starting with the effective edge work, recall that the Janus spectrometer (see Figs. 4.1 and 4.2) consists of two dipole magnets, the C magnet near the target, and the Janus magnet. Between the C magnet and the Janus magnet are two wire chambers, and after the Janus magnet are two more wire chambers. The deflection in Janus gives the particles' momentum.

Once the hits in the wire chambers have been found, the locations of the hits are passed to the track finding routine. To allow the track finding to proceed at a reasonable pace,[2] the track finding is done in the effective edge approximation, with vertical focussing. In this approximation, the field is assumed to be zero outside the magnet and at (constant) full field inside the magnet. The boundaries for "inside" and "outside" can be chosen to either give the best approximation to the real field in the sense of the real tracks are well fit by the effective edge tracks, or that the deflection given by the effective edge field (when set to the central value of the real field) is a good approximation to the deflection in the real field. Studies of Monte Carlo tracks using the field map show that for Janus the two choices are nearly the same. In the C magnet the effective edge position was chosen to give the best agreement for the target traceback position and initial angles of the momentum vector.

The motion of the particles is either that of a straight line, in the field free regions, or that of a section from a spiral (with the radius determined by the Lorentz force law), in the full field regions. Viewed parallel to the field, the track follows an arc in the full field regions. The fields in the C magnet and the Janus magnet are both vertical, so in the plan view the tracks follow arcs inside the full field regions of the C and the Janus magnet. One can easily show[3] that at the boundaries the track is continuous, the derivatives in the horizontal directions are continuous and the vertical derivative ($\frac{dz}{ds}$) has a jump discontinuity given by

$$\Delta\left(\frac{dz}{ds}\right) = \frac{\tan\theta}{r} z_0 \tag{5.11}$$

where s is the path length, z is the vertical coordinate (z_0 is the height of the path above

[2]The hit and track finding program was originally written to run on a PDP-11/45, and attained a speed of about 10 events per second on the PDP-11/45.

[3]See, for example, [42].

the magnet's mid–plane), r is the radius of curvature, and θ is the angle between the particle's path and the normal to the field boundary.

In the track finding program the effective edge motion is used as follows. The first step is to take all the hits in the first two wire chambers and generate all the in–going (to Janus) vectors. If the C magnet is turned off, the in–going vector is traced back to the target plane and the position is checked. The next step is to take all the hits in the last two wire chambers and generate all the out–going (from Janus) vectors. Then a simple geometric check is made to see if a circle (in the plan view) can be made in the Janus magnet using the vectors.

The effective edge approximation requires that the circle (in the full field region) be tangent to the in–going and out–going vectors at the point the vectors intersect the effective edges of the magnet. Recall that for any point on a circle, the line from the center of the circle to a point on the circle is perpendicular to the tangent at that point.

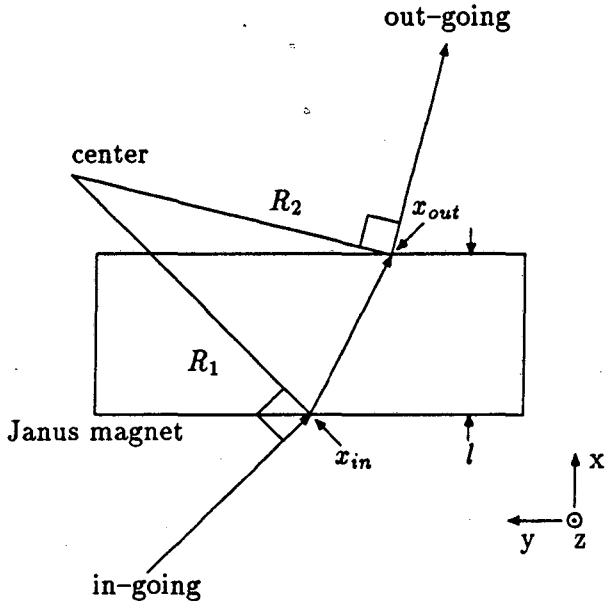

Figure 5.3: The Janus magnet with the set up for the Δr calculation.

The set up is shown in Fig. 5.3, the points x_{in} and x_{out} are the intersection of the in–going and out–going vectors with the effective edges. The lines R_1 and R_2 are perpendicular to the in–going and out–going vectors at x_{in} and x_{out}. If the two vectors are

from a good track, then the center of the circle is the intersection of R_1 and R_2. Then R_1 and R_2 are two radii of the circle that the path defines, and the fractional difference, $\Delta r = (R_1/R_2) - 1$, will be small. It is an easy exercise to calculate R_1 and R_2 from the length of the side of the triangle from x_{in} to x_{out}, the angle between R_1 and R_2, and the sine law. The choice of form for Δr was made to make the calculation insensitive to round–off errors. However, if both R_1 and R_2 are large, then the fractional error could be small, whereas the difference could be large. Therefore a cut is imposed so that R_1 and R_2 are not more than several times as large as the radius of the least curved track. The tracks at this point are ordered by Δr so that the "best" tracks are checked first.

Since two tracks are desired, all the steps that follow are done for both tracks.

First, the momentum[4] is calculated from deflection in the Janus magnet. One can easily show[5] that

$$p = \frac{q}{c} \frac{B_0 l}{|\sin\theta_{in} - \sin\theta_{out}|} \tag{5.12}$$

where l is the effective edge field length, θ is the angle between the particle's path and the normal to the field boundary (*in* for entering the full field region and *out* for leaving), B_0 is the field value at the center of the magnet, c is the speed of light, and q is the particle's charge.[6] The procedure adopted for calculating l was to calculate $\Delta \sin\theta$ for a sample of Monte Carlo tracks (made using the full field map). Then using the known momentum of the track, and the field (B_0), l is calculated. The momentum of the real tracks is then found from l, B_0 and the $\Delta \sin\theta$ of the track.

Once the momentum is known (Eq. 5.12) then the vertical motion can be calculated using Eq. 5.11. The motion can be easily expressed in matrix notation where the vector of interest is

$$\begin{pmatrix} z \\ \frac{dz}{ds} \end{pmatrix} . \tag{5.13}$$

Then motion from one point to another an arc length S apart in a constant field region

[4]The momentum calculated here is only used in the effective edge track finding. See Section 5.6 for the description of how the final momentum is found.

[5]See, for example, [1].

[6]This is the only location where q will be used for charge, elsewhere it is the difference in the momentum of the pions.

is just

$$\begin{pmatrix} z \\ \frac{dz}{ds} \end{pmatrix}_{out} = \begin{pmatrix} 1 & S \\ 0 & 1 \end{pmatrix} \begin{pmatrix} z \\ \frac{dz}{ds} \end{pmatrix}_{in}, \tag{5.14}$$

and the deflection at the field boundary is

$$\begin{pmatrix} z \\ \frac{dz}{ds} \end{pmatrix}_{out} = \begin{pmatrix} 1 & 0 \\ -\frac{1}{f} & 1 \end{pmatrix} \begin{pmatrix} z \\ \frac{dz}{ds} \end{pmatrix}_{in}, \tag{5.15}$$

where $\frac{1}{f} = \frac{\tan\theta}{r} z_0$ as in Eq. 5.11.

The motion from the first to the second wire chamber gives the initial $\frac{dz}{ds}$. Then the remainder of the motion can be found by applying Eq. 5.14 to move the particle from one location to the next, and applying Eq. 5.15 to move the particle across the field boundaries.

In the Janus magnet a further simplification is made; because the arc length (S) is hard to calculate it is desired to replace it with one of the coordinates, x. In the field free regions this change of variables is trivial, and the transfer matrix becomes

$$\begin{pmatrix} 1 & S \left.\frac{dx}{ds}\right|_{in} \\ 0 & \left(\left.\frac{dx}{ds}\right|_{out}\right)^{-1} \left.\frac{dx}{ds}\right|_{in} \end{pmatrix} \tag{5.16}$$

and in the field free regions $\frac{dx}{ds}$ is constant. All the need be done is to replace S by X, the change in x, to recover the original form of the transfer matrices.

In the full field regions $\left.\frac{dx}{ds}\right|_{out}$ is not necessarily equal to $\left.\frac{dx}{ds}\right|_{in}$ and is certainly not constant. However, to the accuracy of the other approximations made in the derivation, this is assumed to be true, and the full field regions are calculated in the same fashion as the field free regions. In the Janus magnet the tracks never make an angle of more than $\sim 45^0$ with the x axis and generally less, so $\frac{dx}{ds}$ varies around its maximum value of 1. In the C magnet, the tracks are handled differently, as will be described below.

In a similar calculation, the deflection matrix becomes

$$\begin{pmatrix} 1 & 0 \\ \left(\left.\frac{dx}{ds}\right|_{out}\right)^{-1} \left(-\frac{1}{f}\right) & \left(\left.\frac{dx}{ds}\right|_{out}\right)^{-1} \left.\frac{dx}{ds}\right|_{in} \end{pmatrix}. \tag{5.17}$$

Again, to the accuracy of the other approximations made in the derivation, we assume that $\frac{dx}{ds}$ is approximately 1 and the deflection matrix is unchanged.

With these approximations, the transfer matrices and the deflection matrices do not depend on the path length and are easy to calculate. Using the appropriate transfer matrix from the second effective edge to the third or fourth wire chamber, the height of the track can be predicted in the third and fourth chambers. A cut is made requiring that the hits used be close to the predicted height.[7] At this point the track finding in the Janus magnet is complete and there is a good chance that the track found is a real one. Therefore, the emphasis in the routines shifts from fast computing times to accuracy.

Next, the track from chamber three to chamber four is extended as a straight line to the AB array and the counters that the track struck are recorded. Tracks that miss the array are, of course, rejected.

If the C magnet is on, then the target traceback is done here. This is done to the full accuracy of the effective edge approximation because the tracks start out parallel to the beam line and the approximation used in the Janus magnet fails. The track is projected from the second chamber to the first chamber, and then to the effective edge of the C magnet. The radius of the track in the C magnet is computed from the Lorentz force law, and the new components of the velocity vector are computed from Eq. 5.11. The track then follows a spiral path back to the plane of the target. The length of the spiral is computed, and then the position at the target plane. A cut is made requiring that the initial position of the track be near the beam spot.

The tracks are then checked to see that the second track does not share wires with the first. Recall that, although triangles cannot share wires with anything else, crosses were allowed to share wires with other crosses. So at this level, a cut is imposed so that crosses are allowed to share wires in the two tracks only if all other hits in the pair of tracks are triangles. This gives the distribution of hits closest to flat. If the second track passes this cut, the pair of tracks is considered to be a good event and the data are written to the output file for further processing.

The accuracy of the effective edge approximation has two aspects. The first is the efficiency for finding single tracks, and the second is the efficiency for finding the two tracks correctly. When calculating the correlation function using the event–mixing technique, the single track efficiencies cancel out (see Section 6.2) and need not be measured. However, a

[7] These cuts are called ΔZ_3 and ΔZ_4, respectively.

good efficiency is desired to allow the largest data sample possible. The major concern is that two track efficiency depends in a predictable way on the event geometry. The track finding in single track and double track events were studied using Monte Carlo data using the full field map (in both magnets) with simulated multiple scattering and energy loss (with Landau straggling). The Monte Carlo data were presented to the track finder with one track per event to check the single track case, and with two tracks per event to check the two track case. For the single track data, the results are given in Table 5.1. The coordinates used are: $\hat{z}$ is vertical, and $\hat{x}$ is horizontal, perpendicular to the beam. The quantities ΔZ_3 and ΔZ_4 are the differences between the predicted (based on the effective edge approximation) and the actual heights in the third and fourth wire chambers.

Quantity	RMS error
Target traceback x	1.0 cm
Target traceback z	1.0 cm
Δr	0.79 %
ΔZ_3	0.69 cm
ΔZ_4	1.0 cm
$\lvert\vec{P}\rvert$	3.4 MeV/c

Table 5.1: Effective edge parameters for one Monte Carlo track per event.

When two tracks are present in each event, the possibility for misidentifying the hits exists. Therefore the histograms of the parameters include not only the effective edge errors as given in Table 5.1, but also random matches. These histograms are given in Fig. 5.4, 5.5, and 5.6. It can be seen that the effective edge approximation allows accurate track reconstruction.

With the Monte Carlo data, the tracks output by the track finder can be compared with the input. There exist three possibilities for an event: First, the event can be found correctly. Second, the event can be missed altogether, because not enough tracks can be found. Third, the event can be returned with the tracks confused, that is, with some hits from each input track assigned to one output track. The histograms for each of these classes for the first wire chamber are presented in Fig. 5.7. The figure shows the fraction of the input data in each class as a function of the distance between the two hits in this

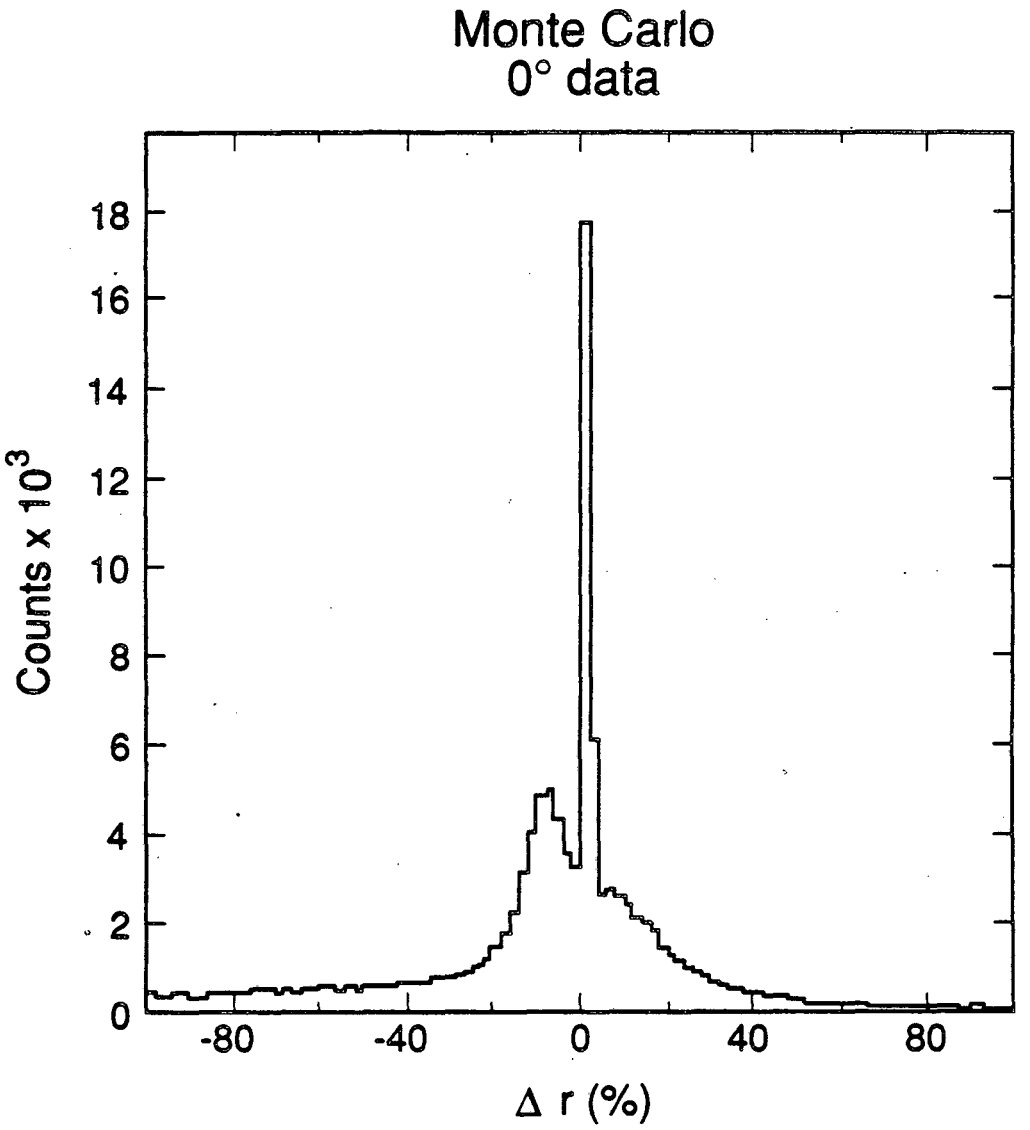

Figure 5.4: Δr with two tracks per event.

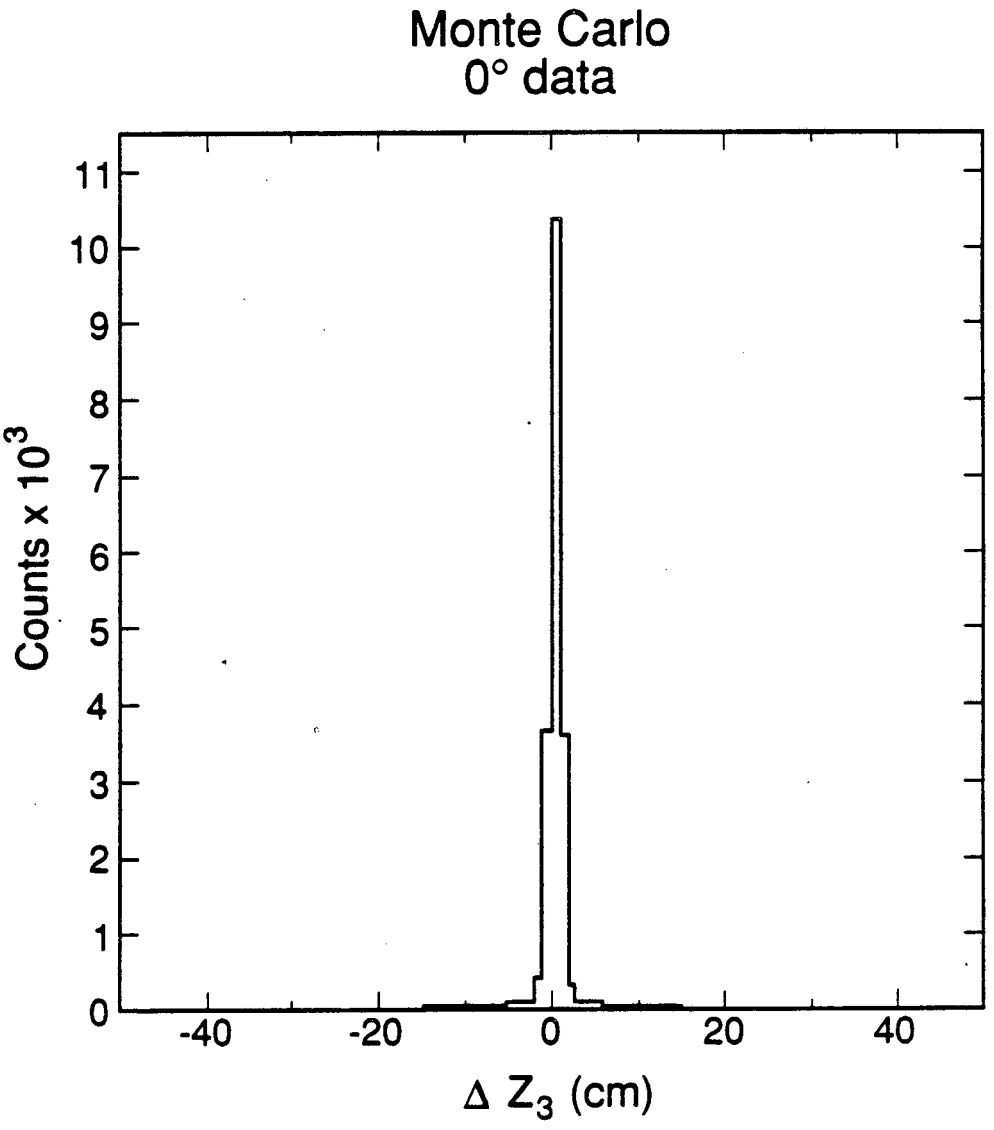

Figure 5.5: ΔZ_3 with two tracks per event.

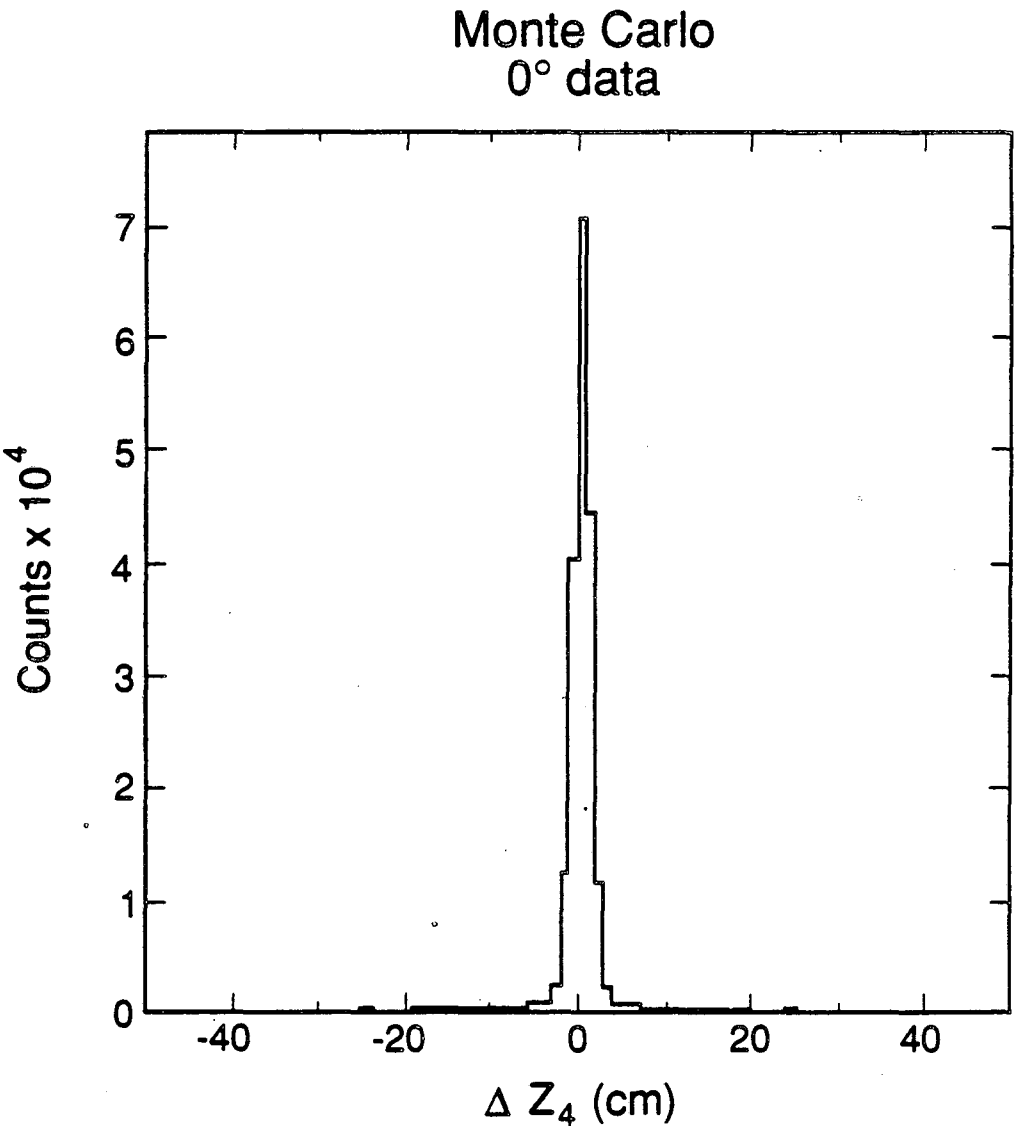

Figure 5.6: ΔZ_4 with two tracks per event.

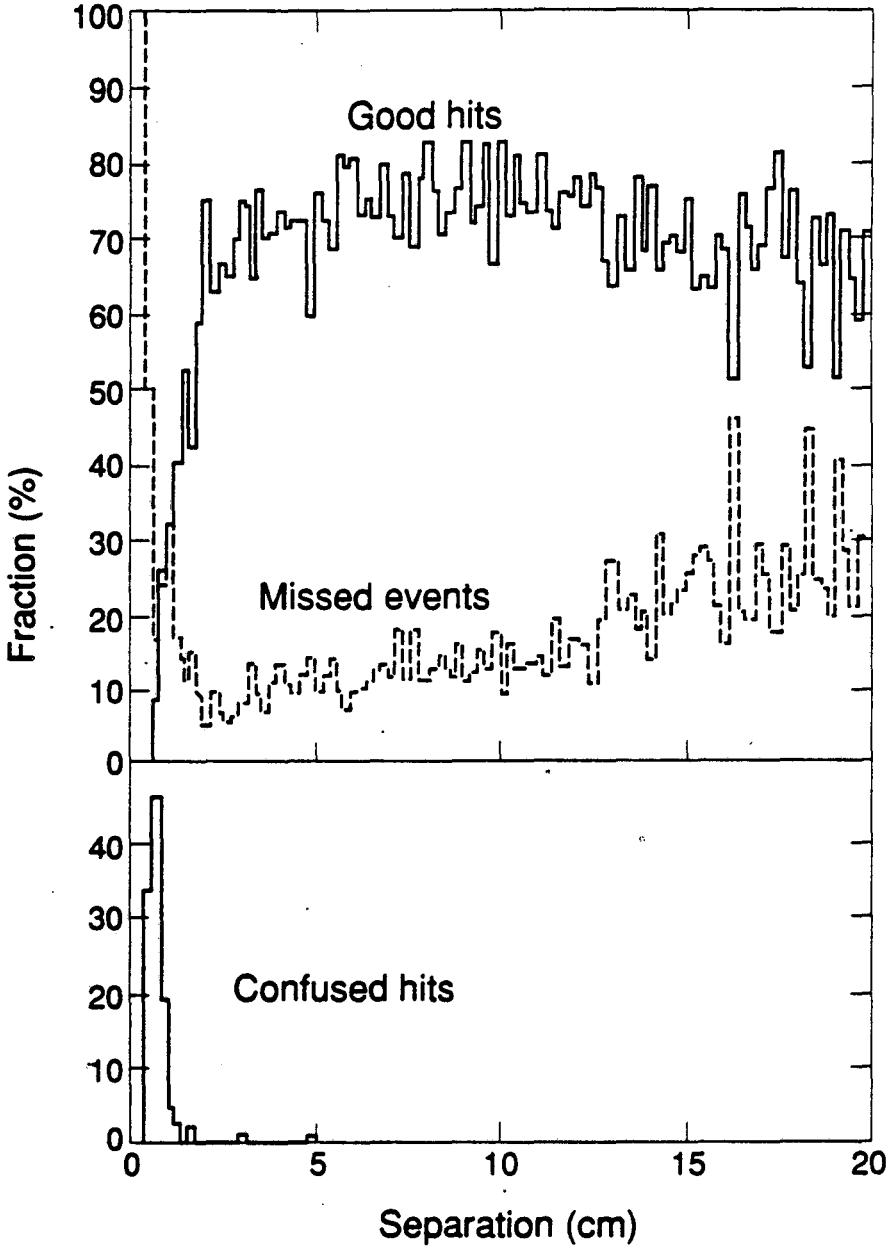

Figure 5.7: Track finding as a function of the hit separation in wire chamber one for Monte Carlo data.

wire chamber. The classes shown are: good hits — where the two tracks in the event were found correctly, missed events — where the two tracks in the event were not found, and confused hits — where the hits in this wire chamber were not found correctly (although two tracks were still found in the event). The histograms for the other wire chambers are similar, although the fraction of events with low separations is smaller for the other wire chambers since they are farther from the target. The feature to notice is that for separations of greater than 2 cm the fraction of confused hits is essentially zero, and the fraction of correctly found events is approximately constant. This is discussed further in the next section (Section 5.4).

At this point track finding is considered complete and the event information is written to tape to allow further processing. About 10% of the triggers survive the first level programs to be written to tape. Before discussing the further processing, the two track efficiency problems and their influence in the data analysis will be discussed.

5.4 Two Track Efficiency

The track–finding routines used introduce some two track efficiency effects. Correcting for them requires understanding how they are introduced in the real data, so that they can be simulated in the background data.

First, there is the hardware trigger requirement. Since the triggering requirement is that two independent AB pairs fire, events where both tracks strike the same AB pair will not fire the hardware trigger. Although it is possible that two AB pairs will fire for some reason when only a single one was struck by the two particles (for example, from a δ–ray striking a nearby counter), it is far more likely that a single pion event will cause this trigger than a two pion event, simply because of the large number of single pion events in the spectrometer. Therefore, a cut is made that requires that the two tracks trace to different AB pairs for the event to be accepted.

Second, the requirement that the triangles do not share wires means that the probability for detection of two hits that *do* share wires is reduced. This is because if a wire is missing from either of the two triangles, the remaining hit (call it the first hit) will form a triangle and the shared wire will be assigned to it, then the second hit will have only one wire passing though it and it is not possible to form a cross to recover the second

hit. Attempts to relax this requirement have always produced data where the number of tracks sharing wires is larger than one would expect for a random hit distribution. Rather than attempt to calculate the probability of missing hits in this fashion, which would depend on the plane efficiencies, a cut is made requiring that the two hits be such that, if all planes fired, the separation of the centroids of the clumps of fired wires in all planes is greater than or equal to 3.5 wires. The choice of 3.5 wires is determined by the requirement that there must be an unfired wire between two clumps of fired wires for the fired wires to be resolved as separate clumps of wires. Allowing one of the clumps to be two wires wide, this implies that the minimum distance between the centroids for the clumps to be resolved is 2.5 wires. Allowing for the wire chamber resolution of $\pm 1/2$ wire for each of the hits implies that the minimum separation between hits to guarantee that the clumps are resolved is 3.5 wires.

Third, the effective edge track reconstruction confuses hits in the tracks when the hits are separated by less than 2 cm. The track identification routine can eliminate these tracks, but the tracks are still lost. The CPU time required to use the methods of the track identification routine to recover these events would be prohibitive. Rather than try to calculate the efficiency for confusion, and subsequent removal, a cut is made requiring that the hits be separated by at least 2 cm in all chambers. Also, as pointed out in Section 5.3, if the hit separation is more than 2 cm the efficiency for reconstruction of Monte Carlo two track events is approximately constant (see Fig. 5.7).

These three cuts give a step-function two track efficiency — either the track is cut, or the two tracks are sufficiently well separated in all detectors that the track finding efficiency is constant. These cuts are imposed on the real data and the background data at the stage where the data were histogrammed and at any point where the two track efficiency function (ρ_{ij}) is used when calculating the event weights in the residual correlation removal (see Chapter 6). The Monte Carlo test of the correlation function fitting procedure (see Section 7.2) included these cuts.

5.5 Particle Identification

Particle identification in the two pion experiment was done at a simple level. If the spectrometer is set to accept negative particles then all detected particles are assumed

to be negative pions. The electron contamination was estimated by taking the number of π^0's produced to be equal to the number of π^-'s produced, taking all of the π^0's as decaying into 2γ's, which are assumed to continue at the momentum of the π^0 (this will overestimate the number of high energy electrons) and then the conversion probability for the γ's was calculated for the target and the air up to the first counters. The particle identification in the negative data is estimated to give an electron contamination of about 5% or less.

5.6 Momentum and Other Track Parameter Fitting

After the particles have been identified, a better track reconstruction is done.

First, any missing wires in the track are reconstructed using equations derived from Eq. 5.8. The tracks' parameters are then calculated as functions of the measured quantities, namely the wire numbers. The procedure used is to use a Monte Carlo simulation to generate a large number of tracks to give the wire numbers hit in the wire chambers as a function of the initial position of the particle and its vector momentum. Note that since there are twelve planes of wires and only five free parameters (two for the initial position at the target plane and three for the vector momentum) some of the wire chamber data are redundant. There is sufficient redundancy that the fourth wire chamber is removed from the input to the fits and later used to verify the effective–edge track reconstruction. The remaining wire chamber data (nine planes) are subject to a principle component analysis[43] to determine which linear combinations of the wire numbers show the most variation in the Monte Carlo data set and which show the least. The five linear combinations showing the most variation were considered to be the most significant to the fit of the parameters as a function the wire numbers, and the remaining four combinations redundant. Each of the desired parameters was then fit using orthogonal polynomials as a function of the five retained wire number combinations. In this experiment Chebyshev polynomials were used since they have good properties for interpolating data. The program used for this analysis was ERIKA written by Harald von Fellenberg and modified by Jim Miller and William Zajc to run on the computers used.

The input data for this procedure is a Monte Carlo simulation of the experiment. The Monte Carlo program is described in Appendix A. We used Monte Carlo data with

multiple scattering and Landau straggling to determine the momentum resolution of this procedure and the results are given in Table 5.2. The coordinate system used is: $-\hat{y}$ is along the beam line, $\hat{z}$ is vertical, and $\hat{x}$ is perpendicular to the beam. Note that $\vec{p}$ was calculated in the laboratory frame and $\mathbf{Q}$ was calculated in the center of mass (of the nuclei) frame.

Quantity	RMS error
p_x	3.6 MeV/c
p_y	2.2 MeV/c
p_z	3.4 MeV/c
q_x	5.1 MeV/c
q_y	1.7 MeV/c
q_z	4.8 MeV/c
q_0	1.8 MeV

Table 5.2: Resolution for Monte Carlo simulated events.

From the data of Table 5.2 the resolution in the components of $(\vec{q}, q_0)$ histogrammed is computed to be (using Δ to denote the uncertainty in a quantity) $\Delta q_0 = 2$ MeV, $\Delta q_{||} = 2$ MeV/c and $\Delta q_{\perp} = 7$ MeV/c. The momentum differences were histogrammed over a range of 0 – 250 MeV/c (or MeV for q_0) with a bin width of 10 MeV/c (or MeV).[8] The spectrometer's resolution is estimated to change the value of the correlation function in the bins of the histogram by $< 1\%$ (FWHM). The range of the parameters resolvable by the apparatus was estimated by requiring that the correlation function vary by $e^{-1/2}$ over the full range of the histograms, and from the first bin to the second bin. The range over which $R_{\perp}$, $R_{||}$ and $c\tau$ are resolvable is from ~ 1 to ~ 20 fm.

In addition to the momentum, other track parameters were fit using the principle component analysis. The parameters are: the target traceback, the distance to the lead walls in the C magnet, and the position of the hit in the fourth wire chamber. One can derive from the individual target tracebacks the separation between the two tracks at the target (which should be zero if the two tracks come from the same nuclear collision). These quantities were compared to the expected values to verify that the track was reconstructed

[8] These values imply that the histograms have 25 bins on each side.

correctly. These cuts were typically placed at three times the corresponding RMS error as calculated from the Monte Carlo tracks.

Chapter 6

Background Generation and Function fitting

6.1 Background Event Generation

The word "background" is used here to mean a two pion data sample with all the physics incorporated except for the Bose–Einstein symmetrization. The measured correlation function is then the ratio of the real data to the background data. It is vital that the single and two track efficiencies be incorporated correctly so that when the ratio of the real data and the background data is taken the efficiencies will cancel.

In this experiment the method of event mixing was used to generate the background data sample. Event mixing consists of taking one pion from an event, adding to it one pion from a different, randomly chosen, event and calling this a two pion event, which is then used to form the background. This assumes that the momentum distribution of a pion in the two pion event is not influenced by the other pion in the event (the ignored pion). Since the pions are correlated (measurement of this correlation is the subject of this thesis), this is only approximately true. The background events are corrected for the correlation by weighting the pions that are mixed to form the event. To show how this weighting is done and, how the background events are generated, it is necessary to consider in detail how the correlation function is calculated from the two pion data. This requires the calculation of the "residual correlation" for the background histogram bins.

The residual correlation calculation is then cast as an event weighting calculation, and the momentum binning assumed no longer appears.

Once the background events have been generated, the correlation function is fit to the measured and the background data samples. The Principle of Maximum Likelihood was used when fitting the data, to avoid biasing the data when the number of counts per bin is small and Poisson statistics must be used. Two different measures of the quality of the fit are given, that of a restricted χ^2, and that of a generalized χ^2, denoted $\chi^2_{\rm PML}$, which is derived from the Principle of Maximum Likelihood and is based on the log of the likelihood function.

6.2 Derivation of Event Mixing

This section uses notation based on the notation used in [1]:

Let η_i be the one particle detection efficiency.

η_{ij} be the two particle detection efficiency.

ω_i be the number density of emitted particles.[1]

C_{ij} be the Bose–Einstein correlation function.

ρ_{ij} be the two particle contribution to the detection efficiency, defined such that $\eta_{ij} = \eta_i \eta_j \rho_{ij}$.

In the above i, j represent momentum bins; That is $i \rightarrow \vec{p}_i$ and $j \rightarrow \vec{p}_j$ and so on. Note that [1] assumed that $\eta_{ij} = \eta_i \eta_j$, or $\rho_{ij} \equiv 1$. Although only one dimension of the histograms will be shown explicitly, it is simple to extend to arbitrary numbers of dimensions by adding subscripts.[2] The correlation function, C_{ij}, will not be taken to be an explicit function of $\vec{q}$. Since $\vec{q} = \vec{p}_1 - \vec{p}_2$, one can regard $C(\vec{q})$ as $C(\vec{q}(\vec{p}_1, \vec{p}_2)) = C_{ij}$ without loss of generality.

The letters $i, j, k, \ldots$ will be used for sums over momentum bins and $\alpha, \beta, \gamma, \ldots$ for sums over events. The calligraphic letter $\mathcal{P}$ will be used for probability. In the two pion

[1] Note the technique of event mixing assumes that a single number density of emitted particles, ω_i, describes all the events. Section 3.5 discusses some of the consequences of this assumption. See also [37] for a discussion of this and related points.

[2] One can also number all the bins sequentially in some fashion and use the equations derived here.

events there are two momenta, so $\vec{p}_{\alpha 1}$ will be used for the α^{th} event's first pion momentum and $\vec{p}_{\beta 2}$ for the β^{th} event's second pion momentum.

With this notation, the two pion experiment consists of measuring a set of N two pion events, which can be written

$$\{(\vec{p}_{\alpha 1}, \vec{p}_{\alpha 2})\}_{\alpha=1}^{N} \text{ , where } N = \text{ the number of events.}$$

Central to the analysis is making a histogram, so the definition of a function that corresponds to making a histogram is needed. Therefore, define a δ function by

$$\delta(\vec{p} \in i) = \begin{cases} 1 \text{ for } \vec{p} \in i\text{th momentum bin} \\ 0 \text{ for } \vec{p} \notin i\text{th momentum bin} \end{cases} \tag{6.1}$$

then making a histogram of the momentum distribution for the first pion in the events corresponds to finding the n_i that are the number of counts per bin by

$$n_i = \sum_{\alpha=1}^{N} \delta(\vec{p}_{\alpha 1} \in i) \, .$$

Before starting into the details of the calculations, it is best to reveal the plan of attack. What is wanted is, of course, the C_{ij} in terms of known quantities. The known quantities in this experiment are the momentum distributions of the pions, the $\delta(\vec{p}_{\alpha 1} \in i)$, for the data set of two pion events. The functions η_i, ω_i and ρ_{ij} are unknown (or, in the case of ρ_{ij}, known approximately). Therefore, the calculation will express the η_i, ω_i and C_{ij} in terms of the momentum distributions and other known quantities. This requires that some normalizations be assumed for the probabilities and for the momentum distributions. In many cases the value assumed for the normalization is unimportant, so long as a normalization is assumed.

Assume the following normalizations

$$\sum_{i=1}^{M} \omega_i = 1 \text{ , Probability of emission somewhere = 1, and} \tag{6.2}$$

$$\sum_{i} \eta_i \omega_i = \Omega \text{ , The efficiency of the spectrometer.} \tag{6.3}$$

Since Ω is unknown, this can be used to define Ω. Also, the normalization of ω_i implies that $\omega_i \sim \mathcal{O}(\frac{1}{M})$, where M = the number of bins.

The normalization for the real two track probability with detector problems, $\mathcal{P}_2^R$ (the superscript R is intended to denote a "real" momentum distribution, as opposed to the "fake" momentum distributions that will be considered later on), is found by considering the definition of $\mathcal{P}_2^R$,

$$\begin{aligned}\mathcal{P}_2^R(i,j) &\equiv \text{the real probability of a two track event with } \vec{p}_1 \in i\text{th bin}, \vec{p}_2 \in j\text{th bin} \\ &= \eta_i\omega_i\eta_j\omega_j C_{ij}\rho_{ij} \ . \end{aligned} \tag{6.4}$$

It is clear that,

$$\mathcal{P}_2^R(i,j) \propto \sum_\alpha \delta(p_{\alpha 1} \in i)\delta(p_{\alpha 2} \in j) \ . \tag{6.5}$$

To find the constant of proportionality use

$$\sum_{ij}\sum_\alpha \delta(\vec{p}_{\alpha 1} \in i)\delta(\vec{p}_{\alpha 2} \in j) = N \ . \tag{6.6}$$

Note that if $C_{ij}\rho_{ij} = 1 \ \forall \ i,j$, then[3]

$$\begin{aligned}\sum_{ij}\mathcal{P}_2^R(i,j) &= \sum_{ij}\eta_i\omega_i\eta_j\omega_j C_{ij}\rho_{ij} \\ &= \Omega^2 \ , \end{aligned} \tag{6.7}$$

so define A such that

$$\begin{aligned}\sum_{ij}\mathcal{P}_2^R(i,j) &= \sum_{ij}\eta_i\omega_i\eta_j\omega_j C_{ij}\rho_{ij} \\ &= \Omega^2 A \ . \end{aligned} \tag{6.8}$$

Then, using

$$\frac{\Omega^2 A}{N}\sum_{ij}\sum_\alpha \delta(\vec{p}_{\alpha 1} \in i)\delta(\vec{p}_{\alpha 2} \in j) = \Omega^2 A \tag{6.9}$$

the normalization desired can be seen to be

$$\mathcal{P}_2^R(i,j) = \frac{\Omega^2 A}{N}\sum_\alpha \delta(\vec{p}_{\alpha 1} \in i)\delta(\vec{p}_{\alpha 2} \in j) \ . \tag{6.10}$$

The above definition can be seen to be equivalent to

$$A = \frac{\sum_{ij} C_{ij}\rho_{ij}\eta_i\omega_i\eta_j\omega_j}{\sum_i \eta_i\omega_i \sum_j \eta_j\omega_j} \tag{6.11}$$

$$= \frac{\text{The number of detected two track events}}{\text{The number of two track events detected, if seen one track at a time}} \tag{6.12}$$

[3]The symbol "$\forall$" is used to denote the phrase "for all".

Note that A is unknown unless the C_{ij} and ρ_{ij} are known.

Now, to find the correlation function, use the definitions (Eqs. 6.4, and 6.10) of $\mathcal{P}_2^R$, to get

$$\eta_i\omega_i\eta_j\omega_j C_{ij}\rho_{ij} = \frac{\Omega^2 A}{N}\sum_\alpha \delta(\vec{p}_{\alpha 1} \in i)\delta(\vec{p}_{\alpha 2} \in j) \tag{6.13}$$

thus

$$C_{ij} = \frac{\frac{\Omega^2 A}{N}\sum_\alpha \delta(\vec{p}_{\alpha 1} \in i)\delta(\vec{p}_{\alpha 2} \in j)}{\eta_i\omega_i\eta_j\omega_j\rho_{ij}} \ . \tag{6.14}$$

At this point the task of calculating the correlation function, C_{ij}, is half complete. The correlation function has been expressed in terms of the two particle momentum distribution, the η_i, the ω_i and ρ_{ij}. It will turn out to be impossible to eliminate ρ_{ij} — the two particle contribution to the detection efficiency — it will be approximated by the cuts outlined in Chapter 5. These cuts will be applied to the real data (to give an explicit form for ρ_{ij}) and whenever ρ_{ij} appears in a formula.

Now to continue the calculation of the correlation function, the $\eta_i\omega_i$ are needed. The $\eta_i\omega_i$ are just the real single track probability of detection (which will be denoted $\mathcal{P}_1^R$). It is expected that, since the correlation is not strong, the two pions in the event will behave approximately independently. So the single pion detection probability can be approximated by just ignoring one of the two pions in the two pion event. So define $\mathcal{P}_1^F$ to be the "fake" one track probability, that is, the probability of detection for one track without regard to the second track of the pair in the event.[4] Roughly,

$$\mathcal{P}_1^F(i) = \frac{1}{N}\sum_\alpha \delta(\vec{p}_{\alpha 1} \in i) \ , \text{ where } \vec{p}_{\alpha 2} \text{ is ignored.}$$

The normalization for $\mathcal{P}_1^F$ is given by considering

$$\mathcal{P}_1^F(i) \propto \eta_i\omega_i\sum_m \eta_m\omega_m C_{im}\rho_{im} \ , \tag{6.15}$$

where the sum is just the probability of observing the first pion's at momentum i, summed over all possible values for the second pion's momentum. If $C_{im}\rho_{im} = 1 \ \forall \ i, m$, then

$$\eta_i\omega_i\sum_m \eta_m\omega_m C_{im}\rho_{im} = \eta_i\omega_i\Omega \ . \tag{6.16}$$

[4]The first track will be used to generate the background. This is not essential since the assignment of the tracks should be random. The computer codes pick the tracks randomly from the first and second tracks in the events to avoid biases in the track-finding programs.

Whereas, if there are no two pion effects, so $C_{ij}\rho_{ij} = 1 \; \forall \; i,j$, then $\mathcal{P}_1^F(i) = \eta_i\omega_i = \mathcal{P}_1^R(i)$ (that appears in the denominator of Eq. 6.14 above). Therefore, a convenient normalization is

$$\mathcal{P}_1^F(i) = \eta_i\omega_i\frac{1}{\Omega}\sum_m \eta_m\omega_m C_{im}\rho_{im} \; . \tag{6.17}$$

Now, write

$$\mathcal{P}_1^F(i) = \sum_m \frac{1}{\Omega}\eta_i\omega_i\eta_m\omega_m C_{im}\rho_{im} \tag{6.18}$$

and use Eq. 6.13 for $\eta_i\omega_i\eta_m\omega_m C_{im}\rho_{im}$. Then

$$\mathcal{P}_1^F(i) = \frac{\Omega A}{N}\sum_m\sum_\alpha \delta(\vec{p}_{\alpha 1} \in i)\delta(\vec{p}_{\alpha 2} \in m) \; . \tag{6.19}$$

Interchange the m, α sums and use

$$\sum_m \delta(\vec{p}_{\alpha 2} \in m) = 1 \text{ , since } \vec{p}_{\alpha 2} \text{ must be somewhere,} \tag{6.20}$$

then the normalization for $P_1^F(i)$ is given by

$$\mathcal{P}_1^F(i) = \frac{\Omega A}{N}\sum_\alpha \delta(\vec{p}_{\alpha 1} \in i) \; . \tag{6.21}$$

Use both expressions for $\mathcal{P}_1^F(i)$ (Eqs. 6.17, and 6.21) to get

$$\frac{\Omega A}{N}\sum_\alpha \delta(\vec{p}_{\alpha 1} \in i) = \eta_i\omega_i\frac{1}{\Omega}\sum_m \eta_m\omega_m C_{im}\rho_{im} \tag{6.22}$$

and so,

$$\eta_i\omega_i = \frac{\frac{\Omega A}{N}\sum_\alpha \delta(\vec{p}_{\alpha 1} \in i)}{\frac{1}{\Omega}\sum_m \eta_m\omega_m C_{im}\rho_{im}} \tag{6.23}$$

and the $\eta_i\omega_i$ have been expressed in terms of a momentum distribution and a weighting factor.

This is a formal solution to finding the correlation function in that Eq. 6.23 gives us the $\eta_i\omega_i$ and Eq. 6.14 gives us C_{ij} in terms of the $\eta_i\omega_i$ and known (or measurable) quantities.

To examine the role of the weighting factor more carefully, set

$$W_i = \frac{1}{\frac{1}{\Omega}\sum_m \eta_m\omega_m C_{im}\rho_{im}} \tag{6.24}$$

then combining Eqs. 6.14 and 6.23 gives

$$C_{ij} = \frac{\frac{\Omega^2 A}{N}\sum_\alpha \delta(\vec{p}_{\alpha 1} \in i)\delta(\vec{p}_{\alpha 2} \in j)}{(\frac{\Omega A}{N})^2 W_i W_j \rho_{ij}\sum_\beta\sum_\gamma \delta(\vec{p}_{\beta 1} \in i)\delta(\vec{p}_{\gamma 1} \in j)} \tag{6.25}$$

and it is apparent that C_{ij} is the ratio of the real data to a background data sample that is made by combining pions from different events. Another important feature is the fact that the $\eta_i\omega_i$ do not appear in the calculation of C_{ij}. The $\eta_i\omega_i$ in the numerator cancel those in the denominator and, as a result, measuring the spectrometer's single track efficiency is unnecessary. This is an extension of Eq. 3.15 in that the two track efficiency is included in the denominator.

The origin of the weighting factor is this: even though only one pion is used, there was another pion detected in the event. If there were no correlation between the pions then the probability distribution for the ignored pion would be $\eta_m\omega_m$ (if m is its momentum bin), and the ignored pion would just weight, on average, the kept pion by $\sum_m \eta_m\omega_m$, a constant. But the pions are correlated so the probability distribution for the ignored pion, given that the kept pion has momentum i, is $\eta_m\omega_m C_{im}\rho_{im}$ (which, when summed over the momentum bins, gives a weight of $\sum_m \eta_m\omega_m C_{im}\rho_{im}$) and the kept pion, through the correlation function, modifies the probability distribution of the ignored pion. If the modified probability distribution happens to increase the probability of the ignored pion being in regions where the detection efficiency is high, then the probability of detecting the kept pion is increased (relative to the case where there is no correlation). The combination of the probability of emission (η_m), the probability of detection (ω_m), the two particle contribution to the detector efficiency (ρ_{im}), and the correlation function (C_{im}) all contribute to the weighting factor.

6.3 Residual Correlations

Define "residual correlation" to be the ratio between the fake single track probability and the real single track probability, that is $\mathcal{P}_1^F/\mathcal{P}_1^R$. This is just the reciprocal of the weight defined in Eq. 6.24. From Eq. 6.17 this can be seen to be

$$\frac{\mathcal{P}_1^F(i)}{\mathcal{P}_1^R(i)} = \frac{1}{\Omega}\sum_m \eta_m\omega_m C_{im}\rho_{im} \ . \tag{6.26}$$

For an ideal spectrometer, $\eta_m = 1\,\forall\, m$, and $\rho_{im} = 1\,\forall\, i,m$, then

$$\frac{\mathcal{P}_1^F(i)}{\mathcal{P}_1^R(i)} = \frac{1}{\Omega}\sum_m \omega_m C_{im} \ , \tag{6.27}$$

which is not necessarily equal to one. In principle, it should be necessary to correct for residual correlations for perfect spectrometers, since the emission probability can induce a residual correlation. For a 4π spectrometer with (only) two track resolution problems, $\rho_{im} \not\equiv 1$, and

$$\frac{\mathcal{P}_1^F(i)}{\mathcal{P}_1^R(i)} = \frac{1}{\Omega}\sum_m \omega_m C_{im}\rho_{im} \ . \tag{6.28}$$

So residual correlations could be important.

6.4 Iteration Scheme for the Event Weights

To calculate the correlation function, a practical way to calculate the $\eta_i\omega_i$ is needed, so expand Eq. 6.23 in a small parameter. It will prove to be possible to derive a successive approximation scheme in powers of a suitably chosen small parameter. The expansion used here is motivated by noting that the correlation between pions is not expected to be strong. This implies that the effect of the ignored pion will not be large, or

$$\mathcal{P}_1^R(i) \approx \mathcal{P}_1^F(i)$$

which is equivalent to

$$\eta_i\omega_i \approx \frac{\Omega A}{N}\sum_\alpha \delta(\vec{p}_{\alpha 1} \in i)$$

which is equivalent to, from Eq. 6.23,

$$\frac{1}{\Omega}\sum_m \eta_m\omega_m C_{im}\rho_{im} \approx 1 \ .$$

So, write

$$\frac{1}{\Omega}\sum_m \eta_m\omega_m C_{im}\rho_{im} = 1 + \frac{\delta_i}{\Omega} \ .$$

Since $\Omega \leq 1$, δ_i is still a small number then, using $\frac{1}{\Omega}\sum_m \eta_m\omega_m = 1$,

$$\frac{1}{\Omega}\sum_m \eta_m\omega_m C_{im}\rho_{im} = \frac{1}{\Omega}\left(\sum_m \eta_m\omega_m + \delta_i\right) \ . \tag{6.29}$$

Define δ_{im} such that

$$\frac{1}{\Omega}\sum_m \eta_m\omega_m C_{im}\rho_{im} = \frac{1}{\Omega}\sum_m \eta_m\omega_m(1+\delta_{im}) \ , \tag{6.30}$$

a suitable such δ_{im} is $\delta_{im} = C_{im}\rho_{im} - 1$. If this is used, then $\delta_i = \sum_m \eta_m\omega_m\delta_{im}$ (from Eq. 6.29 and 6.30) and, on the average, δ_{im} is small.

With this as motivation, take $\delta_{im} = C_{im}\rho_{im} - 1$ and expand Eq. 6.22 in powers of δ_{im}.[5] Recall Eq. 6.22:

$$\frac{\Omega A}{N}\sum_{\alpha}\delta(\vec{p}_{\alpha 1} \in i) = \frac{\eta_i\omega_i}{\Omega}\sum_{m}\eta_m\omega_m C_{im}\rho_{im} \ .$$

Use $C_{im}\rho_{im} = 1 + \delta_{im}$ and $\frac{1}{\Omega}\sum_m \eta_m\omega_m = 1$, then

$$\frac{\Omega A}{N}\sum_{\alpha}\delta(\vec{p}_{\alpha 1} \in i) = \eta_i\omega_i \ \left(1 + \frac{1}{\Omega}\sum_{m}\eta_m\omega_m\delta_{im}\right) \tag{6.31}$$

and

$$\eta_i\omega_i = \frac{\frac{\Omega A}{N}\sum_\alpha \delta(\vec{p}_{\alpha 1} \in i)}{1 + \frac{1}{\Omega}\sum_m \eta_m\omega_m\delta_{im}} \ . \tag{6.32}$$

So far there have been no approximations. Note that $\eta_m\omega_m$ appears as $\sum_m \eta_m\omega_m\delta_{im}$, so $\eta_m\omega_m$ can be accurate to the $(n-1)^{\text{th}}$ order in δ_{im}, but the equation will still be n^{th} order in δ_{im}. This suggests the following approximation scheme be used

$$(\eta_i\omega_i)^{0\text{th}} = \frac{\Omega A}{N}\sum_{\alpha}\delta(\vec{p}_{\alpha 1} \in i) \tag{6.33}$$

$$(\eta_i\omega_i)^{n\text{th}} = \frac{\frac{\Omega A}{N}\sum_\alpha \delta(\vec{p}_{\alpha 1} \in i)}{1 + \frac{1}{\Omega}\sum_m (\eta_m\omega_m)^{(n-1)\text{th}}\delta_{im}} \ . \tag{6.34}$$

Note that Eq. 6.33 results from assuming that $\delta_{im} \equiv 0$. The problems with this idea are that (1) A is unknown, and (2) δ_{im} will be hard to calculate. However, having found the approximation scheme, the δ_{im} can be eliminated and a condition to give A can be found.

First, the condition to give A will be found. Note that $\frac{1}{\Omega}\sum_i \eta_i\omega_i = 1$. Calculate this sum using the 0^{th} order equation (Eq. 6.33), to get

$$\sum_i \eta_i\omega_i = \frac{\Omega A}{N}\sum_i\sum_\alpha \delta(\vec{p}_{\alpha 1} \in i) \tag{6.35}$$

$$\Omega = \frac{\Omega A}{N}\cdot N \tag{6.36}$$

and $A = 1$ to 0^{th} order of δ_{im}. Hence

$$(\eta_i\omega_i)^{0\text{th}} = \frac{\Omega}{N}\sum_{\alpha}\delta(\vec{p}_{\alpha 1} \in i) \tag{6.37}$$

and at each step one can fix A by the requirement that $\sum_i \eta_i\omega_i = \Omega$.

[5] Note that the small parameter, δ_{im}, is not directly related to the histogram making function, $\delta(\vec{p}_{\alpha 1} \in i)$.

The δ_{im} can then be eliminated through use of the definition $\delta_{im} = C_{im}\rho_{im} - 1$ and noting that $\frac{1}{\Omega}\sum_m \eta_m\omega_m = 1$. With these, the iteration scheme for calculating the $\eta_i\omega_i$ becomes

$$(\eta_i\omega_i)^{0\text{th}} = \frac{\Omega}{N}\sum_\alpha \delta(\vec{p}_{\alpha 1} \in i) \tag{6.38}$$

$$(\eta_i\omega_i)^{n\text{th}} = A\frac{\frac{\Omega}{N}\sum_\alpha \delta(\vec{p}_{\alpha 1} \in i)}{\frac{1}{\Omega}\sum_m (\eta_m\omega_m)^{(n-1)\text{th}} C_{im}\rho_{im}} \tag{6.39}$$

where in Eq. 6.39, A is chosen so that $\sum_i (\eta_i\omega_i)^{n\text{th}} = \Omega$.

Now the iteration scheme for the bin weights is converted into something easier to calculate on an event by event basis. This is desirable since it is easier to deal with event weights because the histogram binning does not appear in the calculation of the event weights. The bin weighting scheme is recast into an event weighting scheme by using the fact that for small momentum bins (and continuous functions F)

$$\sum_\alpha \delta(\vec{p}_{\alpha 1} \in i)F(\vec{p}_i) = \sum_\alpha \delta(\vec{p}_{\alpha 1} \in i)F(\vec{p}_{\alpha 1}) \tag{6.40}$$

where the difference is that F is evaluated at the center of the momentum bin in the first case, and at the momentum of the pion in the event in the second case. Note that if histogramming is to have any merit in this analysis, the momentum bins must be small enough so that this is true. The $\eta_\alpha\omega_\alpha$ (the event probabilities for detection and emission) will be defined so that

$$\sum_\alpha \eta_\alpha\omega_\alpha\delta(\vec{p}_{\alpha 1} \in i) = \eta_i\omega_i \tag{6.41}$$

then the correlation function, Eq. 6.14, becomes

$$C_{ij} = \frac{\frac{\Omega^2 A}{N}\sum_\alpha \delta(\vec{p}_{\alpha 1} \in i)\delta(\vec{p}_{\alpha 2} \in j)}{\sum_\beta \delta(\vec{p}_{\beta 1} \in i)\eta_\beta\omega_\beta \sum_\gamma \delta(\vec{p}_{\gamma 1} \in j)\eta_\gamma\omega_\gamma\rho_{\beta\gamma}}\,. \tag{6.42}$$

A suitable set of such probabilities can be seen to be

$$(\eta_\alpha\omega_\alpha)^{0\text{th}} = \frac{\Omega}{N} \tag{6.43}$$

$$(\eta_\alpha\omega_\alpha)^{n\text{th}} = A\frac{\frac{\Omega}{N}}{\frac{1}{\Omega}\sum_m \sum_\beta \delta(\vec{p}_{\beta 1} \in m)(\eta_\beta\omega_\beta)^{(n-1)\text{th}} C_{\alpha m}\rho_{\alpha m}} \tag{6.44}$$

since the addition of the sum over events and the δ functions in Eq. 6.42, and the removal of the same from 6.43, and 6.44, reproduces Eqs. 6.14, 6.38 and 6.39 (using Eq. 6.40, and

using Eq. 6.41 to change from $\eta_\beta\omega_\beta$ to $\eta_m\omega_m$ in Eqs. 6.42, 6.44). Interchanging the m and β sums and using Eq. 6.40 gives

$$(\eta_\alpha\omega_\alpha)^{0\text{th}} = \frac{\Omega}{N} \tag{6.45}$$

$$(\eta_\alpha\omega_\alpha)^{n\text{th}} = A\frac{\frac{\Omega}{N}}{\frac{1}{\Omega}\sum_\beta(\eta_\beta\omega_\beta)^{(n-1)\text{th}}C_{\alpha\beta}\rho_{\alpha\beta}} . \tag{6.46}$$

The normalization condition for A in Eq. 6.46, is found from Eq. 6.41 and using Eq. 6.20, with these

$$\begin{aligned}\Omega &= \sum_i(\eta_i\omega_i)^{n\text{th}} \\ &= \sum_i\sum_\beta \delta(\vec{p}_{\beta 1}\in i)\,(\eta_\beta\omega_\beta)^{n\text{th}} \\ &= \sum_\beta(\eta_\beta\omega_\beta)^{n\text{th}} .\end{aligned} \tag{6.47}$$

Finally, to get the event weights and eliminate the normalization of the $\eta_\alpha\omega_\alpha$, set $W(\alpha) = \frac{\eta_\alpha\omega_\alpha N}{\Omega}$. Then Eq. 6.42 becomes

$$\begin{aligned}C_{ij} &= \frac{\frac{\Omega^2 A}{N}\sum_\alpha \delta(\vec{p}_{\alpha 1}\in i)\delta(\vec{p}_{\alpha 2}\in j)}{\frac{\Omega}{N}\sum_\beta W(\beta)\delta(\vec{p}_{\beta 1}\in i)\frac{\Omega}{N}\sum_\gamma W(\gamma)\delta(\vec{p}_{\gamma 1}\in j)\rho_{\beta\gamma}} \\ &= \frac{AN\sum_\alpha \delta(\vec{p}_{\alpha 1}\in i)\delta(\vec{p}_{\alpha 2}\in j)}{\sum_\beta W(\beta)\delta(\vec{p}_{\beta 1}\in i)\sum_\gamma W(\gamma)\delta(\vec{p}_{\gamma 1}\in j)\rho_{\beta\gamma}}\end{aligned} \tag{6.48}$$

and the iteration scheme becomes

$$(W(\alpha))^{0\text{th}} = 1 \tag{6.49}$$

$$(W(\alpha))^{n\text{th}} = A\frac{1}{\frac{1}{N}\sum_\beta(W(\beta))^{(n-1)\text{th}}C_{\alpha\beta}\rho_{\alpha\beta}} \tag{6.50}$$

where, in Eq. 6.50, the normalization condition is that A is chosen such that

$$\sum_\beta(W(\beta))^{n\text{th}} = N \tag{6.51}$$

or the average weight is one.

At this point the task is complete, C_{ij} has been expressed in terms of momentum distributions (and some constants) with event weights, and the event weights are expressed as a successive approximation scheme involving the correlation function and the two particle contribution to the spectrometer's efficiency. All that remains is to describe how

the correlation function is fit, and how to convert these equations to the ones used in the computer codes.

In the actual computer codes, the normalization of C_{ij} is fit. Therefore, in Eq. 6.48, AN is only estimated by setting it equal to the inverse of the ratio of the total number of real events to the total number of background events, where real and background are defined below. Also, due to problems associated with taking the ratios of small numbers[44] that result from the moderate–sized data samples available, the value of C_{ij} is not calculated. Rather, one chooses C_{ij} to maximize the agreement in this equation

$$R_{ij} = C_{ij} \cdot B_{ij} \tag{6.52}$$

where the R_{ij} are the real events per bin and the B_{ij} are the background, or fake, events per bin. These are given by

$$R_{ij} = \sum_{\alpha} \delta(\vec{p}_{\alpha 1} \in i)\delta(\vec{p}_{\alpha 2} \in j) \tag{6.53}$$

$$B_{ij} = \frac{1}{AN} \sum_{\beta} \sum_{\gamma} W(\beta)W(\gamma)\rho_{\beta\gamma}\delta(\vec{p}_{\beta 1} \in i)\delta(\vec{p}_{\gamma 1} \in j) \tag{6.54}$$

since the ratio of R_{ij} and B_{ij} is just Eq. 6.48.

6.5 Momentum Difference (Q) Histograms

For convenience, the calculation has used momentum bins to derive the residual correlation and the event weighting used to eliminate it. However, now that this has been done, there is no longer any explicit reference to the binning assumed. Therefore the histogramming assumed in Eqs. 6.53 and 6.54 can be changed without effecting the validity of the event weighting.

Recalling derivation of the correlation function (Chapter 3), the natural variables to use are $q_\perp$, $q_{||}$ and q_0, the components of the momentum difference of the pions, and the energy difference. Taking one index for each of $q_\perp$, $q_{||}$ and q_0, the natural enumeration of the histogram bins[6] is a triplet of indices, ijk. So now letting ijk stand for the ijk^{th} **Q** bin and using the four vector **Q** explicitly (and adding the normalization factor D)

[6] This experiment used histograms 25 bins on each of the three sides. The bin width was 10 MeV/c (or MeV, for q_0).

Equations 6.52, 6.53 and 6.54 become

$$R_{ijk} = D \cdot C_{ijk} \cdot B_{ijk} \tag{6.55}$$

$$R_{ijk} = \sum_{\alpha} \delta(\{\mathbf{P}_{\alpha 1} - \mathbf{P}_{\alpha 2}\} \in ijk) \tag{6.56}$$

$$B_{ijk} = \sum_{\beta} \sum_{\gamma} W(\beta) W(\gamma) \rho_{\beta\gamma} \delta(\{\mathbf{P}_{\beta 1} - \mathbf{P}_{\gamma 1}\} \in ijk) \tag{6.57}$$

where ijk refers to the ijk^{th} $\mathbf{Q}$ bin.

The $W(\beta)$ and $W(\gamma)$ are calculated according to Eq. 6.49 and 6.50, where the overall normalization (A) in the last iteration of the weights is ignored. This is done for the sake of computing speed; Since the normalization of the C_{ijk} is fit this changes only the value of the normalization and does not change the value of any of the physically significant parameters.[7] The form for C_{ijk} used is that of Eq. 3.14, where $q_{\perp}$, $q_{||}$ and q_0 are evaluated at the center of the ijk^{th} $\mathbf{Q}$ bin.

6.6 Background Fluctuations

The number of counts in the background histogram is defined by Eq. 6.57

$$B_{ijk} = \sum_{\beta} \sum_{\gamma} W(\beta) W(\gamma) \rho_{\beta\gamma} \delta(\{\mathbf{P}_{\beta 1} - \mathbf{P}_{\gamma 1}\} \in ijk) \, .$$

Because of the weight factors, the statistical fluctuation in the bins is not just the square root of the number of counts. Regarding each event as a bin with one count in it by taking the uncertainty in counting each weighted event as equal to the event weight, the estimated uncertainty in B_{ijk} is (using Δ to denote the uncertainty in a quantity)

$$\begin{aligned}(\Delta B_{ijk})^2 &= \sum_{\beta} \left\{ \sum_{\gamma} W(\beta) W(\gamma) \rho_{\beta\gamma} \delta(\{\mathbf{P}_{\beta 1} - \mathbf{P}_{\gamma 1}\} \in ijk) \right\}^2 \\ &+ \sum_{\gamma} \left\{ \sum_{\beta} W(\beta) W(\gamma) \rho_{\beta\gamma} \delta(\{\mathbf{P}_{\beta 1} - \mathbf{P}_{\gamma 1}\} \in ijk) \right\}^2 \end{aligned} \tag{6.58}$$

where the two terms are due to each event appearing twice, once in the β sum and once in the γ sum, in the function $\delta(\{\mathbf{P}_{\beta 1} - \mathbf{P}_{\gamma 1}\} \in ijk)$. In the second term interchange

[7] While on the topic of computing speed, I note that Eq. 6.50 and Eq. 6.57 both require double loops over all events, hence go as N^2. I do not think that the N^2 behavior of Eq. 6.50 can be eliminated.

the dummy summation labels, and use the fact that $\rho_{\beta\gamma}$ and $\delta(\{\mathbf{P}_{\beta 1} - \mathbf{P}_{\gamma 1}\} \in ijk)$ are symmetric functions, to find that

$$(\Delta B_{ijk})^2 = 2\sum_{\beta}\left\{\sum_{\gamma} W(\beta)W(\gamma)\rho_{\beta\gamma}\delta(\{\mathbf{P}_{\beta 1} - \mathbf{P}_{\gamma 1}\} \in ijk)\right\}^2 . \qquad (6.59)$$

A plot of the fractional uncertainty $(\Delta B/B)$ is shown in Fig. 6.1. To eliminate those bins where the uncertainty is very large, a cut is made requiring that the fractional uncertainty be less than 30%. This cut is found to not change the fitted values at all, but improves the Principle of Maximum Likelihood fit. Note that, for N = the number of events, $\Delta B_{ijk} \sim \mathcal{O}(N^{3/2})$ and $B_{ijk} \sim \mathcal{O}(N^2)$ so that the fractional error $\Delta B_{ijk}/B_{ijk} \sim \mathcal{O}(N^{3/4})$.

6.7 Other Corrections

The discussion of the fitting procedures has ignored the Coulomb interactions of the pions with each other and with the nuclear fragments. These effects are handled as described in [1]. The formulas used there, and in this work, are from Gyulassy and Kauffmann[45] and the temperatures required for the formulas come from the Nagamiya group[39, 40] and Sullivan *et al.*[46].

The pion–nuclear matter correction is handled by correcting the individual pion's momentum before histogramming, which does not alter any of the derivations given above. This correction involves the Coulomb interaction between the pion and the target fragment, the source and the projectile fragment. The assumed distribution of the nuclear charge between the projectile fragment, the interaction region and the target fragment is 20%, 60% and 20%, based on the average impact parameter. The pion–pion correction is handled by weighting the background events with the Gamow factor,[8] to reflect the detection probability for a pion pair with a given momentum difference. This introduces a weighting factor in the calculation of the background that would be placed in Eq. 6.57 next to the $\rho_{\beta\gamma}$ term. This term is symmetric in the two pion momenta and the derivation of the uncertainty in B_{ijk} can follow the one given above.

[8] See, for example, [47].

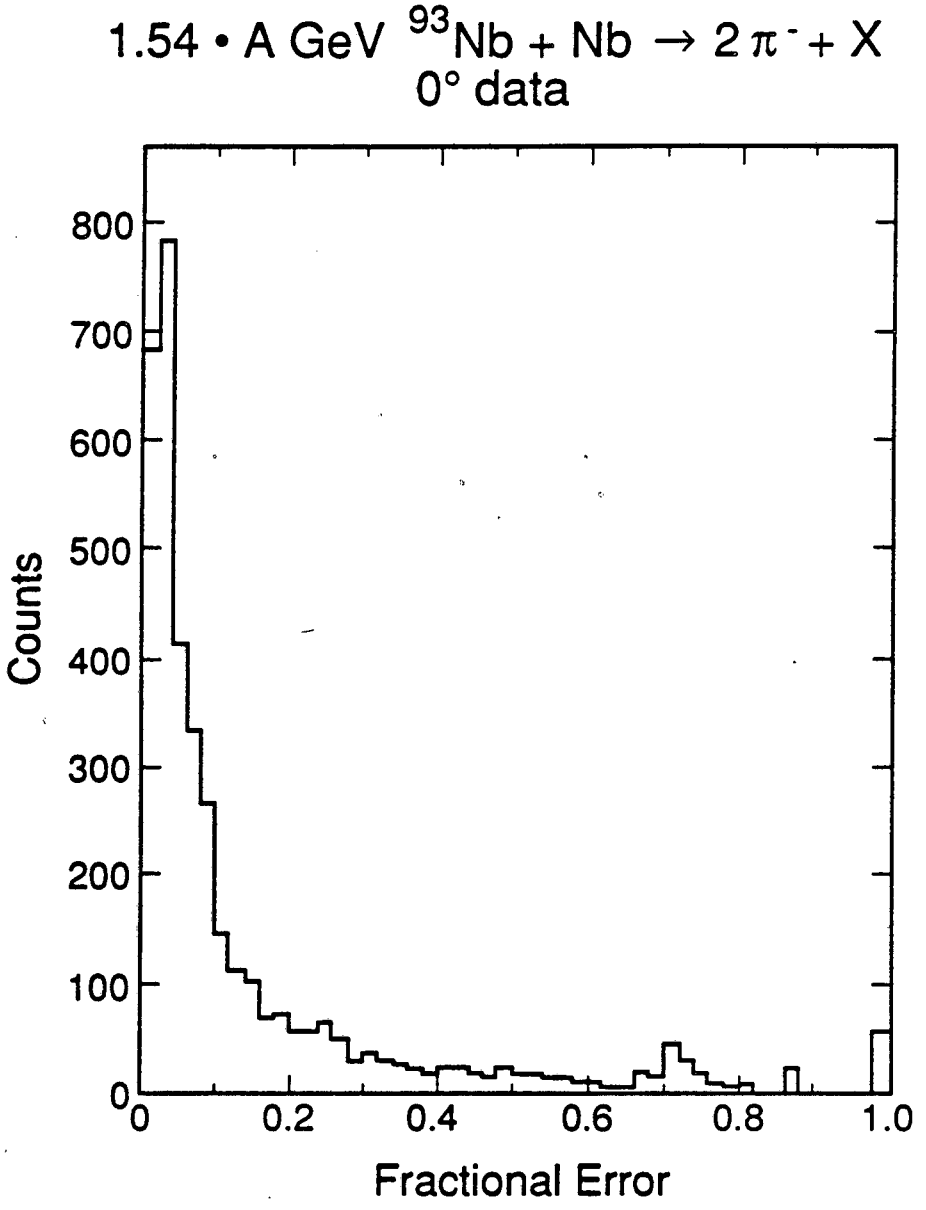

Figure 6.1: Estimated fractional uncertainty in the background.

6.8 Fitting the Correlation Function

When fitting the correlation function there are three areas of concern. The first is what function of the data should be minimized to extract the parameters, the second is what are the statistical uncertainties in the extracted parameters, and the third is how to estimate the probability that the theory used describes the data.

There are $25^3 = 15625$ bins in the histograms,[9] so the average number of counts per bin is small and therefore, the correlation function cannot be calculated by just calculating R_{ijk}/B_{ijk} and then trying to fit a curve using a least squares fit. Instead, the Principle of Maximum Likelihood is used. In its most general form, one attempts to maximize the probability that the measured data came from the theory, by varying parameters in the theory[48]. The details of applying the principle to this problem are given in [1] and the main results will be summarized here. When applied to this experiment, one maximizes the probability that the real counts in a bin came from the measurement of a number of counts equal to the background counts in that bin times the correlation function. Assuming that the real counts are Poisson distributed, and that the fluctuations in the predicted values (e.g., $D \cdot C_{ijk} \cdot B_{ijk}$) are negligible compared to the fluctuations in the real counts, this is

$$\Phi = \prod_{ijk} \frac{(D \cdot C_{ijk} \cdot B_{ijk})^{R_{ijk}}}{R_{ijk}!} e^{-D \cdot C_{ijk} \cdot B_{ijk}} \tag{6.60}$$

where the product is restricted to bins where $B_{ijk} \neq 0$. Based on Eq. 6.59 and the arguments given in [1], the estimated fluctuations in the background counts go as $n^{3/4}$. So, to make the fluctuations in the background counts small, all possible events are used in Eq. 6.57. When making the fits, it is easier computationally to minimize the quantity $F = -\ln \Phi$ rather than maximize the quantity Φ. The correlation function is then fit by adjusting the parameters in C_{ijk} (and D) to minimize F, the negative log of the likelihood function. The computer program used for the numerical minimization and estimates of the uncertainties was MINUIT[49].

The uncertainty estimates were made from contour plots of the log–likelihood function (F), where the contour of interest is that of the minimum value + 0.5. This contour would correspond to a 1σ level if this were a χ^2 fit. Note that the probability of *all* the parameters

[9] Recall the histograms used 25 bins on each of the three sides.

being inside this contour is about 10% for the number of parameters present in our fits[50]. The uncertainties given are taken from the tangent method, which uses the largest and smallest values inside the contour for a parameter, without regard to the values of the other parameters. This implies that the probability of this parameter's true value being within the uncertainty quoted is the same as for a 1σ interval, without regard to the values of the other parameters[50]. Some confidence contours and their corresponding uncertainties are given in Chapter 7.

There are two estimators of the quality of the fit (once the fit has been made) used in this experiment. The first is a restricted χ^2/NDF and the second is the $\chi^2_{\rm PML}$/NDF, as defined in Eq. 6.61.

The χ^2/NDF is calculated in the usual manner, however only those bins predicted (based on $D \cdot C_{ijk} \cdot B_{ijk}$) to have more than five counts are used[48]. The background fluctuations, as calculated in Section 6.6, are not included in the uncertainty estimates. The reason for the second was simply that it was found that including the fluctuations did not change the value very much (which is good since one wants the background fluctuations to be small). The reason for the first is that the χ^2 calculation assumes that the error distribution is Gaussian. Although the real spectrum is assumed to be Poisson distributed, for more than 5 counts per bin the two distributions are essentially identical. The distribution of the restricted χ^2 is that of a true χ^2 with the number of degrees of freedom in the range of N to $N - L$ where N is the number of bins, and L is the number of parameters in the fit[48]. Note that the number of degrees of freedom reported here is always $N - L$, where $L = 5$ for the two–radius parameter fits. This estimator has the virtue of allowing confidence levels to be estimated using standard methods, and one can verify the quality of the fit. This estimator has the failing of not being sensitive to the entire region that is being fit. However, since the fit is made using the Principle of Maximum Likelihood, the fit is unbiased and, presumably, the quality of the fit is the same in any region.

The $\chi^2_{\rm PML}$/NDF is derived from the Principle of Maximum Likelihood fitting method and is calculated according to the prescription of [1]. The parameters were fit by minimizing the quantity $F = -\ln \Phi$. The related quantity, $\chi^2_{\rm PML} = 2F + (\text{constant})$, has the additional property that it reduces to the usual χ^2 in the limit of sufficient statistics, if

the constant is chosen properly. With the proper constant the expression is

$$\chi^2_{\rm PML} = -2\ln\left\{\prod_{ijk}\frac{(D\cdot C_{ijk}\cdot B_{ijk})^{R_{ijk}}}{R_{ijk}!}e^{-D\cdot C_{ijk}\cdot B_{ijk}}\right\} - \sum_{ijk}\ln\{2\pi R_{ijk}\} \qquad (6.61)$$

where the product and the sum are restricted to those bins where $B_{ijk} \neq 0$. Although this estimator is unbiased even if the number of counts is small, it is difficult to determine exactly what the confidence levels are from standard methods, since the distribution is not known[50]. This estimator has the virtue of being unbiased and the flaw not not allowing confidence levels to be calculated.

6.9 Summary of the Fitting Procedure

The procedure for fitting the correlation function is then: a functional form for the C_{ijk} is assumed, and the free parameters (in Eq. 3.14 these are λ, $R_{||}$, $R_{\perp}$ and τ) are set to values corresponding to typical nuclear sizes. Equations 6.49, and 6.50 are used to calculate weights and Eq. 6.50 is iterated until stable to further iteration. The R_{ijk} and B_{ijk} are calculated from Eqs. 6.56 and 6.57 using the weights. The parameters in the correlation function are adjusted to maximize agreement in Eq. 6.55 to give new correlation function parameters. This correlation function is used to calculate new weights and the procedure is repeated until the correlation function parameters are stable to further iteration. Generally less than five iterations are required. This procedure has been checked using Monte Carlo data with a known correlation function (using Eq. 3.14) and has been verified to converge to the input parameter values. The results from the Monte Carlo tests are shown in Section 7.2.

Chapter 7

Results from the Correlation Function Fits

7.1 Presentation of the Data

The data (both the real counts and the background, or reference sample, counts) were histogrammed as a function of $q_{||}$, $q_{\perp}$ and q_0. The fits were made using these three dimensional histograms. Displaying the fits in the obvious fashion of fixing, for example, $q_{||}$, $q_{\perp}$ and showing the data as a function of q_0 has two features. The first is that there would be $25^2 = 625$ such displays, the second is that most of the bins in any given display would be empty, both from limited statistics and from the acceptance limits of the spectrometer in **Q** space.[1]

Therefore, averages are made over (again, for example) the $q_{||} - q_{\perp}$ plane, at a given value of q_0, to display averages of the quantities as a function of q_0. By using each of the three variables ($q_{||}$, $q_{\perp}$ and q_0) in turn, three displays are made showing the data and the fitted correlation function projected onto each of the coordinate axes. Note that these are averages weighted by the spectrometer's acceptance — the projections of the data and the fitted correlation function are both distorted by the acceptance.

The definition of the data points in the projection (C_k) is

$$C_k = \frac{\sum_{ij} R_{ijk}}{D \cdot \sum_{ij} B_{ijk}} \ , \tag{7.1}$$

[1] There is, in addition, the physical constraint that for particle pairs, $q_{||}^2 + q_{\perp}^2 \geq q_0^2$.

the uncertainty in the data points is estimated as

$$(\Delta C_k)^2 = C_k^2 \left\{ \frac{1}{\sum_{ij} R_{ijk}} + \frac{\sum_{ij} (\Delta B_{ijk})^2}{\sum_{ij} (B_{ijk})^2} \right\} , \tag{7.2}$$

and the fitted curve is given by

$$\langle C_k \rangle = \frac{\sum_{ij} C_{ijk} \cdot B_{ijk}}{\sum_{ij} B_{ijk}} , \tag{7.3}$$

where D is the over–all normalization constant (which is fit, see Eq. 6.55), R_{ijk} is the real counts per bin, B_{ijk} is the background (or reference sample) counts per bin and ΔB_{ijk} is the estimated uncertainty in the background counts per bin (see Eqs. 6.56, 6.57 and 6.59). In Equations 7.1, 7.2 and 7.3, the last index (k) was kept and the first and second indices (i and j) were averaged over. By keeping either the first, or the second, index (e.g., i or j) and averaging over the remaining indices, a total of three sets of similar equations can be produced, each set of equations corresponding to the averages as a function of one of q_0, $q_\perp$ and $q_{||}$. Note that if $R_{ijk} \simeq D \cdot C_{ijk} \cdot B_{ijk}$ the curves will be close to the data points. From Eq. 7.3 one can see how the averages are weighted by the spectrometer's acceptance.

7.2 Fits to Monte Carlo Data

Section 6.9 referred to a test of the correlation function fitting routines using Monte Carlo data with a known correlation function. The data for this test were generated so that the correlation function was the same as that predicted by the theory, Eq. 3.14, with $\lambda = 1$, $R_{||} = 3$, $R_\perp = 4$ and $\tau = 2$. The Monte Carlo pions were then processed by simulating the spectrometer as used in the 0° Nb set up with $|\vec{p}_{\rm proj}| > 50$ MeV/c (see Table 4.2). The Monte Carlo program is described in Appendix A. The data output from the Monte Carlo simulation were passed to the usual data analysis stream with the same geometrical cuts as used in the real data analysis. The only difference was that the pulse–height and time–of–flight cuts in the scintillation counters were not used since particle contamination was not simulated. This procedure gives a close approximation to the spectrometer's momentum limits and two track efficiency effects.

Table 7.1 shows the parameters extracted from the fit to the Monte Carlo data. The confidence level for this fit (based on the χ^2/NDF, see Section 6.8) is 55%. In Figures 7.1,

Parameter	Input value	Fitted value
$R_\perp$(fm)	4.0	3.8 ± 0.2
$R_{\|\|}$(fm)	3.0	3.2 ± 0.3
τ(fm/c)	2.0	$2.2^{+0.6}_{-0.4}$
λ	1.0	0.98 ± 0.05
χ^2/NDF	-	595/600
χ^2_{PML}/NDF	-	2646/2359
Events	-	14000

Table 7.1: Parameters extracted from Monte Carlo simulated events. Only statistical uncertainties are shown.

7.2 and 7.3 the projections for this fit are shown. In Figures 7.4, 7.5 and 7.6 the corresponding confidence contours are shown.

In Figures 7.1, 7.2 and 7.3 some effects of the spectrometer's acceptance can be seen: First, the intercept as $q \rightarrow 0$ is not $C_2 = 1 + \lambda$ as one might expect from Eq. 3.14. This is because the average at, for example, $q_0 = 0$ includes bins where $q_\perp$ and $q_{||}$ are not zero, and $C_2 < 1 + \lambda$. Similar arguments apply for the other projections. Second, the shapes of the data and the fitted curves do not follow Eq. 3.14, the most obvious being for $q_{||}$ in Fig. 7.3. However, the projections for both the data and the fitted correlation function have the same shape indicating that this is an acceptance effect. See Equation 7.3 to see how the fitted correlation function is weighted by the acceptance.

One can see that a spectrometer with a limited angular acceptance couples the determination of the radius parameter parallel to the direction of observation and the lifetime parameter. The cause can be visualized by imagining two pion momentum vectors constrained to be within some small angular range. The variation of angle (at a fixed energy) gives momentum differences perpendicular to the average $\vec{p}$ of about $q_{\mathrm{perpendicular}} \approx |\vec{p}|2\cos(\frac{\Delta\theta}{2})$, which is large. Therefore, the momentum difference perpendicular to the pion momentum is decoupled from the energy difference, and the lifetime parameter is decoupled from the corresponding radius parameter. The variation of angle (at a fixed energy) gives momentum differences parallel to the average $\vec{p}$ of about $q_{\mathrm{parallel}} \approx |\vec{p}|2\sin(\frac{\Delta\theta}{2})$, which is small, whereas varying $|\vec{p}|$ gives large variations in the

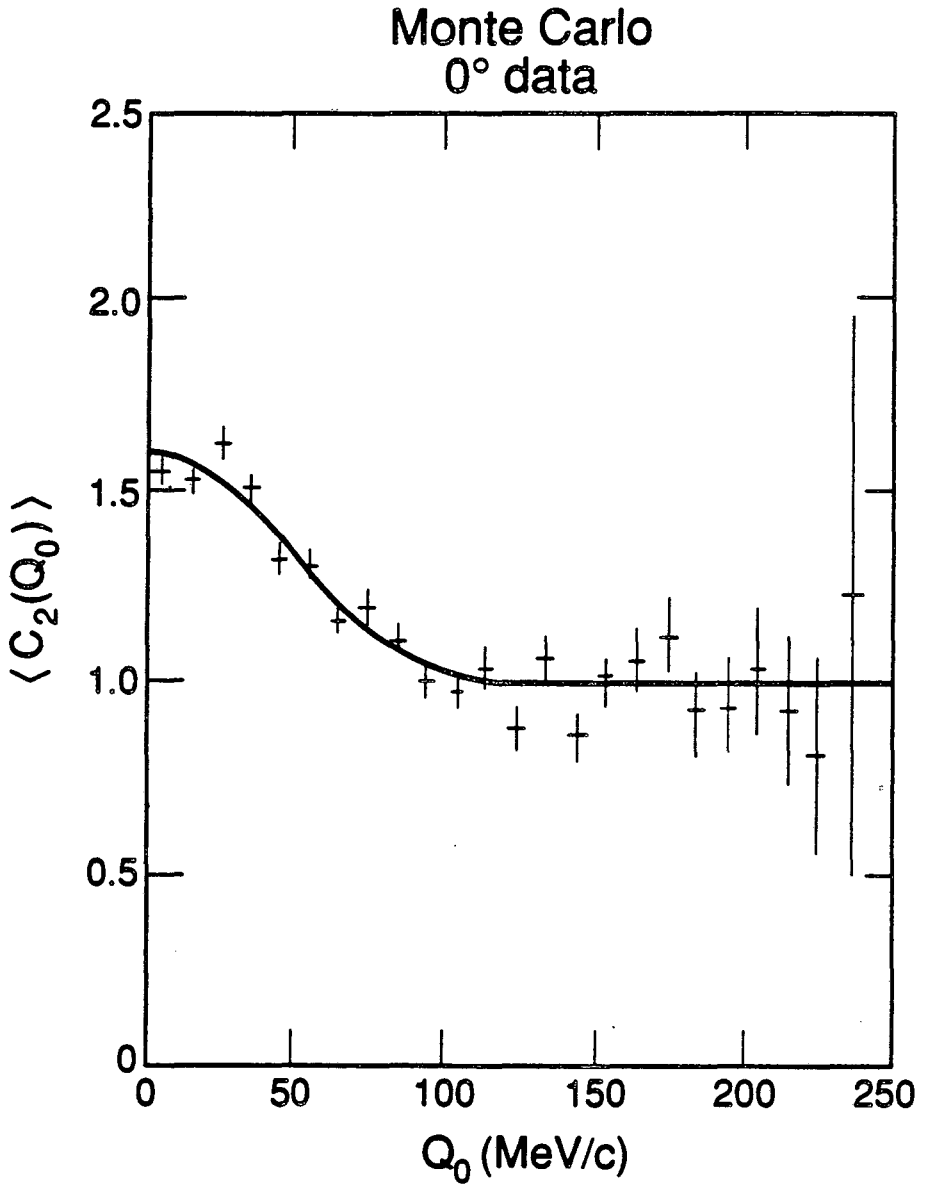

Figure 7.1: $\langle C(q_0) \rangle$ for the Monte Carlo data. Only statistical uncertainties are shown.

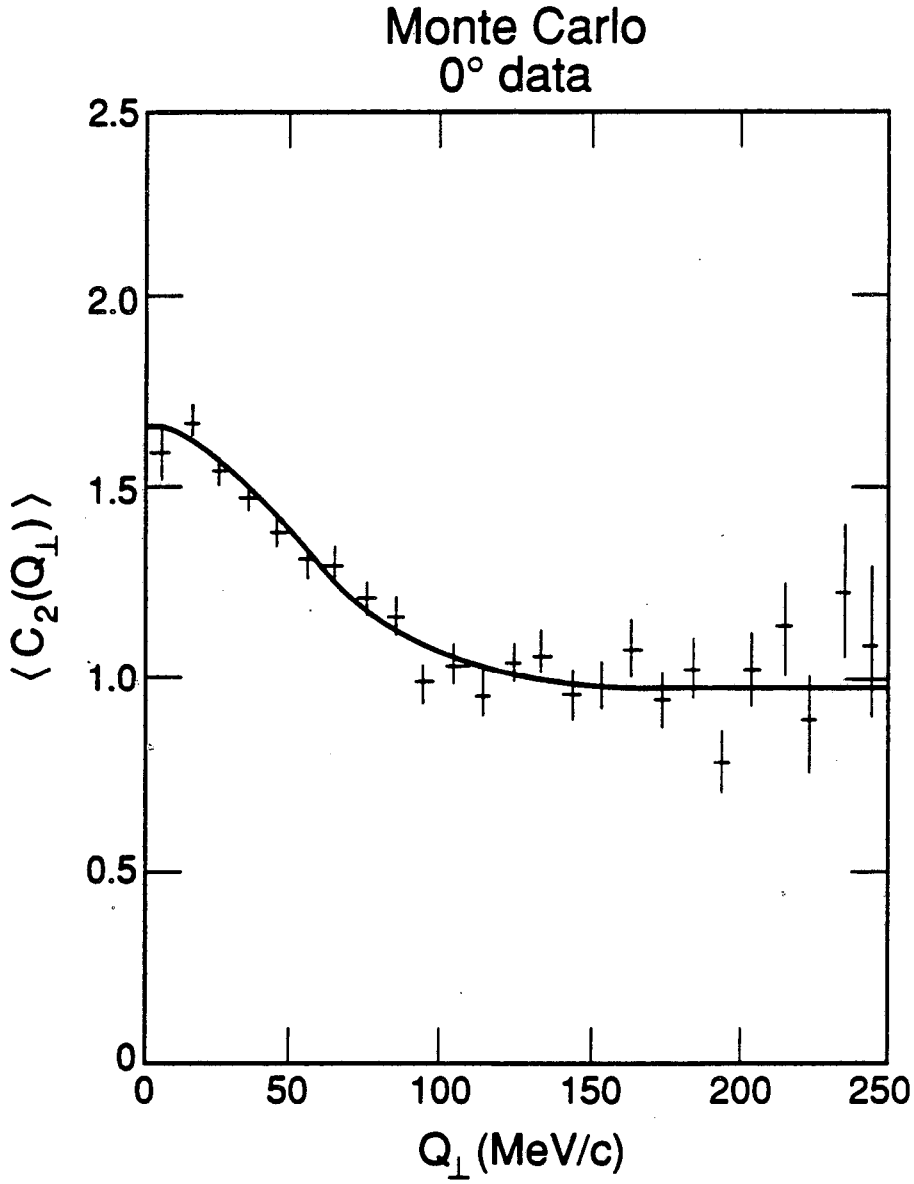

Figure 7.2: $\langle C(q_\perp) \rangle$ for the Monte Carlo data. Only statistical uncertainties are shown.

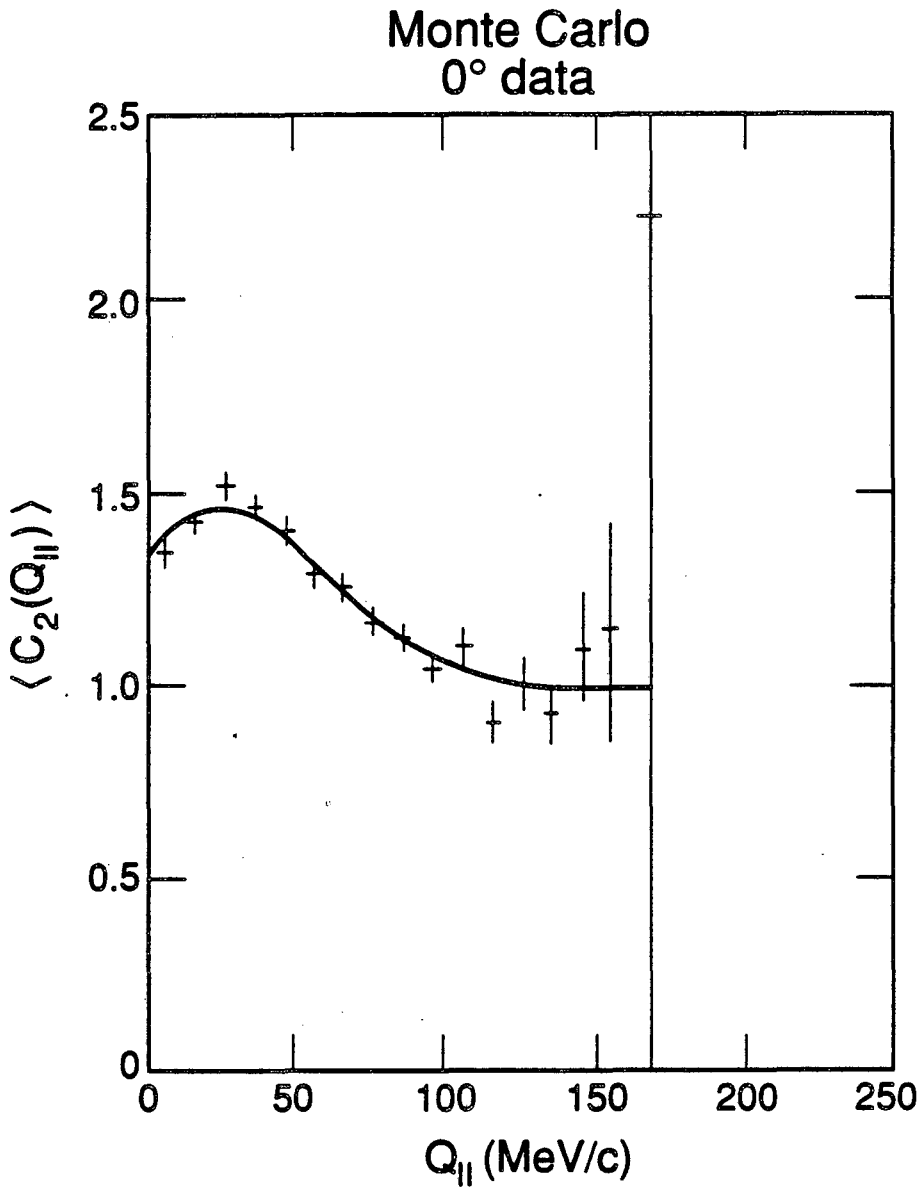

Figure 7.3: $\langle C(q_{||}) \rangle$ for the Monte Carlo data. Only statistical uncertainties are shown.

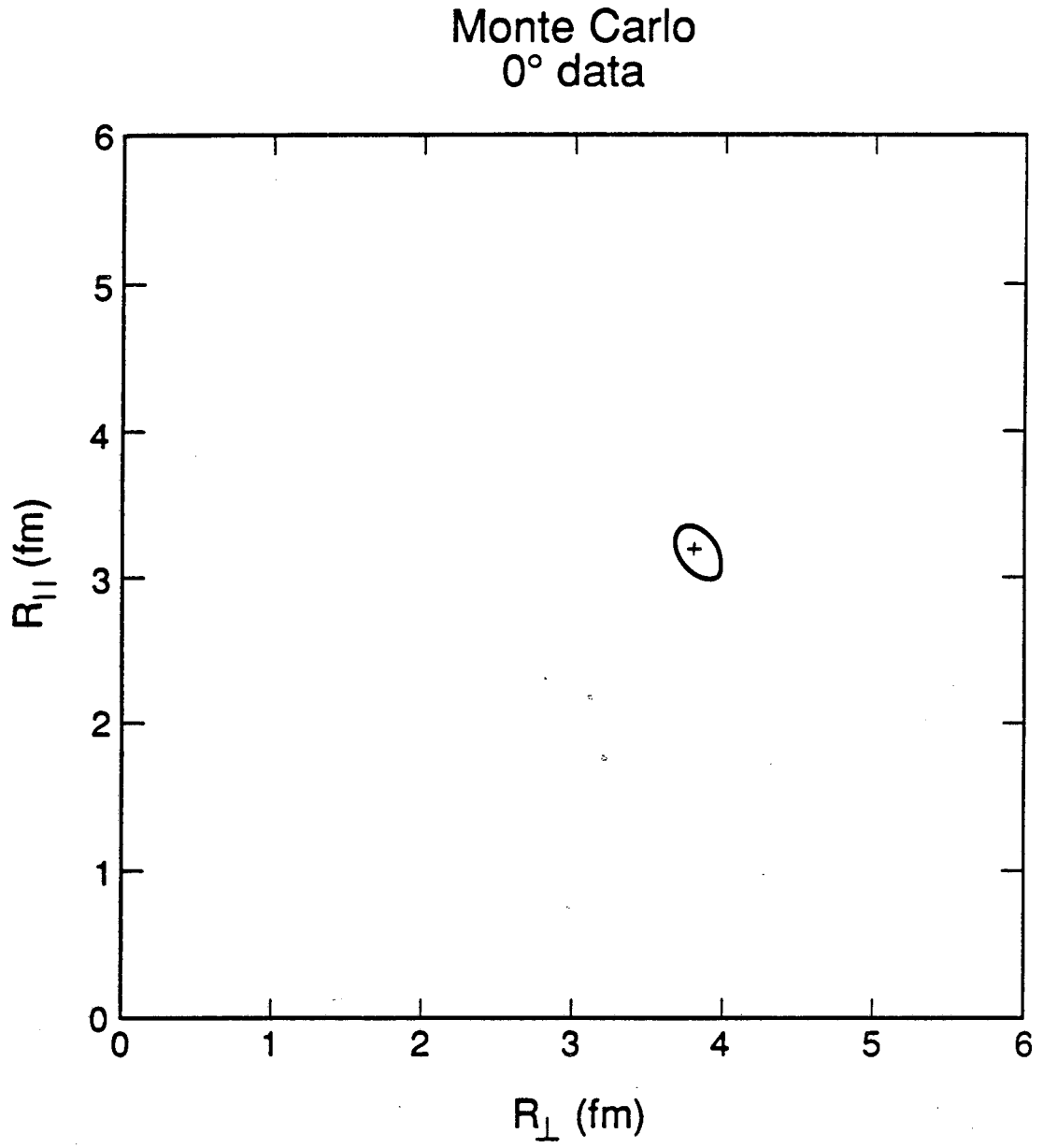

Figure 7.4: The 1σ confidence contour for the Monte Carlo data — $R_{||}$ vs. $R_{\perp}$ plane.

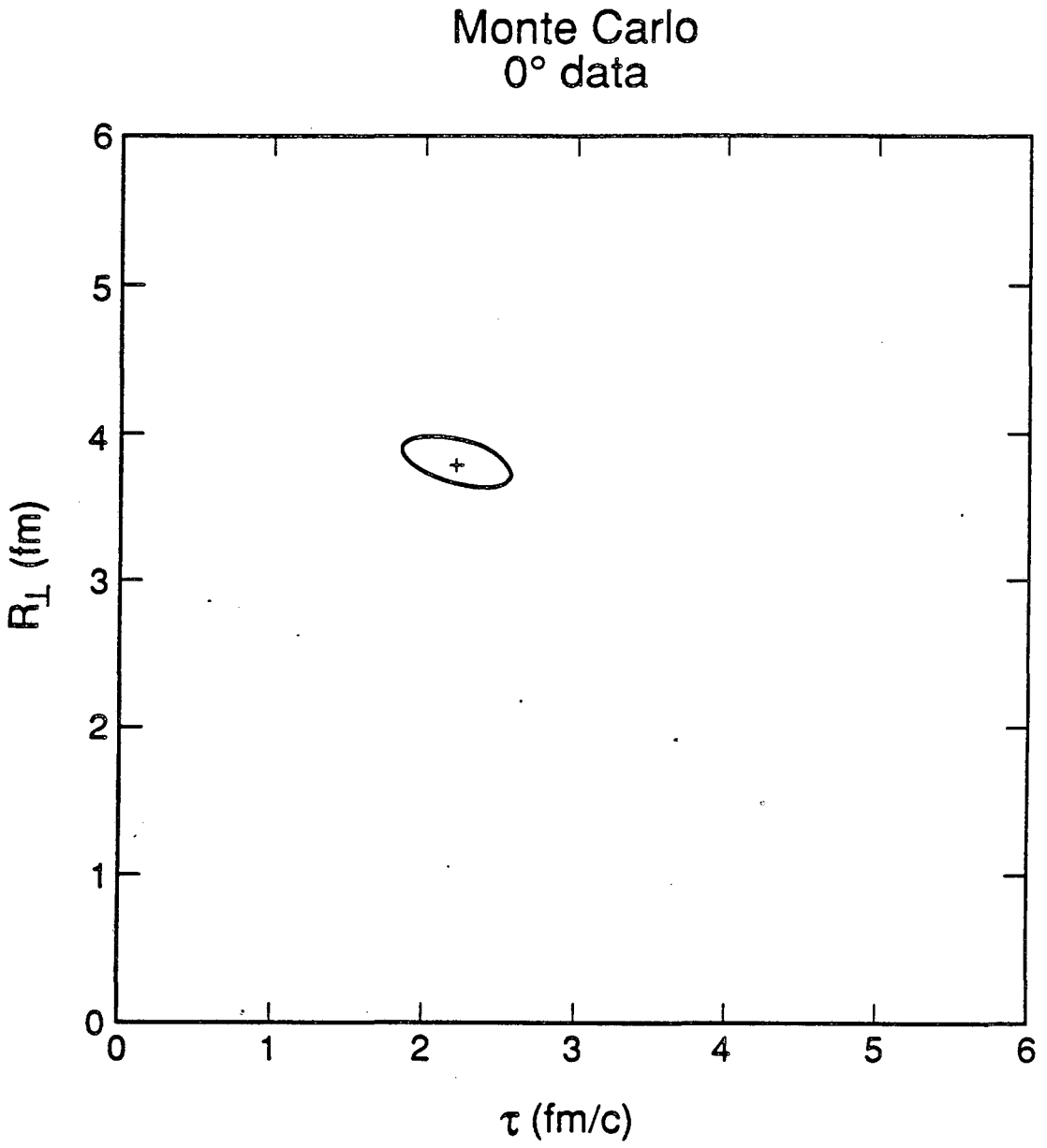

Figure 7.5: The 1σ confidence contour for the Monte Carlo data — $R_\perp$ vs. τ plane.

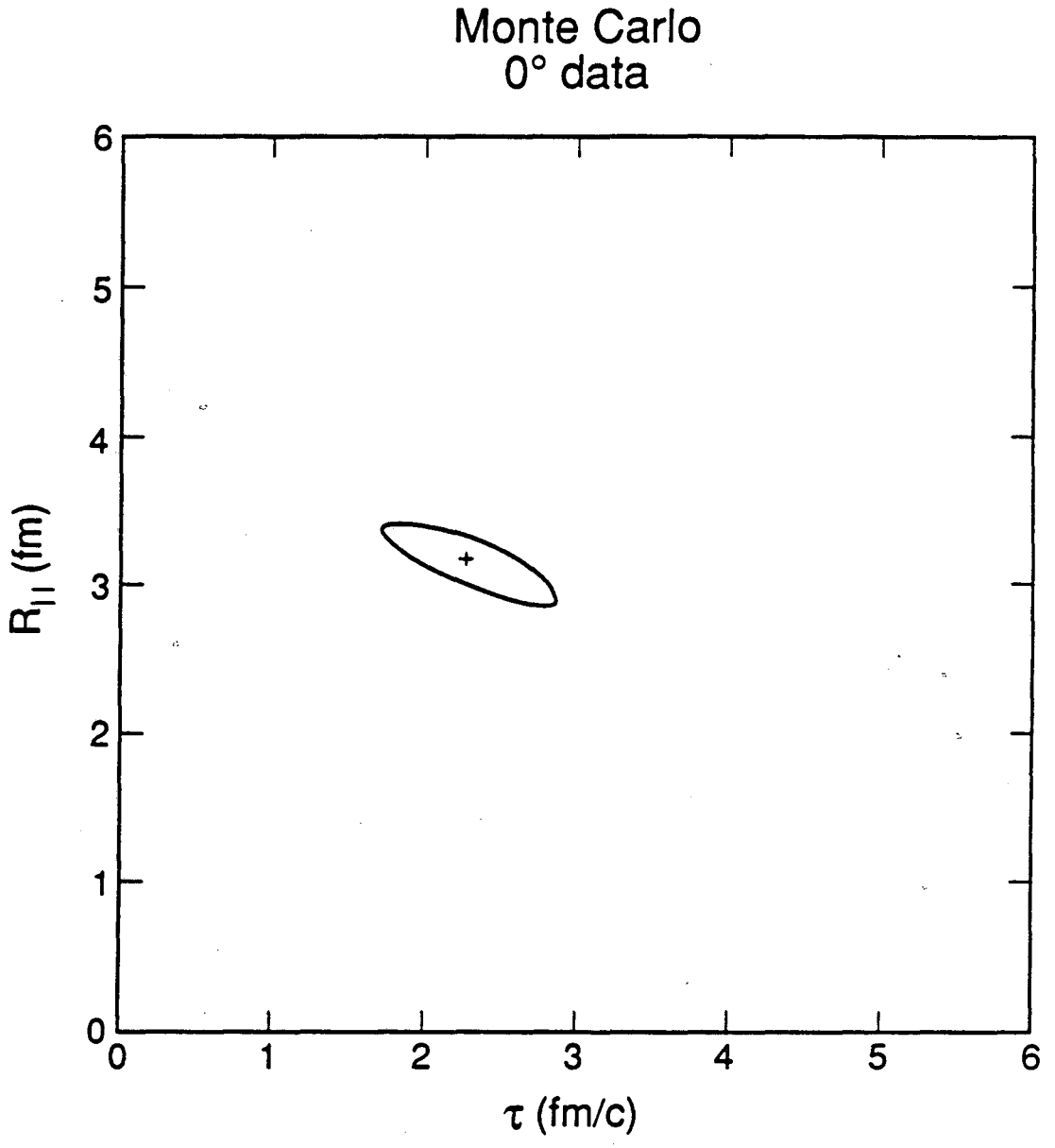

Figure 7.6: The 1σ confidence contour for the Monte Carlo data — $R_{||}$ vs. τ plane.

momentum difference parallel to the average momentum while varying the energy difference as well. Therefore, the momentum difference parallel to the direction of observation will be coupled to the energy difference and one cannot easily separate the lifetime and the corresponding radius parameter.

In the confidence contour plots a coupling between two variables causes the principle axes of the confidence contour ellipse to not be parallel to the coordinate axes. Instead, the axes are parallel to whatever combinations of the variables are independent. In the confidence contour plots for the Monte Carlo data one can see the greater coupling between $R_{||}$ and τ, than between $R_{\perp}$ and τ. Note that the Monte Carlo was a simulation of the 0° spectrometer where this is expected since the pion momenta are constrained to be to within an angular range close to the beam axis.

7.3 Projections for the Data

Figures 7.7, 7.8 and 7.9 show the projections for the 0° Nb π^- data sample with $|\vec{p}_{\rm proj}| >$ 50 MeV/c. This data sample was chosen for display since it is the largest data sample and, correspondingly, has the smallest statistical uncertainty in the data points. For this reason any systematic effects will be the most apparent in this data set. These plots do not show any systematic differences between the data and the correlation function used to fit the data. Note the similarities between the 0° data and the Monte Carlo, which was a simulation of the 0° data. For comparison, the projections from the 45° Nb uncut data sample (this data sample is uncut in the sense that no cuts have been imposed that would remove correctly reconstructed pions, see Section 7.7) are shown in Figures 7.10, 7.11 and 7.12. This is a slightly smaller data set, but again, no systematic differences between the data and the fitted correlation function can be seen. The parameters deduced from these fits are listed in Tables 7.5 and 7.7 (which appear later in Section 7.7).

The projections, of course, reduce the amount of data output (from $25^3 = 15625$ bins to $3 \times 25 = 75$ bins), so some information is lost in making the projections. This means that there are some possible systematic effects that could be masked in the projections. For example, bins along the line given by $q_0 = q_{||} = q_{\perp}$ could be high (or low), and this would not show in the projections. However, calculations of the confidence levels from the χ^2/NDF (see Section 6.8) have verified that the confidence levels are acceptable.

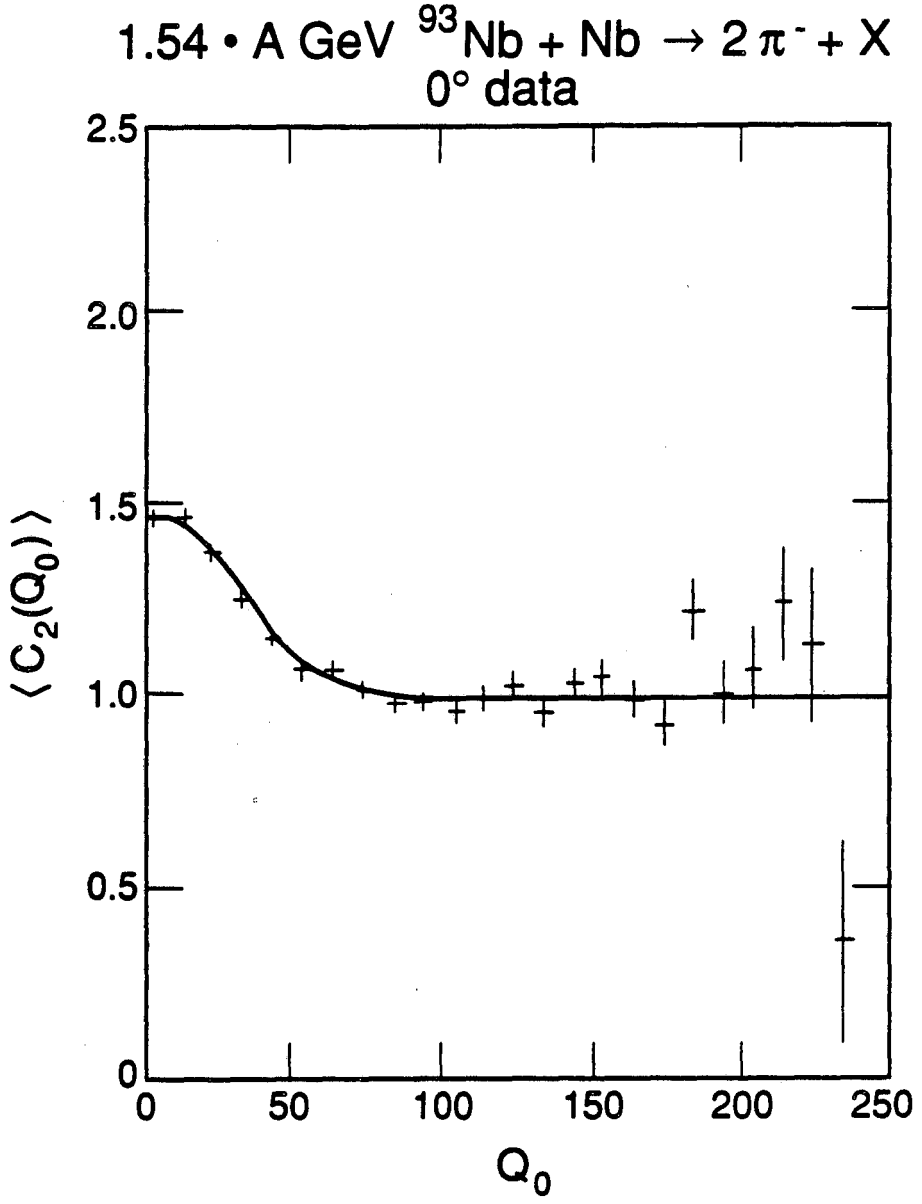

Figure 7.7: $\langle C(q_0) \rangle$ for the 0° Nb least cut data. Only statistical uncertainties are shown.

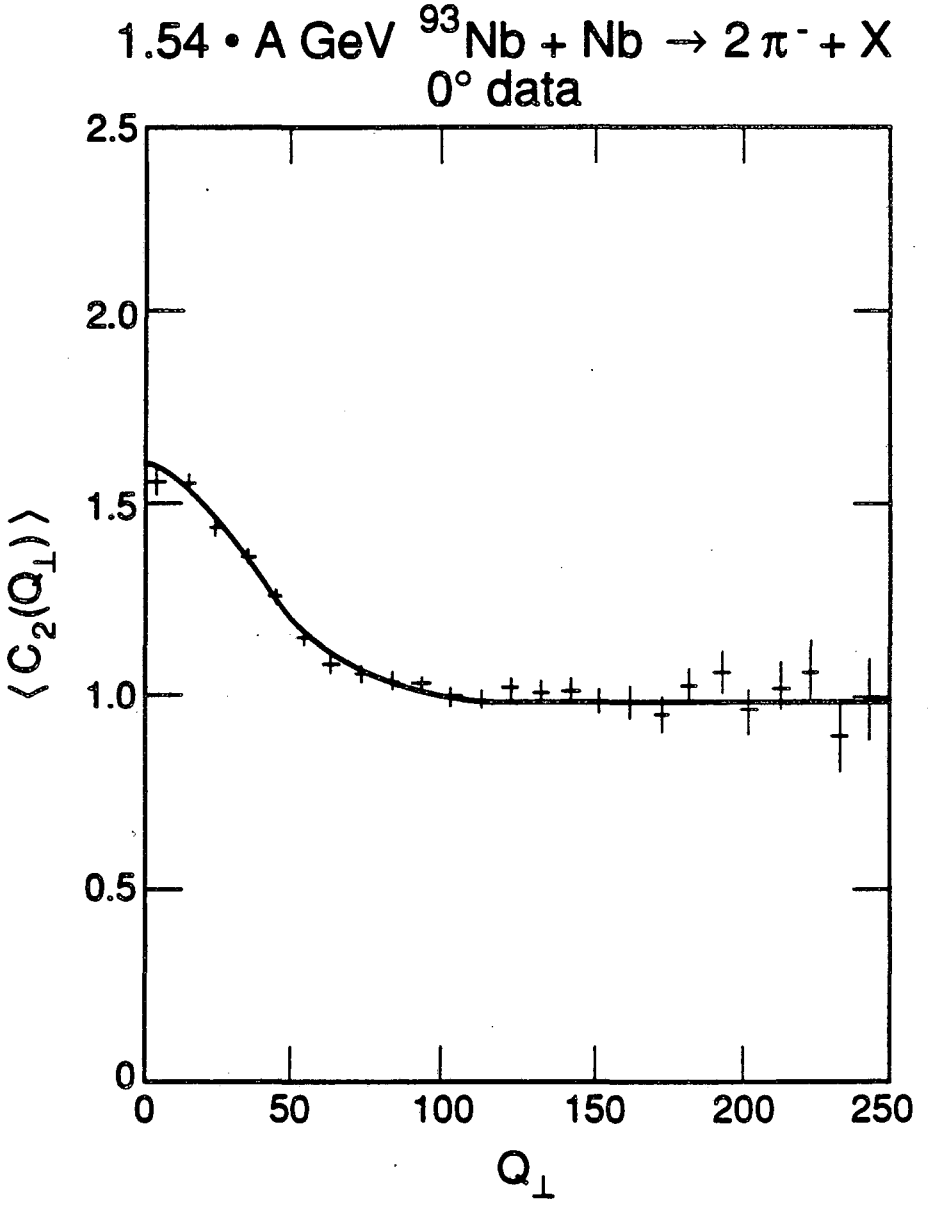

Figure 7.8: $\langle C(q_\perp) \rangle$ for the 0° Nb least cut data. Only statistical uncertainties are shown.

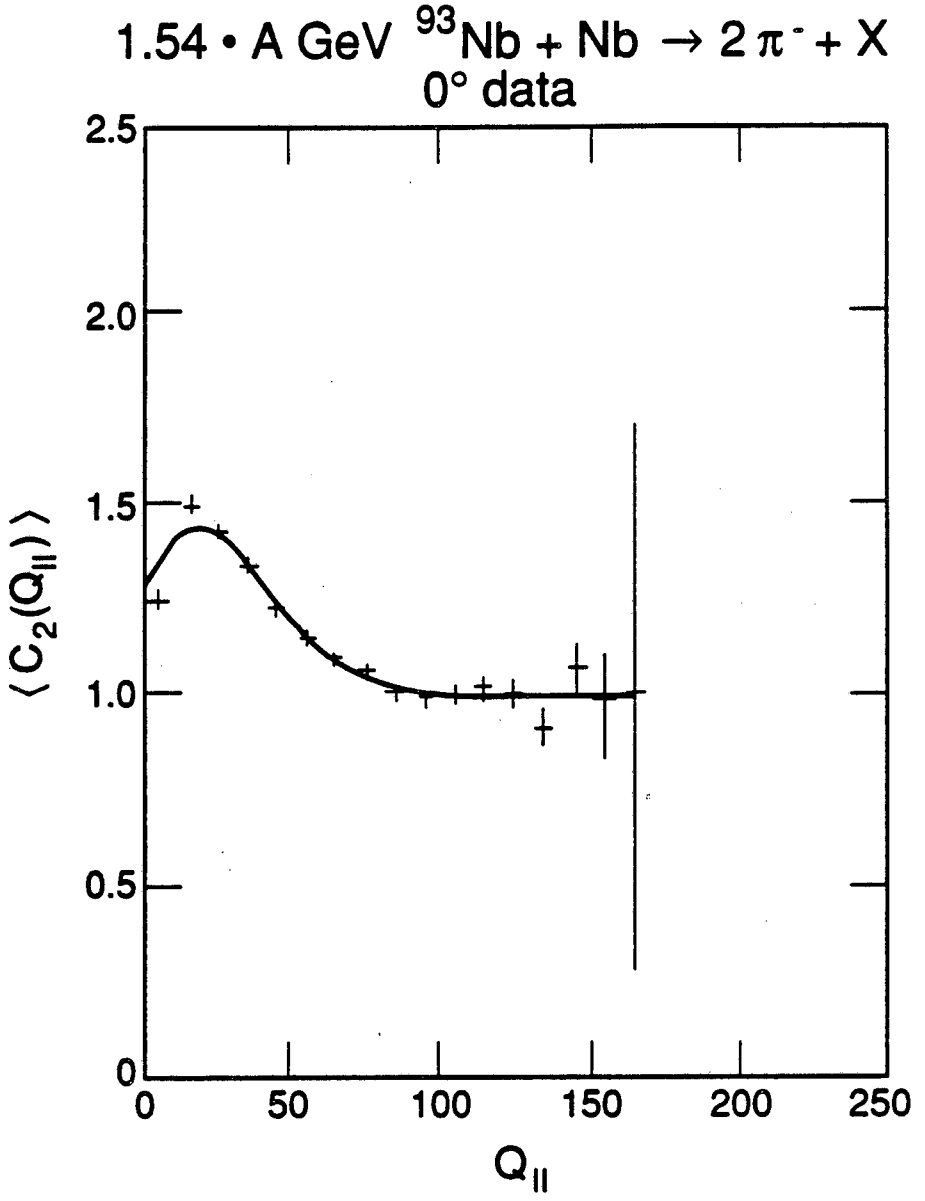

Figure 7.9: $\langle C(q_{\|})\rangle$ for the 0° Nb least cut data. Only statistical uncertainties are shown.

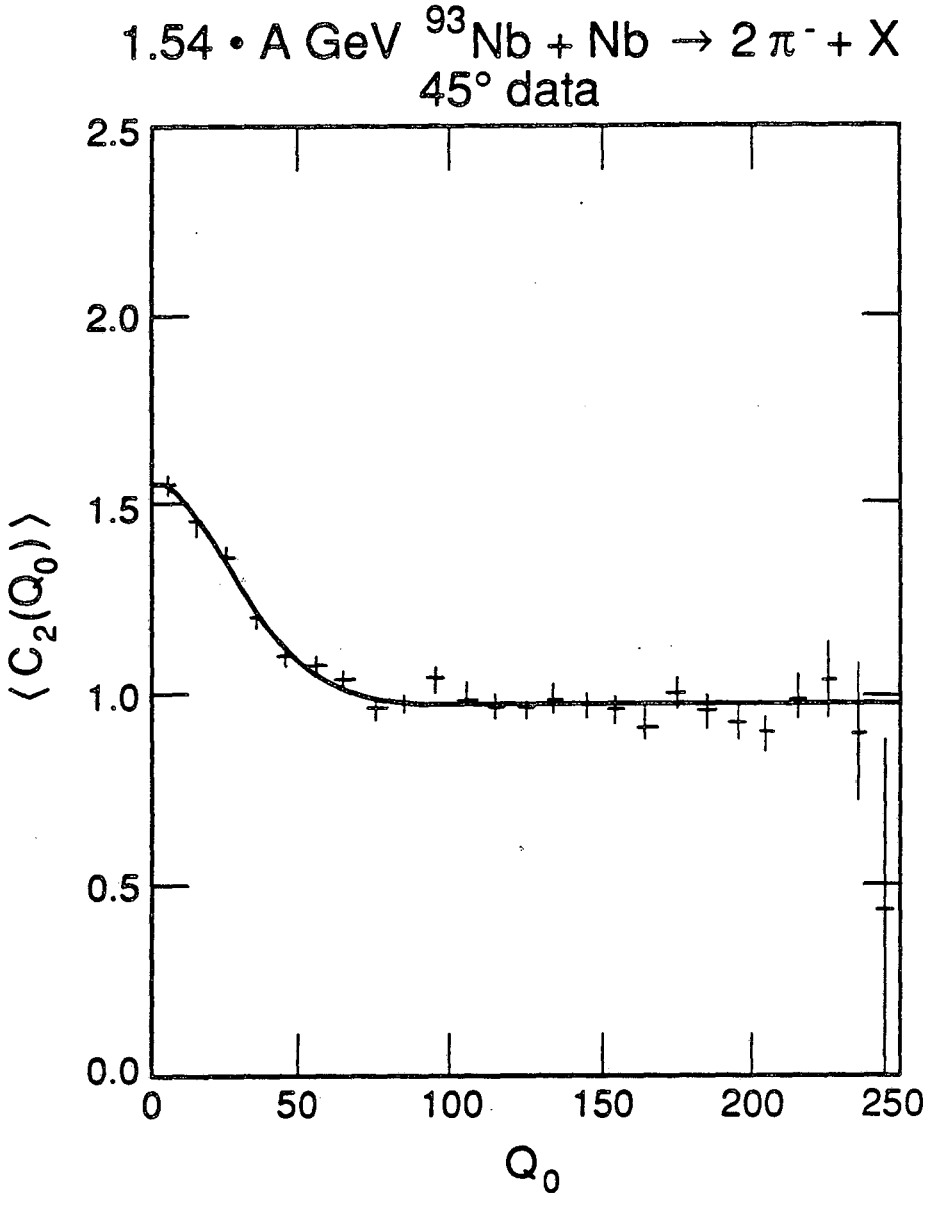

Figure 7.10: $\langle C(q_0) \rangle$ for the 45° Nb uncut data. Only statistical uncertainties are shown.

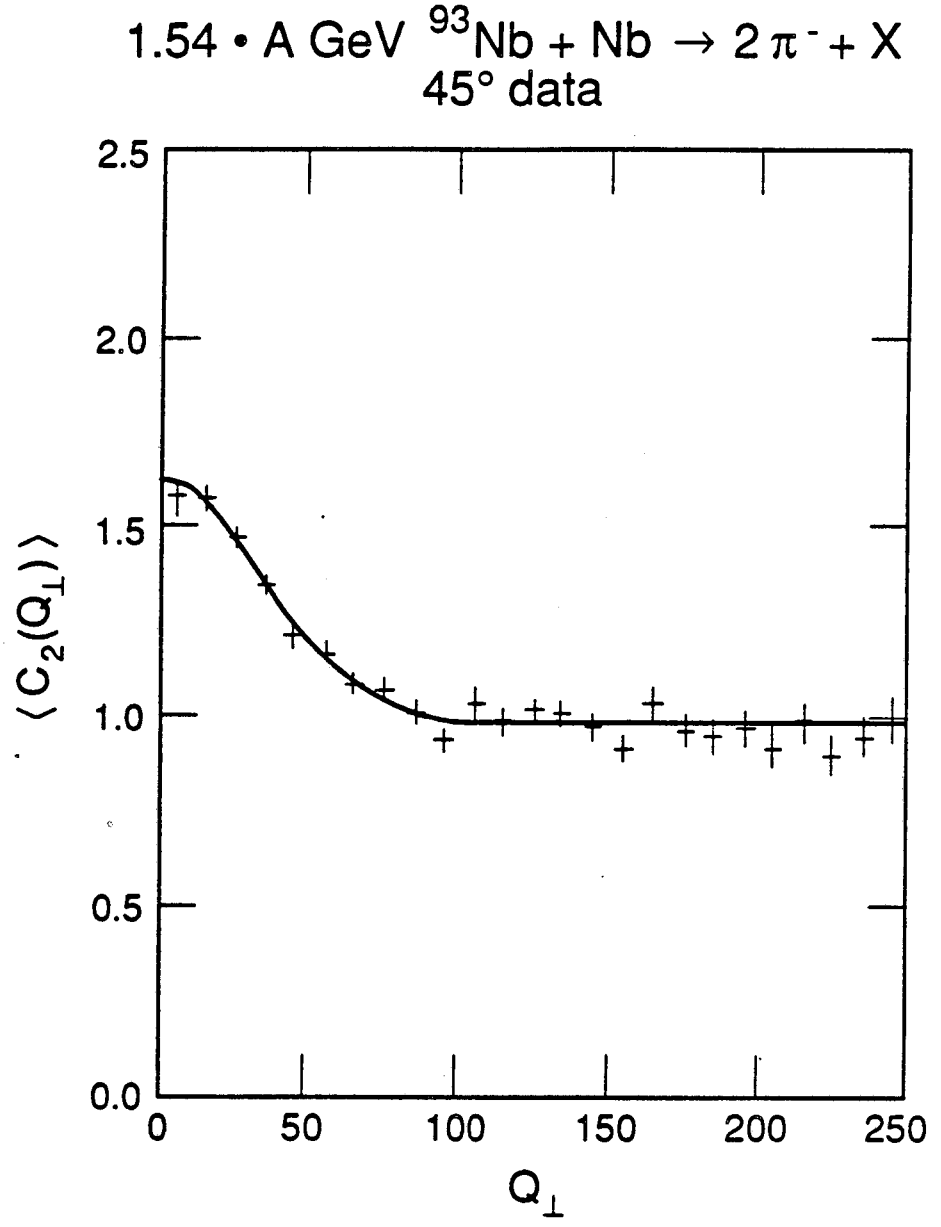

Figure 7.11: $\langle C(q_\perp) \rangle$ for the 45° Nb uncut data. Only statistical uncertainties are shown.

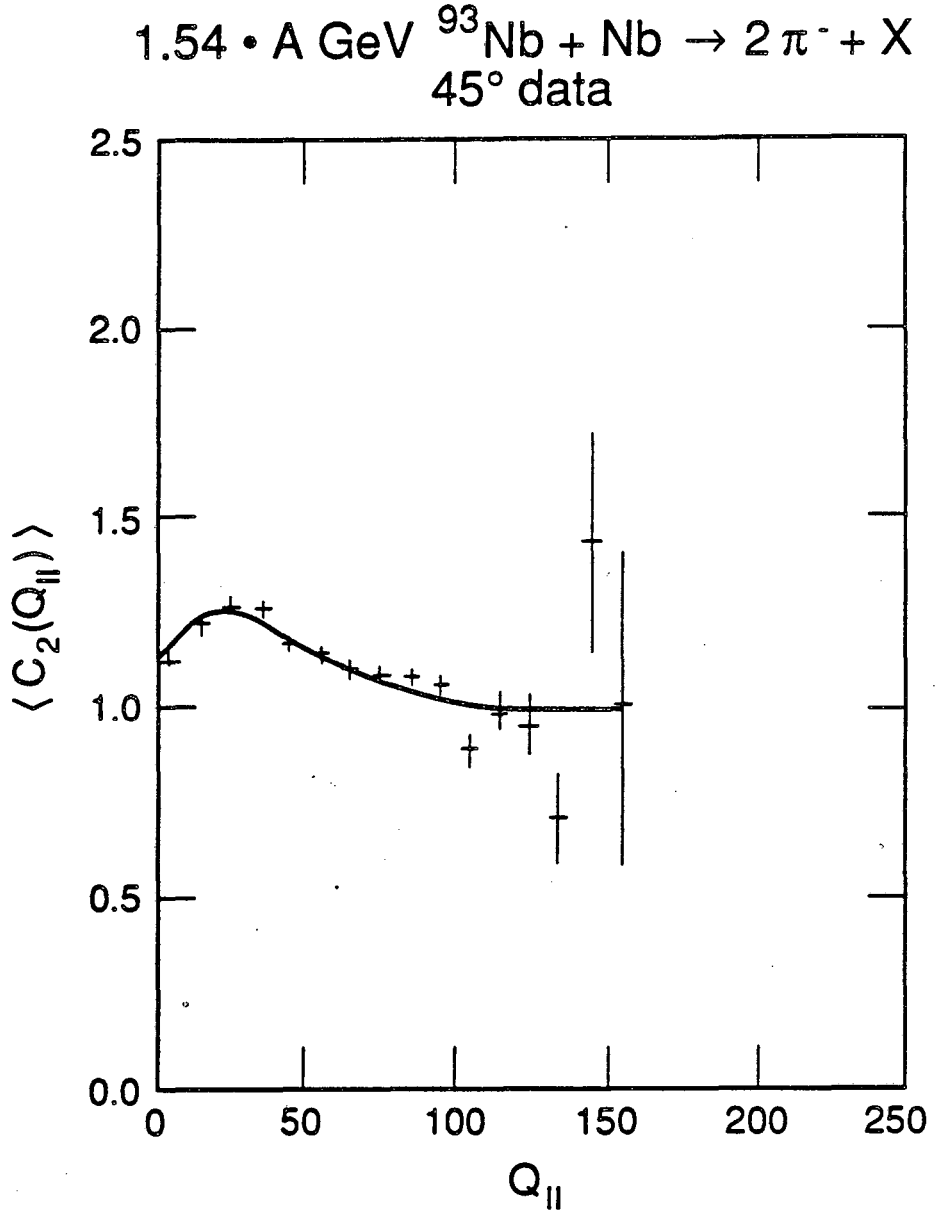

Figure 7.12: $\langle C(q_{\|}) \rangle$ for the 45° Nb uncut data. Only statistical uncertainties are shown.

7.4 Confidence Contours for the Data

Figures 7.13, 7.14 and 7.15 show confidence contours for fits to the 0° Nb π^- data sample with $|\vec{p}_{\rm proj}| > 100$ MeV/c, and Figures 7.16, 7.17 and 7.18 show confidence contours for the 45° Nb data with $|\vec{p}_{\rm cm}| > 150$ MeV/c. The shapes of the contours are typical of the contours for all of the data sets, although for the data sets with fewer events the error contours can intersect zero. Figure 7.19 shows the contour for one such case. The data in this plot are for the 0° Ar data sample with $|\vec{p}_{\rm proj}| > 50$ MeV/c; however, the appearance is typical for an error contour intersecting zero. Note that for the 0° Nb data, $R_{||}$ is more correlated with τ than $R_{\perp}$ is. For the 45° Nb data the situation is reversed, and the independence of $R_{||}$ and τ is clearer than for $R_{\perp}$ and τ in the 0° case. The values of the parameters for these fits, and the uncertainties, are given in Tables 7.6, 7.8 (for Nb) and 7.7 (for Ar).

7.5 Study of the Coulomb Corrections

The Coulomb correction between the pions and the nuclear matter, and the correction between the two pions in the event (the corresponding correction is called the Gamow correction, although it is a Coulomb interaction), were discussed in Section 6.7. In principle one has to solve the n–body interaction problem to determine the corrections accurately. To determine if the assumption that the interactions can be separated is acceptable, a study was made using about 1/3 of the 0° Fe data (with $|\vec{p}_{\rm proj}| > 50$ MeV/c), where fits were made with all possible combinations of the two corrections being made or not. The parameters extracted from the fits are given in Table 7.2. Note that the $|\vec{p}_{\rm proj}| > 50$ MeV/c cut is made after the corrections so that the number of events, hence the NDF, depends somewhat on the corrections applied.

Examining Table 7.2 shows that the size of a correction does not depend on if the other correction is made or not. All confidence levels are in the range 10% to 15% (based on the χ^2/NDF), so the quality of the fit does not depend on if a correction is made or not. Based on this test it is concluded that the corrections may be calculated separately, as was done. The motivation for the cut at 50 MeV/c in the 0° data was a compromise between the data sample size and the desire to have small Coulomb corrections, which

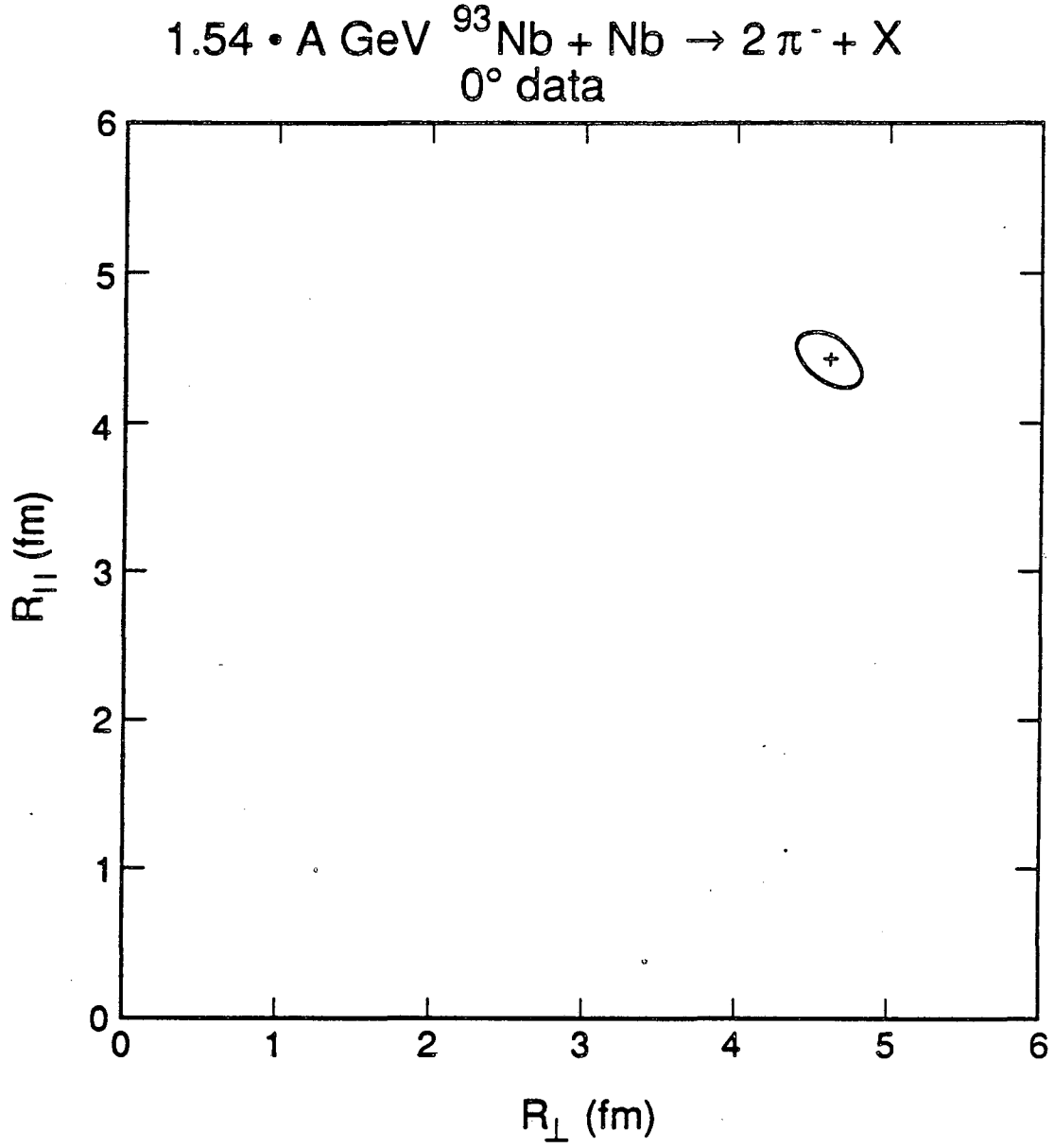

Figure 7.13: The 1σ confidence contour for the 0° Nb cut data — $R_{||}$ vs. $R_\perp$ plane.

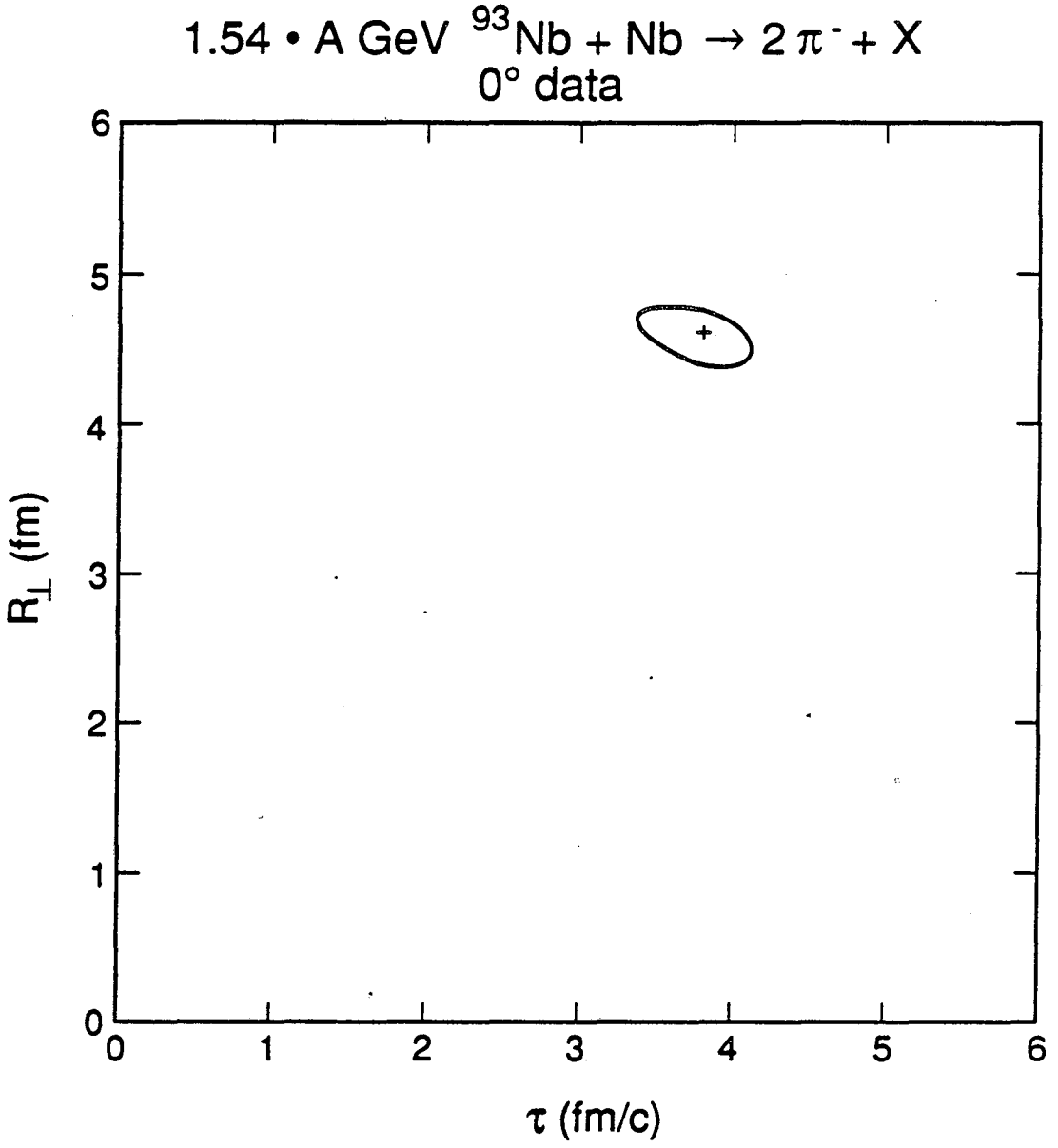

Figure 7.14: The 1σ confidence contour for the 0° Nb cut data — $R_\perp$ vs. τ plane.

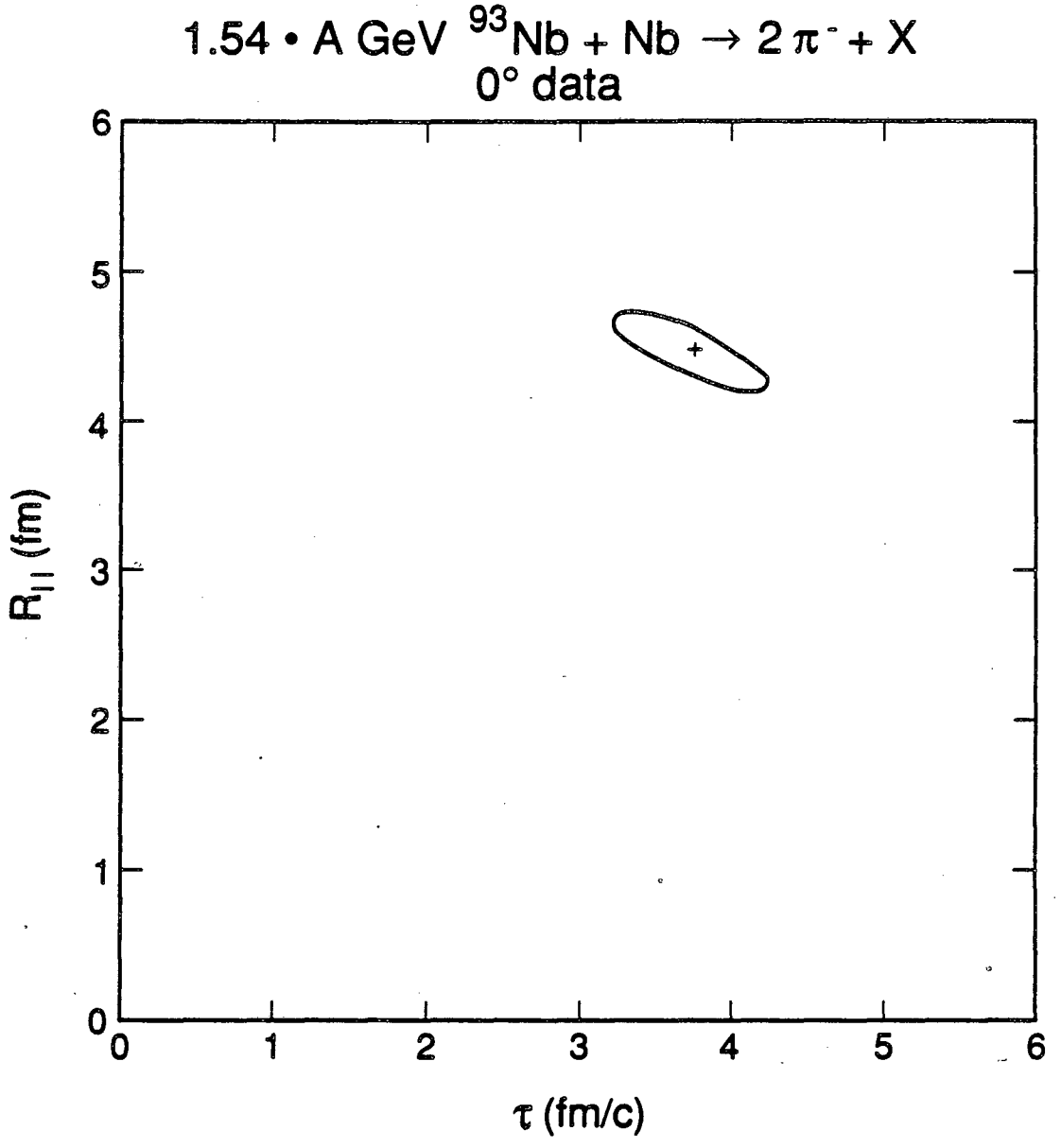

Figure 7.15: The 1σ confidence contour for the 0° Nb cut data — $R_{||}$ vs. τ plane.

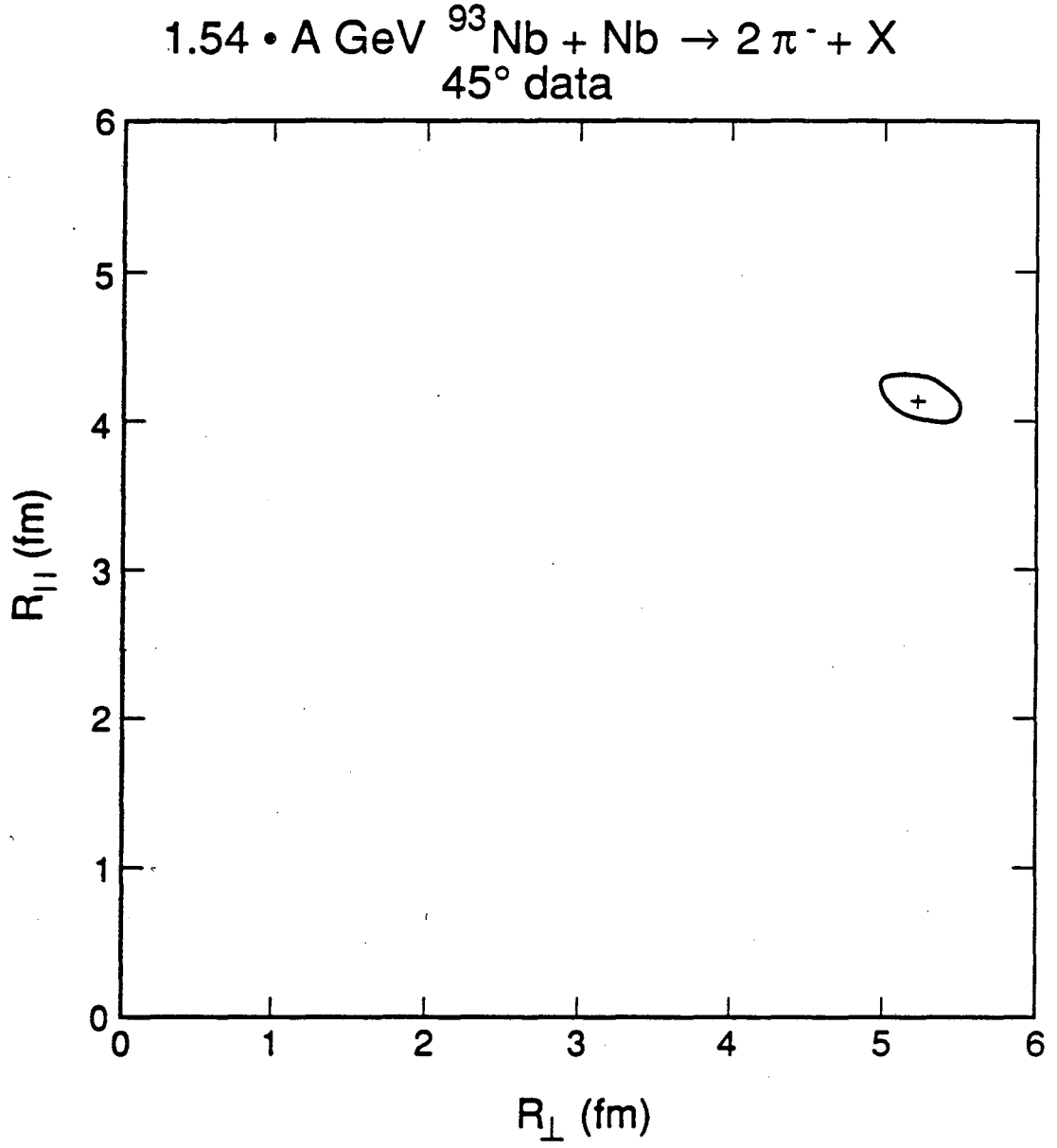

Figure 7.16: The 1σ confidence contour for the 45° Nb cut data — $R_{||}$ vs. $R_{\perp}$ plane.

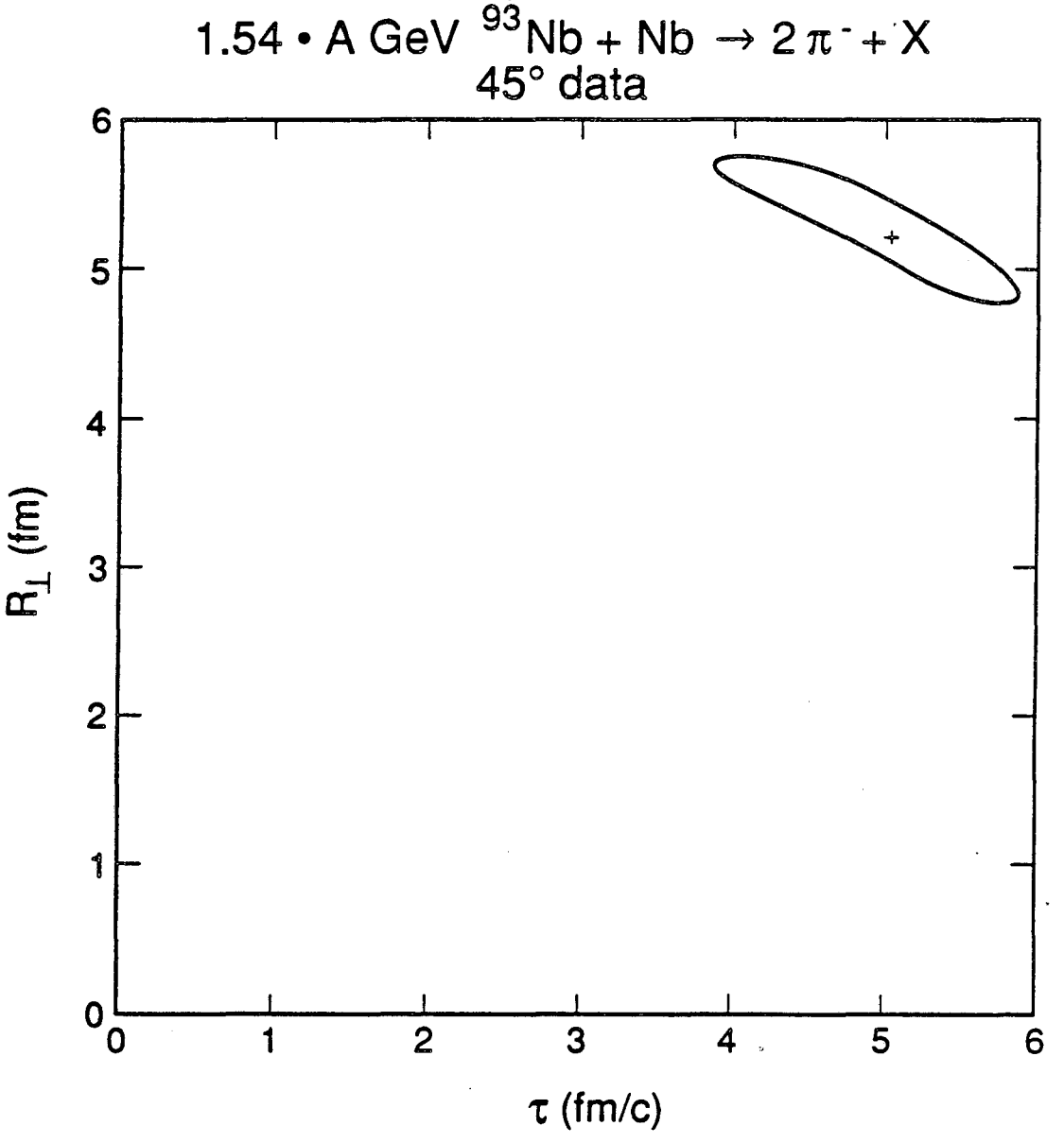

Figure 7.17: The 1σ confidence contour for the 45° Nb cut data — $R_\perp$ vs. τ plane.

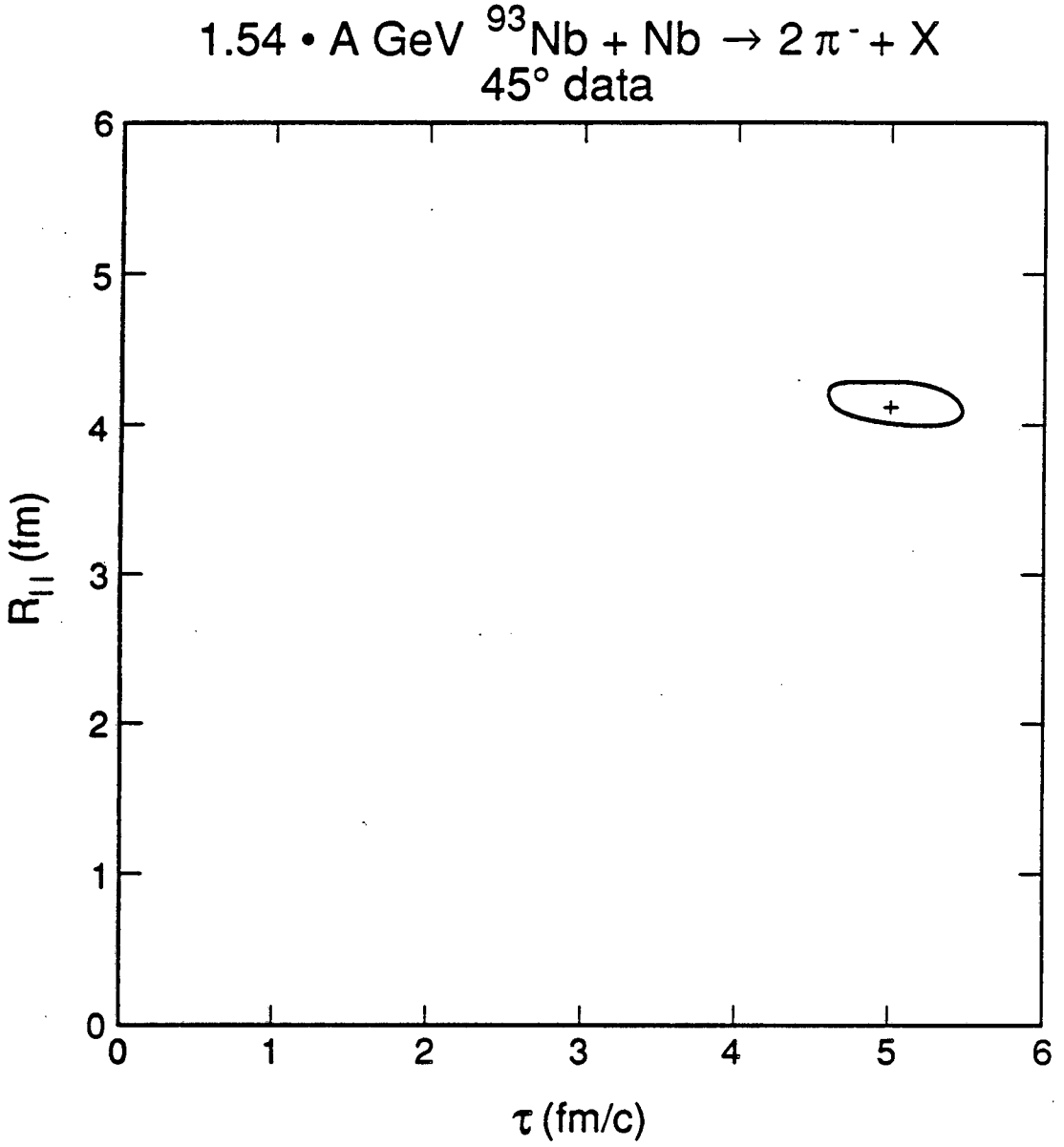

Figure 7.18: The 1σ confidence contour for the 45° Nb cut data — $R_{||}$ vs. τ plane.

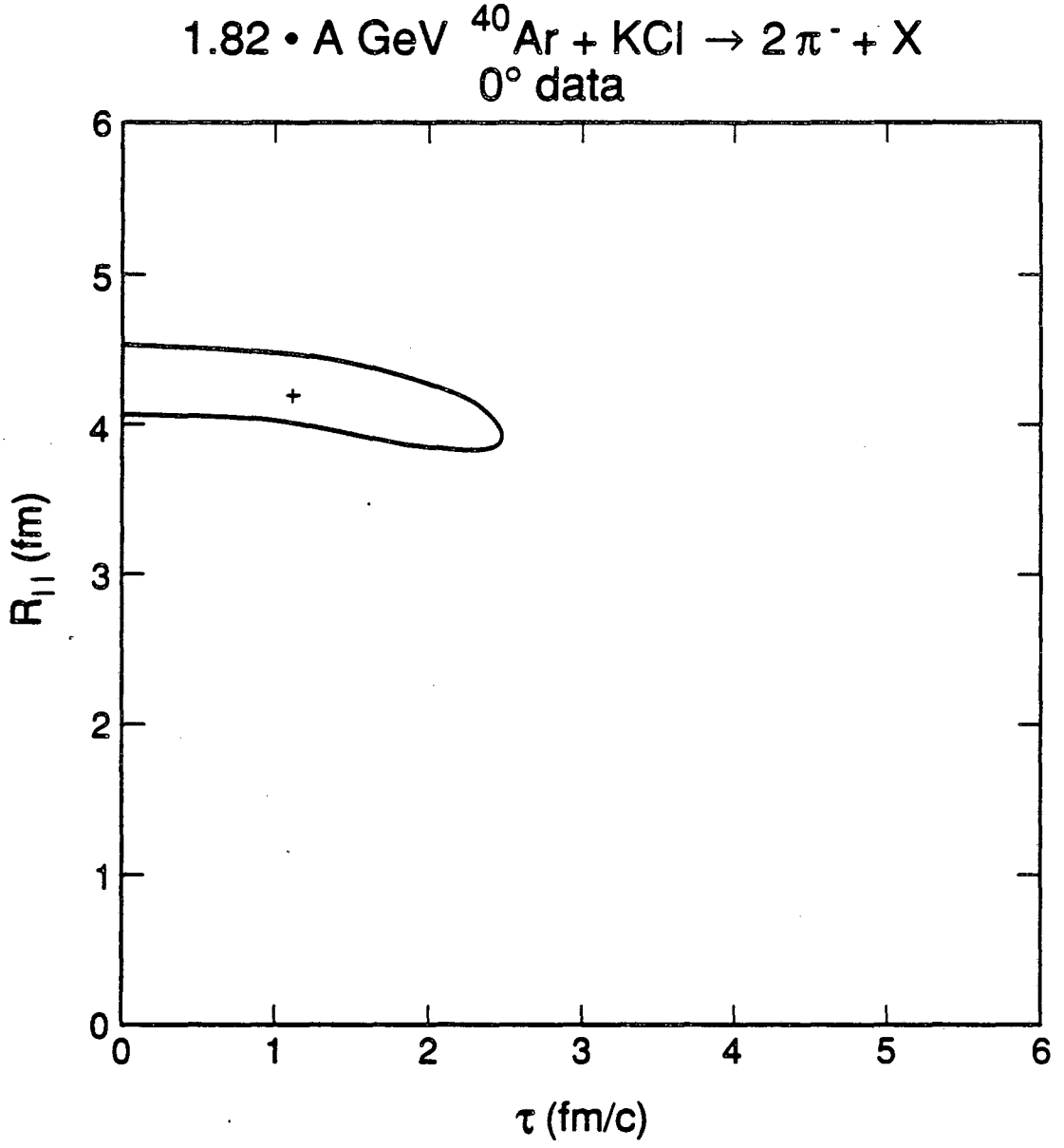

Figure 7.19: The 1σ confidence contour for the 0° Ar least cut data — $R_{||}$ vs. τ plane.

	Fe, 0° data, $\|\vec{p}_{\rm proj}\| > 50$ MeV/c ($\sim 10,000$ events)			
Coulomb correction	In	In	Out	Out
Gamow correction	In	Out	In	Out
$R_\perp$(fm)	4.6 ± 0.2	4.3 ± 0.3	5.9 ± 0.5	5.6 ± 0.6
$R_\parallel$(fm)	$1.5^{+0.7}_{-1.5}$	$0.4^{+1.2}_{-0.4}$	$2.9^{+0.5}_{-1.1}$	$2.2^{+0.8}_{-1.6}$
τ(fm/c)	3.8 ± 0.7	4.2 ± 0.4	3.7 ± 1.0	4.2 ± 1.1
λ	0.78 ± 0.04	0.65 ± 0.06	0.92 ± 0.08	0.77 ± 0.07
χ^2/NDF	451/421	451/421	314/286	314/285
$\chi^2_{\rm PML}$/NDF	2046/1942	2044/1942	1278/1247	1280/1247

Table 7.2: Parameters as a function of the corrections applied, for a subset of the 0° Fe data. Only statistical uncertainties are shown.

would allow the corrections to be calculated separately.

To further examine the Coulomb corrections, a π^+ pair data sample was taken in the 0° Nb configuration. In the π^+ data sample protons were rejected if the pulse height in the A and the B counters were both above the cuts for these counters, and the time–of–flight is above the cut for this AB pair. The proton contamination after the cuts was estimated by comparing the momentum spectrum without the cuts to the spectrum with the cuts (to determine where the protons were in that spectrum), and comparing the spectrum with cuts to the spectrum of the π^- data analyzed with the same cuts (to determine the spectrum shape in the absence of the proton contamination). The proton contamination is estimated to be 25%. The small data sample size did not allow further reductions in the proton contamination. The agreement between the π^- and the π^+ data is at the 1σ level for $R_\perp$, τ, λ and at the 3σ level for $R_\parallel$. While this shows acceptable agreement, the uncertainties in the π^+ parameters are large, due to the small data sample size. The parameters (for both the π^+ and π^-) are given in Table 7.7.

7.6 Systematic Uncertainty

The major source for the systematic uncertainty is believed to be the uncertainty in the residual correlation calculation. The source of this effect is that the correlation function

used as input for the residual correlation calculation is taken from the measurements and is, therefore, uncertain. The systematic uncertainty from this effect was studied for both acceptances. The statistical and systematic uncertainties for the 0° Ar (least cut) and the 0° Fe (both cuts) data sets are shown in Table 7.3. Unless noted, in the remaining tables the uncertainties shown are the total uncertainties. Note that this systematic uncertainty has the feature that improved statistics will decrease the systematic uncertainty by decreasing the uncertainty in the measured correlation function. The uncertainties in λ due to particle contamination corrections are not included since λ was not corrected for the particle contamination.

	Ar, 0° data	Fe, 0° data	
	$\|\vec{p}_{\rm proj}\| > 50$ MeV/c	$\|\vec{p}_{\rm proj}\| > 50$ MeV/c	$\|\vec{p}_{\rm proj}\| > 100$ MeV/c
$R_\perp$(fm)	$4.8 \pm 0.3 \pm 0.07$	$4.8 \pm 0.2 \pm 0.05$	$4.7 \pm 0.3 \pm 0.08$
$R_{\|\|}$(fm)	$4.2 \pm 0.4 \pm 0.2$	$2.7 \pm 0.3 \pm 0.1$	$2.1 \pm 0.5 \pm 0.16$
τ(fm/c)	$1.1^{+1.4}_{-1.1} \pm 0.4$	$2.7 \pm 0.6 \pm 0.2$	$3.5 \pm 0.6 \pm 0.3$
λ	$0.81 \pm 0.05 \pm 0.03$	$0.88 \pm 0.03 \pm 0.015$	$0.75 \pm 0.05 \pm 0.02$
χ^2/NDF	581/537	939/729	470/395
$\chi^2_{\rm PML}$/NDF	2979/2590	2938/2420	1476/1300
Events	12900	32000	11200

Table 7.3: Statistical uncertainties followed by estimated systematic uncertainties for the Ar and Fe 0° data sets.

7.7 The Parameters

The projections and the confidence contours show that the data are well described by the correlation function chosen for the fits, so the remaining fits will not show the projections or the confidence contour plots.

Table 7.4 and Figure 7.20 present the data for the 45° set up where $R_\perp \equiv R_{||}$ has been forced in the codes so that this data is easily compared to earlier data. Note that if $R_\perp = R_{||} = R$, then

$$q_\perp^2 R_\perp^2 + q_{||}^2 R_{||}^2 + q_0^2 \tau^2 = \vec{q}^{\,2} R^2 + q_0^2 \tau^2 \tag{7.4}$$

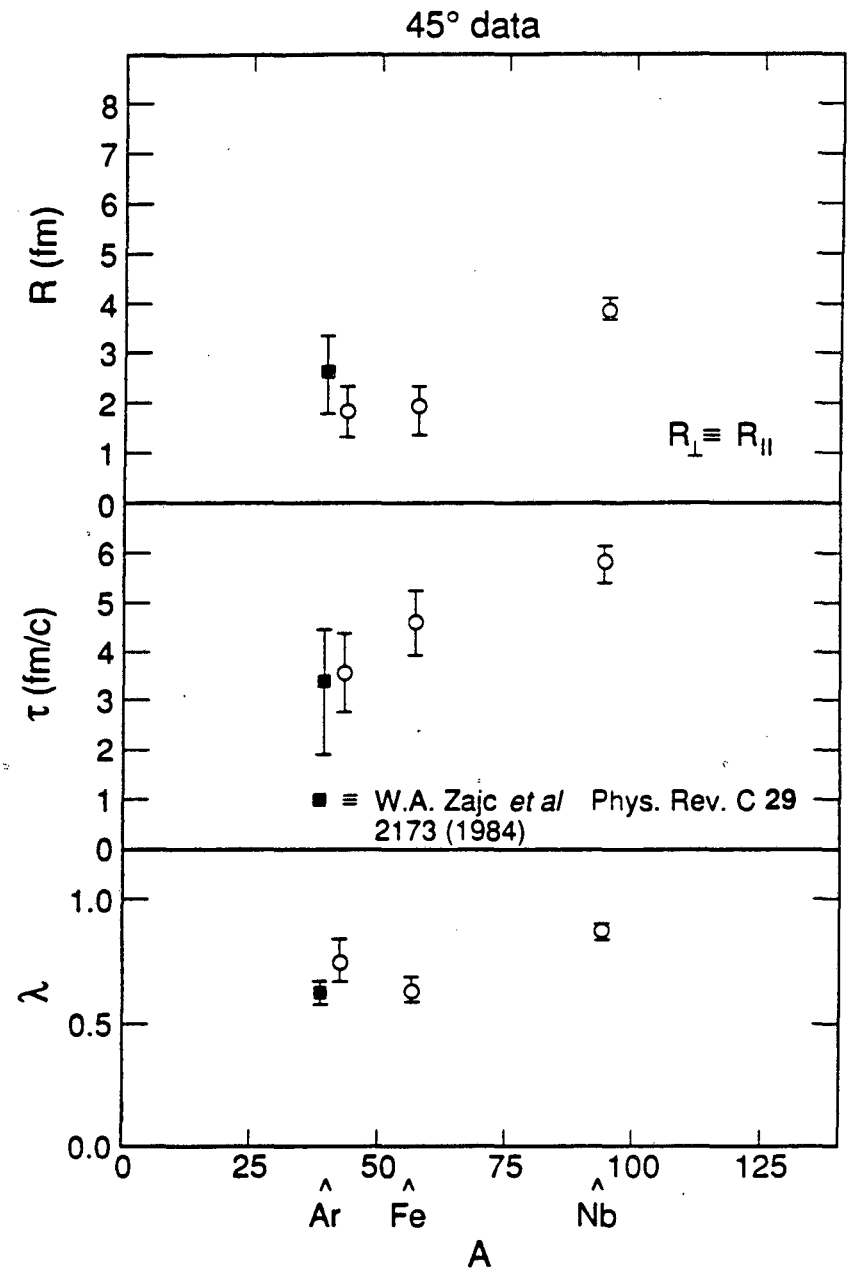

Figure 7.20: Parameters as a function of A for the 45° data with $R_\perp \equiv R_{||}$. The data points for Ar have been displaced for clarity. Only statistical uncertainties are shown.

	45° data, single radius parameter fits			
Projectile	Ar (Zajc)	Ar	Fe	Nb
R(fm)	$2.77^{+0.6}_{-0.9}$	1.9 ± 0.5	2.0 ± 0.5	3.9 ± 0.1
τ(fm/c)	$3.44^{+1.1}_{-1.5}$	3.6 ± 0.8	4.7 ± 0.5	5.8 ± 0.4
λ	0.63 ± 0.04	0.75 ± 0.1	0.65 ± 0.05	0.88 ± 0.03
χ^2/NDF	80.3/96	145/160	389/408	846/795
$\chi^2_{\rm PML}$/NDF	211.2/158	1716/1663	2195/1927	2607/2098
Events	6700	3300	8400	39100

Table 7.4: Parameters as a function of the projectile, for the 45° data. The data marked Ar (Zajc) are the Ar π^- data of W. A. Zajc *et al.*[1]; the remaining data are this work. Only statistical uncertainties are shown.

and these fits are equivalent to the single radius parameters fits used earlier[1, 23, 24, 25, 28]. The fits are labeled by the projectile used, where the beam energies and the targets are as listed in Tables 4.1 and 4.2. The column headed Ar (Zajc) is data from Zajc *et al.*[1]. The fitting method used in [1] is slightly different in that the data were histogrammed as a function of $q = |\vec{q}|$ and q_0, so that the assumption that $R_\perp = R_{||}$ could not be tested. For this reason the NDF is quite different from the values in this work. Note that the data from this work agrees with the data from the the previous work at the 1σ level.

Table 7.5 and Figure 7.21 present the data for the 45° data where $R_\perp$ and $R_{||}$ are allowed to vary separately. These data have a cut imposed on the magnitude of the center of mass momentum requiring both pions to have momenta greater than the lower limit of the acceptance of the spectrometer. This cut was imposed to remove improperly reconstructed tracks. The value of this cut was 90 MeV/c for the Ar data, 100 MeV/c for the Fe data and for the Nb data the cut was ignored since no data would have been cut. Since this cut removes no real data, these data are labelled "uncut".

Table 7.6 and Figure 7.22 present the data for the 45° set up as above, however the cut on the center of mass momenta was increased to $|\vec{p}_{\rm cm}| > 150$ MeV/c to search for effects that depend on the pion momentum. One such effect would be a pion source size depending on the pion momentum, which would be the result of an expanding pion

	45° data, uncut		
Projectile	Ar	Fe	Nb
$R_\perp$(fm)	4.5 ± 1.0	4.0 ± 0.65	4.8 ± 0.55
$R_\parallel$(fm)	1.0 ± 1.0	$1.5^{+0.55}_{-0.9}$	3.8 ± 0.2
τ(fm/c)	$0.0^{+2.3}_{-0.0}$	1.7 ± 1.7	4.8 ± 1.0
λ	0.72 ± 0.10	0.66 ± 0.06	0.89 ± 0.035
χ^2/NDF	138/156	381/403	846/795
$\chi^2_{\rm PML}$/NDF	1702/1662	2194/1925	2612/2098
Events	3300	8400	39100

Table 7.5: Parameters as a function of the projectile, for the 45° uncut data.

	45° data, $\lvert\vec{p}_{\rm cm}\rvert > 150$ MeV/c	
Projectile	Fe	Nb
$R_\perp$(fm)	$4.3^{+0.6}_{-0.8}$	5.2 ± 0.55
$R_\parallel$(fm)	$1.5^{+0.6}_{-1.0}$	4.1 ± 0.2
τ(fm/c)	$0.1^{+2.8}_{-0.1}$	5.0 ± 1.1
λ	0.58 ± 0.07	0.87 ± 0.035
χ^2/NDF	362/345	742/719
$\chi^2_{\rm PML}$/NDF	2167/1897	2477/1945
Events	6900	34600

Table 7.6: Parameters as a function of the projectile, for the 45° cut data. There is not enough data in the Ar sample to fit the data with the cut.

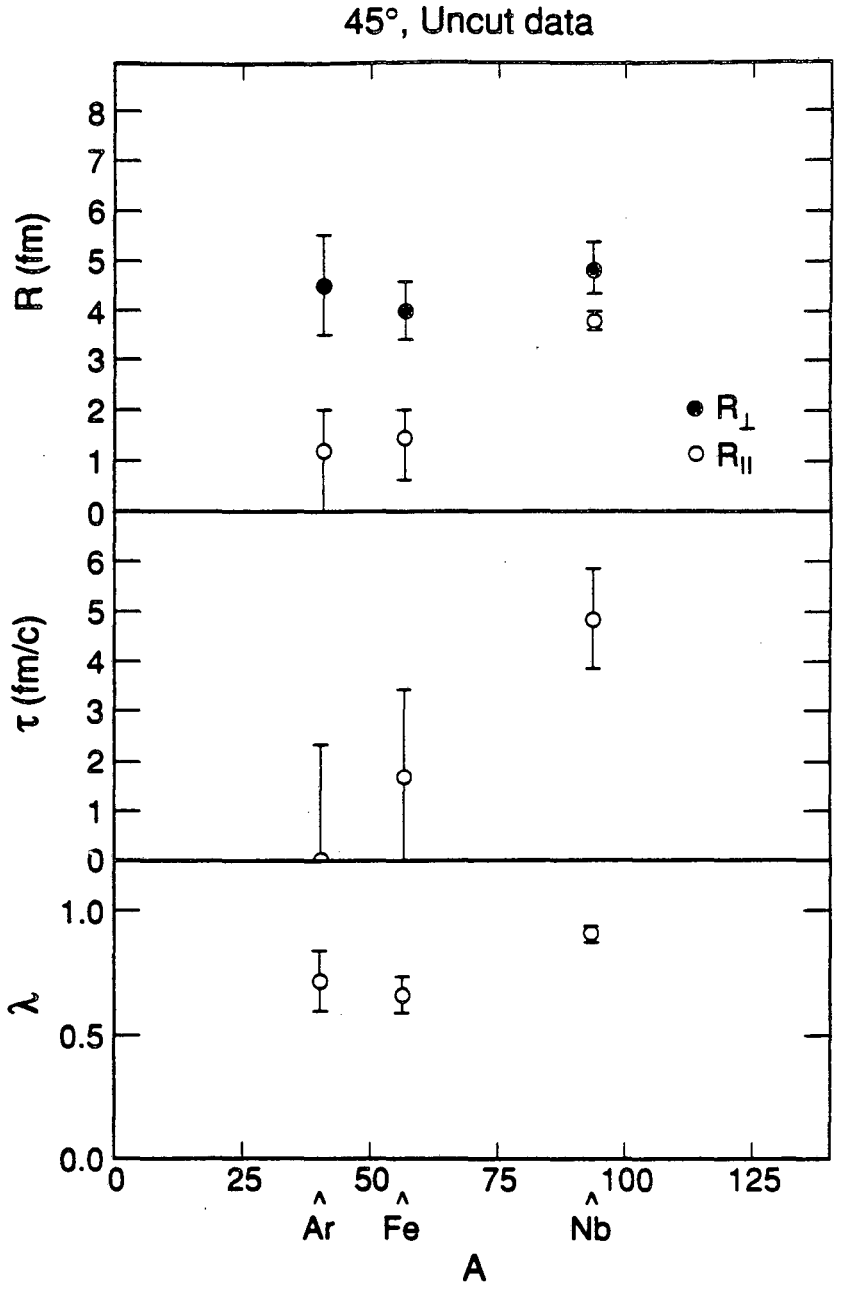

Figure 7.21: Parameters as a function of A for the 45° uncut data.

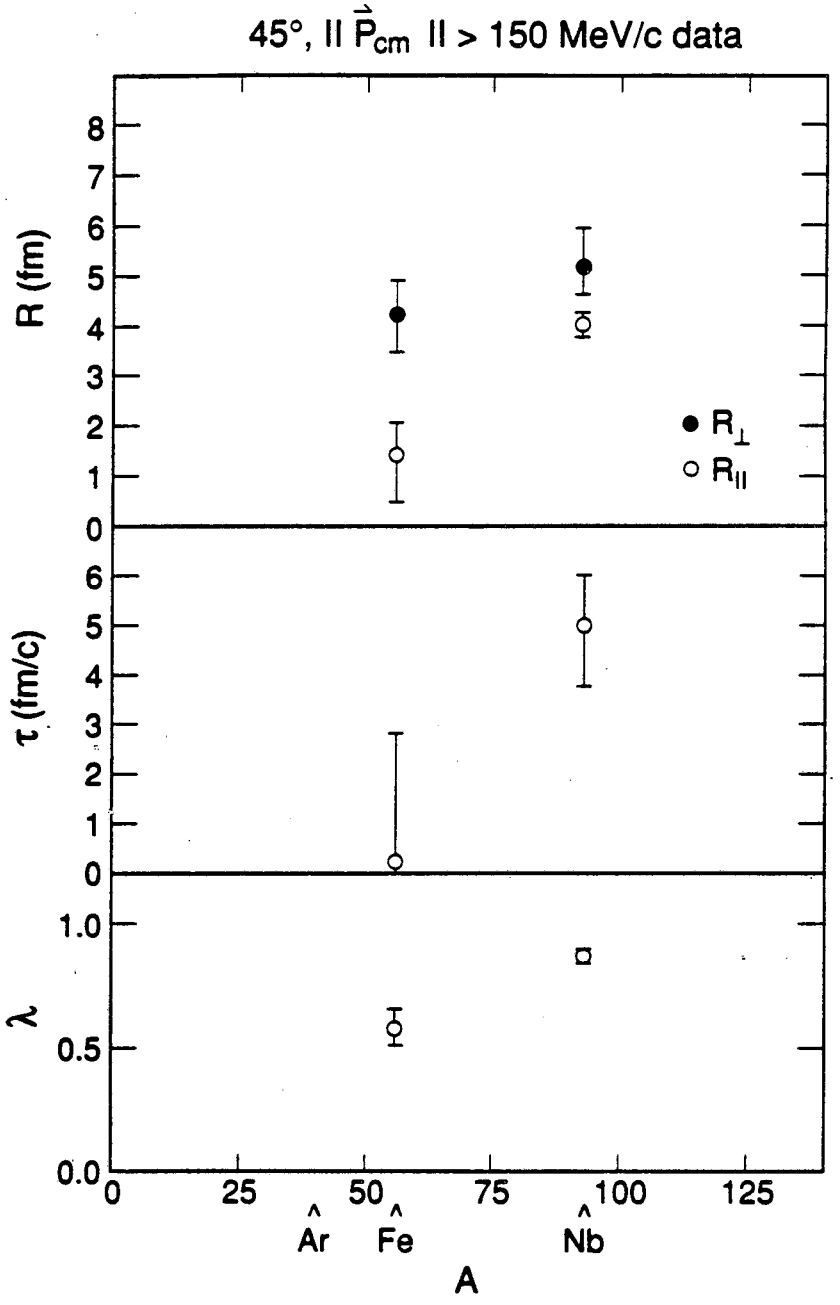

Figure 7.22: Parameters as a function of A for the 45° cut data.

source (see Section 3.3 and [36]). Examining the corresponding entries in Tables 7.5 and 7.6 shows that, within the uncertainties, there is no dependence on the momentum cut. The Ar data sample was smaller than desired and there was not enough data to fit a cut sample.

	0° data, $\|\vec{p}_{\rm proj}\| > 50$ MeV/c			
Projectile	Ar	Fe	Nb (π^-)	Nb (π^+)
$R_\perp$(fm)	4.8 ± 0.3	4.8 ± 0.2	5.1 ± 0.2	5.3 ± 1.0
$R_{\|\|}$(fm)	4.2 ± 0.4	2.7 ± 0.3	4.4 ± 0.3	7.4 ± 1.2
τ(fm/c)	$1.1^{+1.4}_{-1.1}$	2.7 ± 0.6	3.9 ± 0.4	$0.0^{+3.6}_{-0.0}$
λ	0.81 ± 0.06	0.88 ± 0.03	1.11 ± 0.03	1.0 ± 0.17
χ^2/NDF	581/537	939/729	1144/1087	69/86
$\chi^2_{\rm PML}$/NDF	2979/2590	2938/2420	3776/3235	736/753
Events	12900	3200	49400	1700

Table 7.7: Parameters as a function of the projectile, for the 0° least cut data.

Table 7.7 and Figure 7.23 present data for the 0° set up with $|\vec{p}_{\rm proj}| > 50$ MeV/c. The Nb set up included both π^- and π^+ data, motivated by a desire to verify the Coulomb correction calculations as mentioned in Section 7.5.

Table 7.8 and Figure 7.24 present data for the 0° set up with $|\vec{p}_{\rm proj}| > 100$ MeV/c. The larger value for the cut was motivated by a desire to check for effects that depend on the pion momentum relative to the nearest nuclear matter, the projectile fragment. This would include effects from the Coulomb correction. Note that for the Fe and Nb data the agreement between the two data sets is good. For the Ar data the higher momentum cut data are about 2σ smaller in all parameters.

7.8 Discussion

The parameters show the pion source to be oblate ($R_\perp > R_{||}$) or spherical. Using a 4π streamer chamber, Beavis *et al.* have found spherical sources for 1.5 · A GeV Ar + KCl with parameters[23] of $R_\perp = 5.0 \pm 0.5$ fm and $R_{||} = 5.0 \pm 1.5$ fm, and for Ar + Pb with parameters[25] of $R_\perp = 5.16 \pm 0.50$ fm, $R_{||} = 5.76 \pm 0.54$ fm and $\lambda = 0.98 \pm 0.14$. The

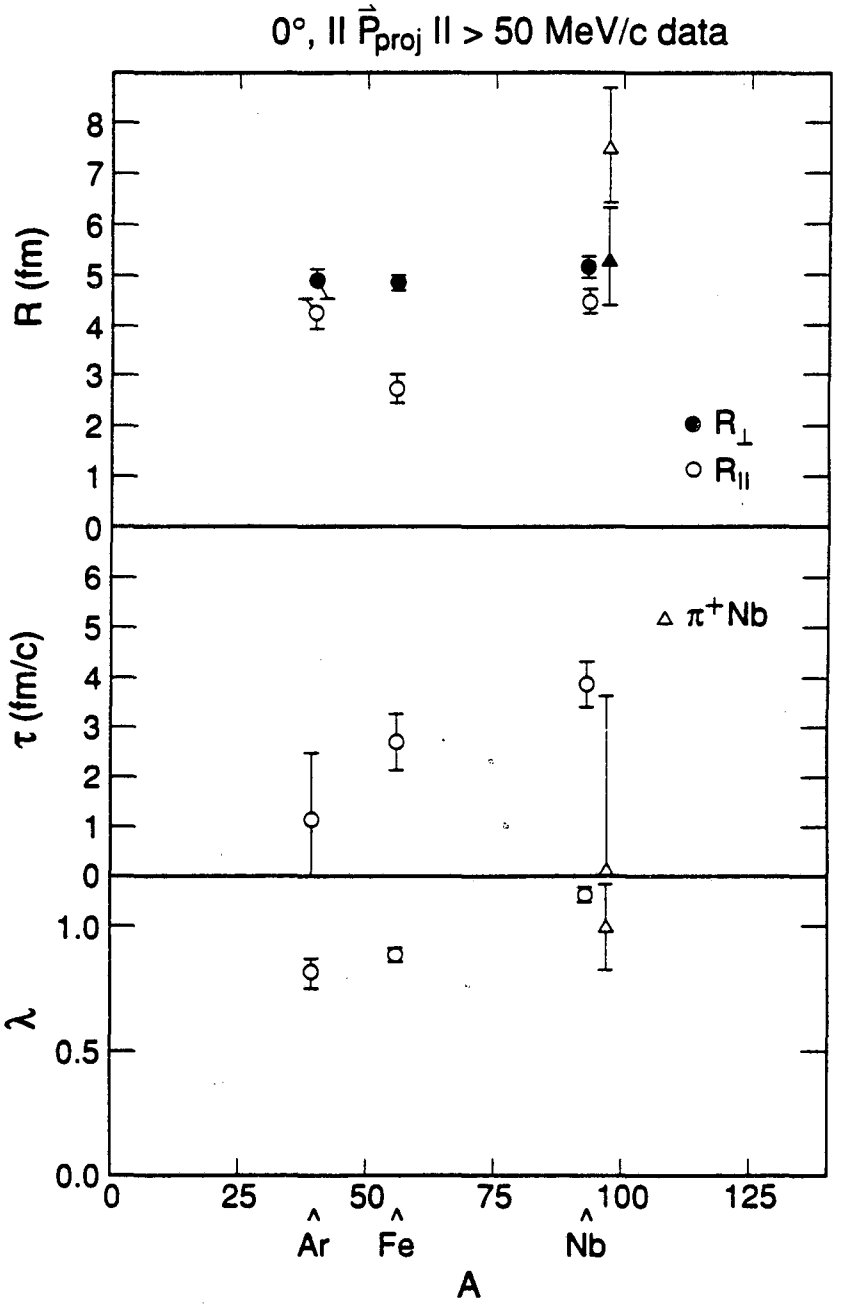

Figure 7.23: Parameters as a function of A for the 0° least cut data. The data points for Nb have been displaced for clarity.

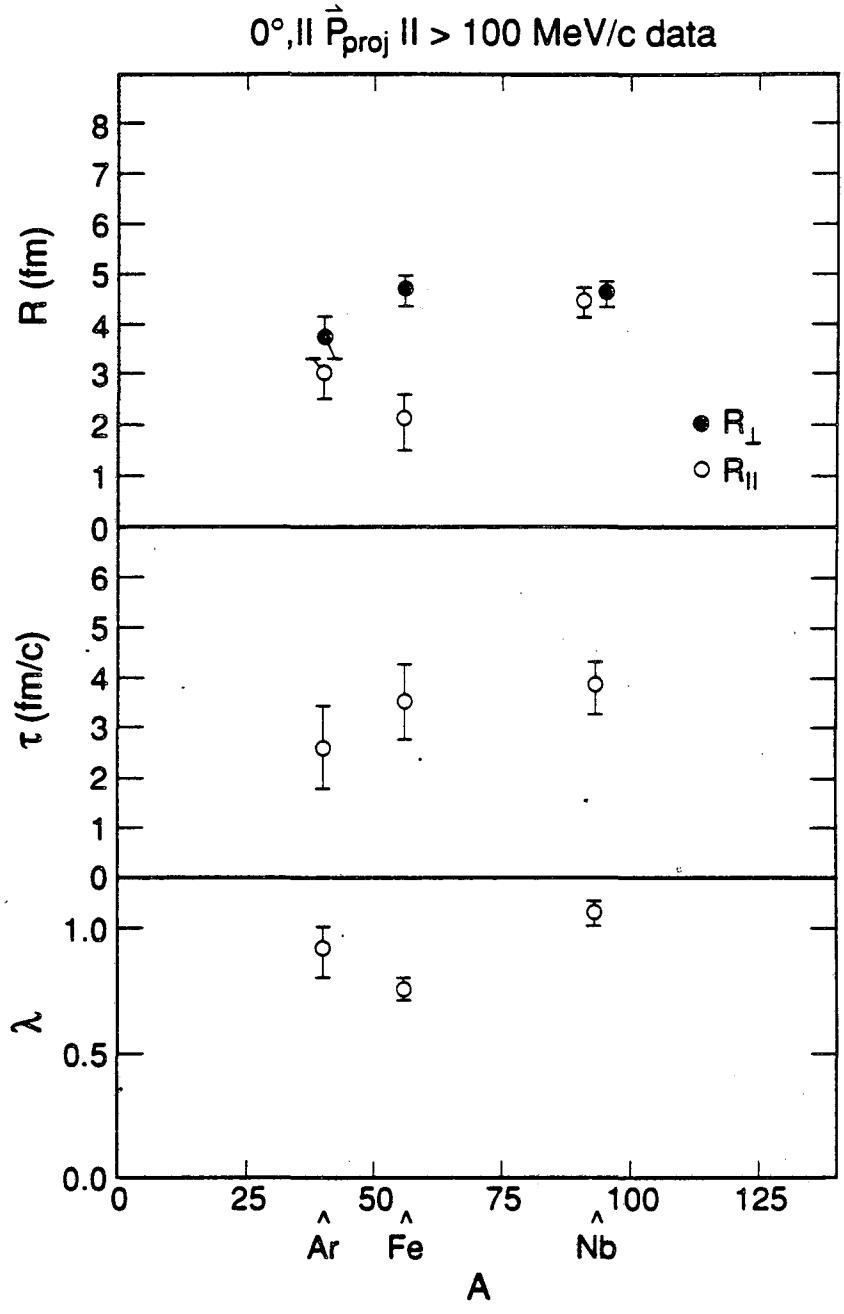

Figure 7.24: Parameters as a function of A for the 0° cut data. The data points for the Nb radii have been displaced for clarity.

	0° data, $\|\vec{p}_{\rm proj}\| > 100$ MeV/c		
Projectile	Ar	Fe	Nb
$R_\perp$(fm)	3.7 ± 0.4	4.7 ± 0.3	4.6 ± 0.3
$R_\parallel$(fm)	3.0 ± 0.5	2.1 ± 0.5	4.5 ± 0.3
τ(fm/c)	2.7 ± 0.8	3.5 ± 0.7	3.8 ± 0.5
λ	0.9 ± 0.10	0.75 ± 0.05	1.05 ± 0.04
χ^2/NDF	324/318	470/395	665/630
$\chi^2_{\rm PML}$/NDF	2147/1936	1476/1300	2386/2091
Events	6800	11200	21400

Table 7.8: Parameters as a function of the projectile, for the 0° cut data.

Ar + KCl parameters are within 1σ of this thesis, so the oblate shape obtained here is within the uncertainties of the spherical shape.

At the Intersecting Storage Rings (in CERN), Åkesson *et al.*[51] have measured a prolate source in p + p collisions at $\sqrt{s} = 63$ GeV, and spherical source in He + He collisions at $\sqrt{s} = 126$ GeV. Their data analysis technique is different, because they measure the pion source size perpendicular to the average of the pions' momenta, and then cut on the direction of the pions' momenta. Their source sizes (multiplied by $\sqrt{2/3}$ to convert to the parametrization used in this thesis) are $R \simeq 1.4 \pm 0.2$ for p + p and $R \simeq 1.2 \pm 0.1$ for He + He.

Using the Plastic ball at the Bevalac, Bock *et al.*[28] found, for Nb + Nb at $650 \cdot$ A MeV, $R = 3.4 \pm 0.4$ fm (with τ fixed at 0 fm/c and χ^2/NDF = 1.5) a value 1.25σ from the value in this work. However, the single radius parameter Ar + KCl fit of Beavis *et al.*[23, 24] gives $R = 4.7 \pm 0.5$ fm, $\tau = 4.2^{+1.8}_{-4.2}$ and $\lambda = 1.2 \pm 0.2$ (the different beam energy is the reason this fit is not included in Table 7.4). There is significant disagreement between these numbers and those of Zajc *et al.*[1] and this work.

The parameters for a given acceptance (0° or 45°) agree, within the uncertainties, for the lower momentum cut and the higher momentum cut. Therefore the data do not show any evidence for possible collective expansion effects[36]. Beavis *et al.*[25] have also searched for collective expansion effects using cuts on the average of the pions' momenta, but the size of their data sample did not allow any definitive conclusions. Brock *et al.*[28]

analyzed their data for variations in the source size as a function of the pions' momenta, but observed only changes in the radius parameter for their Nb data at the 1σ level, again not showing any evidence for expansion.

Comparing the 45° data and the 0° least cut ($|\vec{p}_{\rm proj}| > 50$ MeV/c) data shows the pion source is more spherical for the 0° data. The $R_\perp$ parameter for one angular acceptance agrees, within the uncertainty, with $R_\perp$ for the other acceptance (comparing system by system), so this effect is due to $R_{||}$ being consistently smaller in the 45° acceptance.

Considering the parameters as a function of A, for both acceptances, $R_\perp$ shows only a weak dependence on A, increasing slightly. In fact, within the uncertainties, $R_\perp$ could be independent of A. The $R_{||}$ parameter depends more strongly on A than $R_\perp$. In the 45° acceptance the source is noticeably oblate for the light system, becoming less so for the heavier system. In the 0° acceptance the source shape is slightly oblate, becoming spherical. The τ parameter increases with A in the 45° acceptance (although the uncertainties are large due to the small sample sizes), and in the 0° acceptance this effect is not as clear.

The λ parameter is less than 1 for the 45° acceptance, for all systems, with a slight increase with A. The 0° acceptance data show similar behavior, but the values are slightly larger, being just below 1 for Ar and just above 1 for Nb.

Comparisons of Tables 7.4 and 7.5 show that restricting the source shape to spherical leaves λ unchanged and increases the extracted τ by more than 1σ. Since the same data were used in both fits (for a given system), this effect is systematic, not statistical. Future experiments will have to test the assumption that $R_\perp = R_{||}$, since it is clear that in this experiment the assumption changes the values of parameters other than R.

Chapter 8

Conclusions and Future Work

8.1 Conclusions

The method of pion–pion interferometry was used to measure the pion source parameters for three nuclear species, using two acceptances. The methods and computer codes used in this work have been verified, by Monte Carlo simulations, to give parameters that are within the statistical uncertainties of the values used as input for the Monte Carlo simulation.

The large data samples present in this experiment have allowed the determination of the source shape (that is, have allowed relaxing the assumption that the source is spherical). In addition, the lifetime of the source was measured and, in the larger data sets, is constrained to be non–zero (this has not always been the case in correlation experiments).

Figure 8.1 shows a plot of data inspired by a review article by Bartke[53]. This plot shows the pion source size parameter R, as a function of the atomic number of the projectile (A_p) to the one–third power. This plot contains data from a range of energies, impact parameters, and asymmetries of the projectile and target (although the projectile was always lighter than the target). The projectiles, targets, source parameters and the sources of the data are listed in Table 8.1. As in the article, our radius parameters have been multiplied by $\sqrt{3/2}$ to give RMS radius parameters. Note that the results of this measurement of the radius parameter are generally smaller than the prior measurements and show some increase with $A_p^{1/3}$. This plot allows the comparison of some of the data of

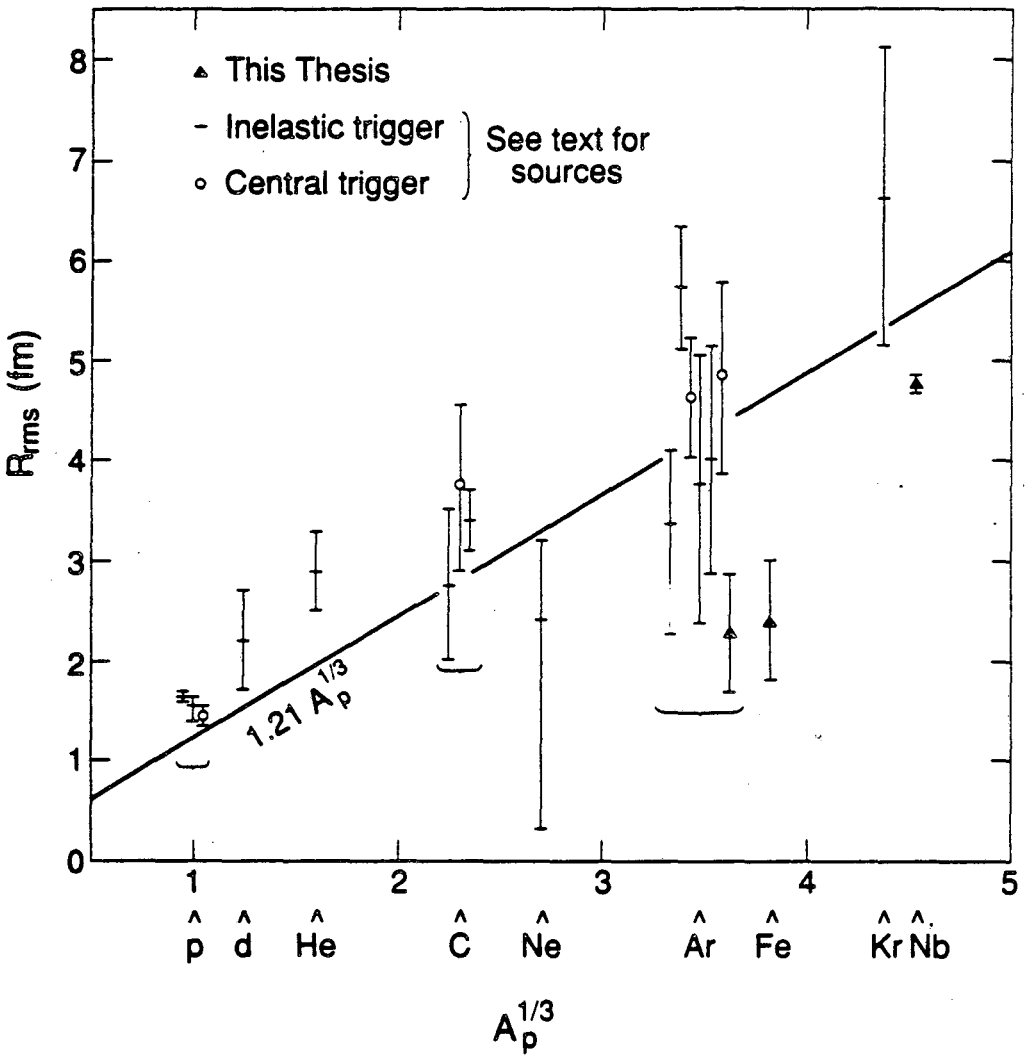

Figure 8.1: Pion source parameters as a function of $A_p^{1/3}$, where A_p is the atomic number of the projectile. The data are from the sources listed in Table 8.1. The data points for some projectiles have been displaced for clarity.

	A_p	A_t	E/A GeV	$R_{\rm rms}$	Reference
	p	H	200	1.66 ± 0.04	[54]
	p	Xe	200	1.53 ± 0.13	[54]
*	p	Xe	200	1.45 ± 0.11	[54]
	d	Ta	3.4	2.20 ± 0.50	[55]
	He	Ta	3.4	2.90 ± 0.40	[55]
	C	C	3.4	2.75 ± 0.73	[56]
*	C	C	3.4	3.76 ± 0.88	[56]
	C	Ta	3.4	3.40 ± 0.30	[55]
	Ne	NaF	1.8	$2.24^{+0.98}_{-1.96}$	[1]
	Ar	KCl	1.8	$3.39^{+0.73}_{-1.10}$	[1]
	Ar	KCl	1.5	5.76 ± 0.61	[24]
*	Ar	KCl	1.2	4.65 ± 0.61	[24]
	Ar	BaI_2	1.8	3.75 ± 1.35	[22]
	Ar	Pb_3O_4	1.8	4.04 ± 1.14	[22]
*	Ar	Pb_3O_4	1.8	4.87 ± 0.96	[22]
	Ar	KCl	1.8	2.3 ± 0.6	this thesis
	Fe	Fe	1.7	2.5 ± 0.6	this thesis
	Kr	RbBr	1.2	6.61 ± 1.47	[57]
	Nb	Nb	1.5	4.8 ± 0.1	this thesis

Table 8.1: Pion source parameters for different projectile target combinations. The symbols A_p and A_t are the projectile and target atomic numbers, respectively. The data marked with an asterisk were biased by towards central collisions above whatever biasing occurs due to the spectrometer's acceptance.

this thesis to a large sample of pion–pion correlation data. One can see the improvement in the accuracy of the measurement of the pion source radius parameter for heavy ions in the more recent measurements.

At this point one would, of course, like to point to several theory predictions and pick the one that most closely agrees with the experimental data. Usually the situation is not so simple and, unfortunately, this experiment is no exception. The existing theories are computer Monte Carlo simulations and require too much computer time for one person to generate the required predictions.

There are two sets of data that can be compared with theory, those of the Ar single radius parameter fits and the Fe two radius parameter fits. The predictions are taken from the work of Humanic and made using the program CASCADE.[1]

	Ar 45° data, single radius parameter fits		
	Experiment (Zajc)	This Experiment	CASCADE
R(fm)	$2.77^{+0.6}_{-0.9}$	1.9 ± 0.5	3.58 ± 0.11
τ(fm/c)	$3.44^{+1.1}_{-1.5}$	3.6 ± 0.8	2.83 ± 0.43
λ	0.63 ± 0.04	0.75 ± 0.1	1.003 ± 0.045
χ^2/NDF	80.3/96	145/160	–
χ^2_{PML}/NDF	211.2/158	1716/1663	–
Events	6700	3300	–

Table 8.2: Comparison between experimental and CASCADE pion source parameters for the 45° data. The data marked (Zajc) are the Ar π^- data of Zajc *et al.*[1]; the remaining experimental data are this work. Only statistical uncertainties are shown.

The single radius parameter predictions[27] were generated for comparison to the data of Zajc *et al.*[1] and the data of Beavis *et al.*[23, 24]. Table 8.2 presents Humanic's predictions, the data of Zajc *et al.* and the data from this experiment (which are taken from Table 7.4). The measured R is much smaller than the prediction, and τ is larger. It is unclear if τ being larger is a fundamental effect, or an artifact of fitting a restricted form of the correlation function. As mentioned in Section 7.8, restricting the form of the fitted correlation function to a single radius parameter causes τ to increase. The measured

[1] See [27] and references therein.

values of λ are smaller than the predicted values.

The Fe data and predictions have been published earlier[32]. Repeated here in Table 8.3 are the predictions and the experimental results from Tables 7.5, 7.6, 7.7, 7.8. The predicted numbers are generally larger than the measured values. This would indicate that a nuclear collision is more than just the superposition of the 2–body interactions, as has been believed for some time.[2]

In the absence of theoretical data, one can try to predict what effects the modifications of the computer codes will have on the predictions made by the codes. The inclusion of nucleon–nucleon repulsion terms will make the interaction region larger, because the nucleons will resist compression. The repulsion will also cause energy to be stored as compressional energy and be unavailable for pion production. These two effects would lower the energy density available for pion production. Assuming that the energy density in the nuclear collision is near the pion production threshold, this would decrease the pion source size, since the energy density in the outer regions of the collision would drop below the production threshold. So if the nuclear repulsion effect is present in nuclear collisions, and if the energy density is near the pion production threshold, then the measured source should be smaller and longer lived than the CASCADE prediction. In Table 8.2 the measured sources are smaller and longer lived than the CASCADE predictions.

The repulsion term will expand the source perpendicularly to the beam axis, since the increased pressure will push matter out the sides of the interaction region, giving sources that are more oblate than the CASCADE predictions. In Table 8.3 it can be seen that the measured sources are more oblate than those predicted by CASCADE, The measured $R_\perp$ being equal to or slightly larger than the prediction, while the measured $R_{||}$ is smaller. Here, however, the measured lifetime is shorter than the CASCADE prediction.

Collective flow will, to some extent, cause the momentum distribution of the pions to peaked in the direction of the flow. This will cause the pion momenta to be correlated in addition to the Bose–Einstein symmetrization, and will cause the measured λ to be smaller than the CASCADE prediction. In Table 8.3 the measured value of λ is smaller than the predictions.

Based on these arguments, nucleon–nucleon repulsion effects will be needed to describe

[2]See, for example, [52] for an article concerned specifically with CASCADE.

	45°		45°	
	$\|\vec{p}_{cm}\| > 100$ MeV/c		$\|\vec{p}_{cm}\| > 150$ MeV/c	
	Experiment	CASCADE	Experiment	CASCADE
$R_\perp$(fm)	4.0 ± 0.65	4.2 ± 0.3	$4.3^{+0.6}_{-0.8}$	4.2 ± 0.2
$R_\parallel$(fm)	$1.5^{+0.55}_{-0.9}$	3.0 ± 0.2	$1.5^{+0.6}_{-1.0}$	2.9 ± 0.2
τ(fm/c)	1.7 ± 1.7	3.3 ± 0.6	$0.1^{+2.8}_{-0.1}$	3.2 ± 0.6
λ	0.66 ± 0.06	1.00 ± 0.02	0.58 ± 0.07	0.98 ± 0.02
χ^2/ NDF	381/403	1099/1082	362/345	1112/1039
χ^2_{PML}/NDF	2194/1925	1563/1691	2167/1897	1596/1708

	0°		0°	
	$\|\vec{p}_{proj}\| > 50$ MeV/c		$\|\vec{p}_{proj}\| > 100$ MeV/c	
	Experiment	CASCADE	Experiment	CASCADE
$R_\perp$(fm)	4.8 ± 0.2	4.0 ± 0.1	4.7 ± 0.3	4.4 ± 0.1
$R_\parallel$(fm)	2.7 ± 0.3	3.3 ± 0.1	2.1 ± 0.5	2.3 ± 0.1
τ(fm/c)	2.7 ± 0.6	4.3 ± 0.2	3.5 ± 0.7	4.4 ± 0.2
λ	0.88 ± 0.03	1.00 ± 0.02	0.75 ± 0.05	0.98 ± 0.02
χ^2/ NDF	939/729	1031/1061	470/395	374/376
χ^2_{PML}/NDF	2938/2420	1543/1693	1476/1300	498/555

Table 8.3: Comparison between experimental and CASCADE pion source parameters for the Fe data. The data marked $|\vec{p}_{cm}| > 100$ MeV/c are labeled "uncut" in Chapter 7, see Chapter 7. The uncertainties shown for the measured data are total. The uncertainties shown for CASCADE are statistical only.

the pion source size and shape and, therefore, the nuclear collision process. Theoretical comparisons should be made with the results of pion interferometric measurements to help determine if the repulsion terms are being incorporated into the theories correctly.

8.2 Future Work

The first question raised by this work is; How does the size of the source increase with atomic number? The measured source size for 0° Ar (with $|\vec{p}_{\rm proj}| > 50$ MeV/c) is $R_\perp = 4.8 \pm 0.3$ fm and $R_{||} = 4.2 \pm 0.4$ fm and the source size for p + p is ≈ 1.4 fm (corrected to the parameterization used in this thesis) and prolate[51]. Figure 8.1 would seem to indicate that the size increases smoothly, but at a rate slower than the projectile radius. However, the uncertainties in some of the measurements are large and there is the additional uncertainty over the assumption that the source size is dominated by the smaller of the two nuclei in the collision. Measurements (with equal mass target and projectile, to make the comparison easier) need to be made in the region of $A \approx 10$ and $A \approx 20$. Suitable choices for beams and targets are ^{11}B + B and ^{20}Ne + NaF.

Given that the p + p source is prolate, the Ar source is oblate, and the Nb source is nearly spherical a second question is; How does the shape of the source depend on the atomic number? For the lower atomic numbers, again, measurements need to be made in the region of $A \approx 10$ and $A \approx 20$, and an experiment using U + U would cover the entire range of particles that the Bevalac accelerator can accelerate (as well as the range of naturally occurring isotopes).

These experiments are possible to do with existing accelerators and detectors, and indeed, could be done with existing detectors at the Bevalac. Some lighter elements have been measured, but without sufficient statistics to permit a source shape analysis. The Crowe/Rasmussen Group at LBL has done an experiment using 1.22 · A GeV ^{139}La + La (that is under analysis) that may help to answer the question for high atomic numbers, but U + U will be needed to cover the highest atomic numbers possible.

In the farther future, using 4π detectors, it should be possible to measure all of the charged particles from the nuclear collision and determine the impact plane. One could then measure radius parameters in the impact plane and perpendicular to it. This would remove the necessity for averaging over the impact plane angle that is necessary when

comparing the current data to the theories. One could also measure these parameters as a function of the impact parameter, since in this type of experiment, the number of participant nucleons will be measured.

As higher energy machines come on line it will become less accurate to ignore the multiparticle correlations since the density of pions in phase–space will be high. The formalism will have to change from the current correlation function, which only considers two pions in the event, to perhaps something like speckle interferometry[12]. Theoretical analysis will be needed to determine how to analyze the data to extract the relevant parameters and to determine what the relevant parameters are.

Appendix A

The Monte Carlo Program

The performance of the spectrometer was simulated using Monte Carlo methods. The computer codes used to simulate this experiment fulfilled three roles. First, the Monte Carlo was used to provide the input data for the ERIKA fit that gives the track parameters as a function of the wire numbers in the track (see Section 5.6). Second, it was used to provide fake single track events to test the hit and track finding software, to measure the acceptance, and to measure the resolution (see Sections 4.2 and 5.3). Third, it was used to provide fake two track events with a known correlation function to test the correlation function fitting procedure and programs (this test included the entire data analysis stream). These data were also used to check the hit and track finding software when two tracks are present in the event (see Section 5.4). Many features of the Monte Carlo codes are common to the three roles and the same code, with switches, was used for all three roles.

The magnetic field map (in both magnets) was used to track the particles. The fields were interpolated to second order between the grid points and the particles' motion was described by fitting sections from circles for each path step (1 cm in the air). The separation between the sense planes in the wire chambers was simulated, as was the finite wire–chamber resolution, except for when producing ERIKA input data when increased accuracy was desired. Multiple scattering and energy loss are simulated using formulas from [58], where the energy loss can include the Landau distribution (this was switchable). The simulation did not include missing wires in the hits, stray particles nor particle contamination.

For the ERIKA input data, the desire is to have as a complete representation of the physics as possible without introducing random processes that would make the output (the wire numbers) a multiple valued function of the input (the momentum and position). For this reason, the random processes were disabled, these are the multiple scattering, and the Landau distribution of the energy loss (energy loss was assumed to happen at the most probable value). The finite wire chamber resolution, while not random, will reduce the accuracy of the ERIKA fit, so the finite resolution was not simulated. The accuracy of the fit was increased by expanding the dimensions of the wire chambers 10%[1]. The lead walls in the C magnet were disabled so that tracks passing through the lead walls are reconstructed correctly.[1]

For the single track data, the wire chambers are returned to their physical size, and the lead walls are re–enabled. The random processes are re–enabled.

For the two track data, the code is set up as for the single track data, and the momenta of the two pions in the events are correlated according to Equation 3.14. The two track data could optionally be analyzed as twice as many single track events, allowing comparison of the performance of the software when analyzing one and two track events.

The acceptance is calculated using the procedures for the single track events but, in addition, the pions were weighted by probability of emission, using data from [39, 40].

The acceptance is shown in Section 4.2. The one and two track efficiencies are discussed in Section 5.4. A fit to Monte Carlo correlated data is discussed in Sections 6.9 and 7.2.

[1]Such tracks are removed from the experimental data by requiring the distance from the track to the surface of the lead wall be positive.

Bibliography

[1] W. Zajc, Phd. thesis, The University of California, Berkeley (1982), LBL–14864, and W. Zajc, Phys. Rev. C **29**, 2173 (1984).

[2] R. Hanbury–Brown, R. Jennison and M. Das Gupta, Nature **170**, 1061 (1952).

[3] R. Hanbury–Brown and R. Twiss, Phil. Mag. (Series 7) **54**, 663 (1954).

[4] R. Hanbury–Brown and R. Twiss, Nature **177**, 27 (1956).

[5] R. Glauber, Phys. Rev. Lett. **10**, 84 (1963) and also R. Glauber, Phys. Rev. **130**, 2529 (1963), R. Glauber, Phys. Rev. **131**, 2766 (1963).

[6] J. Armstrong and A. Smith, Phys. Rev. **140** (Number 1A), A155 (1965).

[7] G. Goldhaber, S. Goldhaber, W. Lee and A. Pais, Phys. Rev. **120**, 300 (1960). See also G. Goldhaber *et al.*, Phys. Rev. Lett. **3**, 181 (1959).

[8] B. Lörstad, Int. J. Mod. Phys. A **4**, 2861 (1989).

[9] G. Kopylov and M. Podgoretskii, Sov. J. Nucl. Phys. **15**, 219 (1972).

[10] E. Shuryak, Phys. Lett. **44B**, 387 (1973).

[11] G. Cocconi, Phys. Lett. **49B**, 459 (1974).

[12] W. Zajc, *Bose–Einstein Correlations from Statistics to Dynamics*, in **Hadronic Multiparticle Production**, editor P. Carruthers, World Scientific Press, 1989.

[13] M. Deutschmann *et al.*, Nucl. Phys. B **103**, 198 (1976).

[14] M. Deutschmann *et al.*, Nucl. Phys. B **204**, 333 (1982).

[15] M. Adamus *et al.*, Z. Phys. C — Particles and Fields **37**, 347 (1988).

[16] G. Goldhaber in **Proceedings on the International Conference on High Energy Physics**, Lisbon, Portugal, 1981.

[17] G. Goldhaber in **Proceedings of the First International Conference on Local Equilibrium on Strong Interaction Physics**, editors P. Scott and R. Wiener, World Scientific Publishing Co., 1985.

[18] G. Goldhaber and I. Juričić, *New Results on the Bose-Einstein Effect in e^+e^- Interactions or the GGLP Effect Revisited*, in **Proceedings of the Second International Workshop on Local Equilibrium in Strong Interactions**, editors P. Carruthers and D. Strottman, World Scientific Publishing Co., Singapore, 1986.

[19] I. Juričić, Phd. thesis, The University of California, Berkeley (1987), LBL–24493 and I. Juričić *et al.*, Phys. Rev. D **39**, 1 (1989).

[20] B. Andersson and W. Hofmann, Phys. Lett. **169B**, 364 (1986).

[21] S. Nagamiya and M. Gyulassy, *High Energy Nuclear Collisions*, in **Advances in Nuclear Physics** (Vol. 3), editors J. Negele and E. Vogt, Plenum Press, 1984.

[22] S. Fung *et al.*, Phys. Rev. Lett. **41**, 1592 (1978).

[23] D. Beavis *et al.*, Phys. Rev. C **27**, 910 (1983).

[24] D. Beavis *et al.*, Phys. Rev. C **28**, 2561 (1983).

[25] D. Beavis *et al.*, Phys. Rev. C **34**, 757 (1986).

[26] J. Lu *et al.*, Phys. Rev. Lett. **46**, 898 (1981).

[27] T. Humanic, Phys. Rev. C **34**, 191 (1986).

[28] R. Bock *et al.*, Mod. Phys. Lett. A **3**, 1745 (1988).

[29] W. Christie, Phd. thesis, The University of California, Davis (to be published).

[30] A representative, but by no means complete, list of references is (in chronological order): J. Cugnon, T. Mizutani and J. Vandermeulen, Nucl. Phys. **A352**, 505 (1981);

E. Braun and Z. Fraenkel, Phys. Rev. C **34**, 120 (1986); Y. Kitazoe, M. Sano, H. Toki and S. Nagamiya, Phys. Lett. **166B**, 35 (1986); C. Gale, G. Bertsch and S. Das Gupta, Phys. Rev. C **35**, 1666 (1987); D. Boal and J. Glosli, Phys. Rev. C **37**, 91 (1988); J. Molitoris *et al.*, Phys. Rev. C **37**, 1014 (1988); and J. Aichelin *et al.*, Phys. Rev. C **37**, 2451 (1988).

[31] W. Zajc, Phys. Rev. D **35**, 3396 (1987).

[32] A. Chacon *et al.*, Phys. Rev. Lett. **60**, 780 (1988).

[33] M. Gyulassy, S. Kauffmann and L. Wilson, Phys. Rev. C **20**, 2267 (1979).

[34] F. Yano and S. Koonin, Phys. Lett. **78B**, 556 (1978).

[35] M. Deutschmann *et al.*, CERN/EP/PHYS/78-1 (1978).

[36] S. Pratt, Phys. Rev. Lett. **53**, 1219 (1984).

[37] M. Gyulassy, Phys. Rev. Lett. **48**, 454 (1982).

[38] S. Olsen *et al.*, LBL-2445 (1973).

[39] S. Nagamiya *et al.*, Phys. Rev. C **24**, 971 (1981).

[40] S. Hayashi *et al.*, Phys. Rev. C **38**, 1229 (1988).

[41] J. Harrison *et al.*, I. E. E. E. Transactions on Nuclear Science **NS-28**, 3724 (1981).

[42] A. P. Banford, **The Transport of Charged Particle Beams**, E. & F. N. Spon Ltd., London, 1966.

[43] E. Wind, *Principle Component Analysis and its Application to Track Finding*, in **Formulae and Methods in Experimental Data Evaluation** (Vol. 3), Editors R. Bock *et al.*, European Physical Society, CERN, Geneva, 1984.

[44] F. James and M. Roos, Nucl. Phys. **B172**, 475 (1980).

[45] M. Gyulassy and S. Kauffmann, Nucl. Phys. **A362**, 503 (1981).

[46] J. Sullivan private communications, and J. Sullivan *et al.*, Phys. Rev. C **25**, 1499 (1982).

[47] E. Merzbacher, **Quantum Mechanics**, John Wiley & Sons, New York, 1970, pp. 245–249.

[48] A. Frodesen, O. Skeggestad and H. Tøfte, **Probability and Statistics in Particle Physics**, Universitetsforlaget, 1979.

[49] F. James and M. Roos, Comp. Phys. Comm. **10**, 343 (1975).

[50] F. James, Comp. Phys. Comm. **20**, 29 (1980).

[51] T. Åkesson *et al.*, Phys. Lett. B **187**, 420 (1987).

[52] J. Molitoris *et al.*, Phys. Rev. C **33**, 867 (1986).

[53] J. Bartke, Phys. Lett. B **174**, 32 (1986).

[54] C. DeMarzo *et al.*, Phys. Rev. D **29**, 363 (1984).

[55] G. Agakishiev *et al.*, Sov. J. Nucl. Phys. **39** (3), 344 (1984).

[56] N. Akhababian, J. Bartke, V. Grishin and M. Kowlaski, Z. Phys. C — Particles and Fields **26**, 245 (1984).

[57] D. Beavis *et al.*, *Multi-Pion Production*, in **Proc. 7th High Energy Heavy Ion Study (Darmstadt, Oct. 1984)**, Report GSI–85–10 (Darmstadt, 1985) p. 771.

[58] M. Aguilar–Benitez *et al.*, **Particle Properties Data Booklet**, North Holland, Amsterdam, 1986.

LAWRENCE BERKELEY LABORATORY
TECHNICAL INFORMATION DEPARTMENT
1 CYCLOTRON ROAD
BERKELEY, CALIFORNIA 94720